High-Gain Parametric Amplification for the Generation of Quantum States of Light

by

Elna M. Nagasako

Submitted in Partial Fulfillment
of the
Requirements for the Degree
Doctor of Philosophy

Supervised by
Professor Robert W. Boyd

The Institute of Optics
The College
School of Engineering and Applied Sciences

University of Rochester
Rochester, New York

2001

Curriculum Vitae

The author was born in Hilo, Hawaii in 1969. From 1987 to 1991, she attended Pomona College in Claremont, California. She graduated Cum Laude with a Bachelor of Arts degree in Physics and Mathematics. She began graduate studies at the University of Rochester Institute of Optics in 1991. In 1997 she began employment as a senior technical associate in the Department of Anesthesiology, where she has been working on quantitative methods of assessing peripheral nervous system function. Her doctoral research at the Institute of Optics has been conducted under the supervision of Professor Robert W. Boyd and has been focused on the quantum properties of nonlinear optical processes.

Publications

E.M. Nagasako, S.J. Bentley, R.W. Boyd, and G.S. Agarwal, "Nonclassical two-photon interferometry and lithography with high-gain optical parametric amplifiers", to be published in Physical Review A, Sept. 2001.

E.M. Nagasako, S.J. Bentley, R.W. Boyd, and G.S. Agarwal, "Parametric downconversion vs. optical parametric amplification: a comparison of their quantum statistics", to be published in Journal of Modern Optics.

R. H. Dworkin, E. M. Nagasako, R. W. Johnson, and D. R. J. Griffin, "Acute pain in herpes zoster: the famciclovir database project", to be published in Pain.

R. H. Dworkin, E. M. Nagasako, and B. S. Galer, "Assessment of Neuropathic Pain", in *Handbook of Pain Assessment (2nd ed.)*, edited by D. C. Turk and R. Melzack, in press.

R. H. Dworkin, E. M. Nagasako, R. D. Hetzel, and J. T. Farrar, "Assessment of Pain and Pain-Related Quality of Life in Clinical Trials", in *Handbook of Pain Assessment (2nd ed.)*, edited by D. C. Turk and R. Melzack, in press.

G. S. Agarwal, R. W. Boyd, E.M. Nagasako, and S.J. Bentley, Physical Review Letters **86**, 1389 (2001) [comment].

R. H. Dworkin, F. M. Perkins, and E. M. Nagasako, " Prospects for the prevention of postherpetic neuralgia in herpes zoster patients", Clinical Journal of Pain **16**, S90 (2000) .

E. M. Nagasako, R. W. Boyd, and G. S. Agarwal, "Vacuum-induced jitter in spatial solitons", Optics Express **3**(5) (1998).

E. M. Nagasako, R. W. Boyd, and G. S. Agarwal, "Vacuum-field-induced filamentation in laser-beam propagation", Physical Review A **55**, 1412 (1997).

E. M. Nagasako and R. W. Boyd, "From Laser Beam Filamentation to Optical Solitons: The Influence of C. H. Townes on the Development of Modern Nonlinear Optics", in Amazing Light, edited by R. Y. Chiao (Springer-Verlag, New York, 1996).

W. V. Davis, M. Kauranen, E. M. Nagasako, R. J. Gehr, A. L. Gaeta, R. W. Boyd, and G. S. Agarwal, "Excess noise acquired by a laser beam after propagating through an atomic potassium vapor", Physical Review A **51**, 4152 (1995).

R. W. Boyd, G. S. Agarwal, W. V. Davis, A. L. Gaeta, E. M. Nagasako, and M. Kauranen, "Quantum Noise Characteristics of Nonlinear Optical Amplifiers", Acta Physica Polonica A **86**, 117 (1994).

D. W. Hoard, E. Nagasako, and W. Sandmann, "Time of eclipse for the binary system PV Cas." Information Bulletin on Variable Stars, no. 3462, p. 1-5 (1990).

D. W. Hoard, E. Nagasako, and W. Sandmann, "UBVR photometry of the ZZ Ceti star G 185-32." Information Bulletin on Variable Stars, no. 3461, p. 1-4 (1990).

Presentations

R.W. Boyd, E.M. Nagasako, S.J. Bentley, and G.S. Agarwal, "Nonclassical two-photon interferometry and lithography with high-gain optical parametric amplifiers", 8th Rochester Conference on Coherence and Quantum Optics, June 13-16, 2001, Rochester, New York, ThC1.

R.H. Dworkin, E.M. Nagasako, R.W. Johnson, and D.R.J. Griffin, "Risk factors for severe acute herpes zoster pain and postherpetic neuralgia", Association of University Anesthesiologists 48th Annual Meeting, May 17-20, 2001, Rochester, New York.

S.J. Bentley, R.W. Boyd, E.M. Nagasako, and G.S. Agarwal, "Quantum entanglement for optical lithography and microscopy beyond the Rayleigh limit", Quantum Electronics and Laser Science Conference (QELS), May 6-11, 2001, QTuD2.

E.M. Nagasako, R.W. Johnson, D.R.J. Griffin, and R.H. Dworkin, "Risk factors for postherpetic neuralgia in early herpes zoster: the famciclovir database project", 20th Annual Scientific Meeting of the American Pain Society, April 19-22, 2001, Phoenix, Arizona.

E.M. Nagasako, R.W. Johnson, D.R.J. Griffin, and R.H. Dworkin, "Geographic and racial aspects of herpes zoster: the famciclovir database project", 4th International Conference on Varicella, Herpes Zoster, and Postherpetic Neuralgia, March 3-5, 2001, La Jolla, California.

R. H. Dworkin, D. I. Kulick, C. H. Andrus, L. A. Hogan, E. M. Nagasako, and F. M. Perkins, "Chronic pain following breast cancer surgery", Era of Hope, Department of Defense Breast Cancer Research Program Meeting, June 8-11, 2000, Atlanta, Georgia. Proceedings Vol. II p. 801.

P. A. Tick, E. M. Nagasako, and R. W. Boyd, "Dye-doped glasses: nonlinear optical materials for spatial soliton applications", Nonlinear Optics '98. Materials, Fundamentals, and Applications Topical Meeting (Cat. No. 98CH36244). IEEE. 1998, pp. 379-80. New York, NY.

E. M. Nagasako, R. W. Boyd, and G. S. Agarwal, "Laser beam filamentation initiated by quantum fluctuations", Optical Society of America Annual Meeting, Rochester, NY, October 1996.

E. M. Nagasako, R. W. Boyd, and G. S. Agarwal, "Quantum fluctuations as the origin of laser beam filamentation", QELS '95. Summaries of Papers Presented at the Quantum Electronics and Laser Science Conference. Vol. 16. 1995 Technical Digest Series Conference Edition. Opt. Soc. America 1995, p. 178. Washington DC.

R. W. Boyd, G. S. Agarwal, W. V. Davis, A. L. Gaeta, M. Kauranen, and E. Nagasako, "Signal to noise characteristics of nonlinear optical amplifiers" LEOS '93 Conference proceedings IEEE Lasers and Electro-optics Society 1993 Annual Meeting (Cat. No. 93CH3297-9) IEEE. 1993, pp. 309-10 New York, NY.

Acknowledgments

I would first like to thank Professor Robert W. Boyd for his guidance and support. He has been very tolerant of an unconventional career journey. In addition to making the projects within these pages possible, he has also taught me the importance of placing research findings within a larger scientific and societal context. I have matured as a scientist in large part through my interactions with him.

I would be remiss if I did not thank Dr. Girish S. Agarwal for his interest in and assistance with these projects. His wide-ranging theoretical expertise was invaluable and his visits were always a spur to my productivity.

This work would also have not been possible without the other members of Dr. Boyd's research group. Sean Bentley has been a valued collaborator on many of these projects. Discussions with fellow group members, scientific and otherwise, have been an enjoyable part of my graduate school experience, especially with Eric Buckland, George Fischer, and Russell Gehr from the early days and Ryan Bennink and Vincent Wong in these recent years.

The staff and administrators of the Institute of Optics have had to deal with

reams of additional paperwork due to the divergence of my career path from the norm. I would like to thank them for their assistance and their friendship.

Finally I would like to thank my family, especially my husband Leon, whose patience knows no bounds.

Abstract

The novel quantum statistical properties of the two-photon entangled states generated by spontaneous parametric downconversion have been utilized in a variety of fourth-order interferometric configurations. The extent to which the intense light produced by an unseeded parametric amplifier (optical parametric generator) retains these desirable properties is explored in a series of calculations.

Common fourth-order interferometric configurations using two-photon entangled states are summarized, with an emphasis on the Hong-Ou-Mandel and Mach-Zehnder interferometers. This summary is followed by a review of recent proposals for the exploitation of entangled states for sub-Rayleigh-limit imaging.

The limitations of using parametric downconversion at two-photon levels are discussed and the replacement of two-photon interferometric sources with the multiphoton output of a high-gain optical parametric generator is considered. The output of the Hong-Ou-Mandel interferometer, Mach-Zehnder interferometer, and quantum lithography configurations as a function of single-pass gain is determined, and the interpretation of these results in the context of multiple photon pair contributions to interferometric patterns is presented.

The analysis of the high-gain optical parametric generator as a fourth-order interferometric source is then extended to the case of multiple signal and idler output modes. The impact of the system transfer characteristics on the desired interferometric properties is discussed.

The initiation of beam filamentation by vacuum fluctuations is considered, and this four-wave mixing process is compared to parametric downconversion as a source for fourth-order interferometric applications.

We conclude by contrasting the states produced by high-gain optical parametric generation with coherent states and the states produced by seeded optical parametric amplification as sources for fourth-order interferometric configurations.

Table of Contents

List of Tables

List of Figures

Chapter 1

Introduction

States of light produced by parametric downconversion have been utilized in a variety of experimental settings. The two-photon entangled states produced by spontaneous parametric downconversion have excited interest due to their potential for use in fields such as Einstein-Podolsky-Rosen experiments [1–3], Heisenberg-limited phase measurements [4,5], sub-Rayleigh limit lithography [6–8], and quantum cryptography [9,10].

Parametric downconversion [11–14] is the nonlinear process by which a pump field at frequency ω_0 is used to produce two output fields–conventionally called the signal and idler–at frequencies ω_s and $\omega_i = \omega_0 - \omega_s$. This process may be initiated spontaneously, with only a pump beam as an input, or seeded by the provision of an additional beam at the desired wavelength. In the latter case, this externally provided signal beam will be amplified, accompanied by the production of an idler beam at an appropriate wavelength.

A variety of devices have been developed to exploit these effects. An op-

tical parametric generator (OPG) uses spontaneous parametric downconversion (SPDC) to produce a seed beam for later amplification stages. Optical parametric oscillators (OPOs) enclose the downconversion crystal in a cavity; optical parametric amplifiers (OPAs) are high-gain devices used for signal field amplification.

The fields produced by parametric downconversion and parametric amplification possess interesting quantum features [15–19]. In the high-gain limit, where multiple photons are produced, the OPO and OPA have been analyzed as sources of strongly correlated beams [20–25]. The relationship between the signal and idler beams has been exploited in the OPA configuration to produce two amplified copies of an image-bearing beam that are spatially entangled [20]. In addition, the spatial patterns arising from quantum noise have been investigated in the context of the OPO [21,26,24,27]. When operated as a phase-sensitive amplifier, the OPA has been used for noiseless image amplification [22].

At the low-gain limit, in which single photon pairs are produced, spontaneous parametric downconversion has been extensively studied as a source of two-photon entangled states [28–30]. These states may be entangled with respect to a variety of different physical attributes such as time of arrival [31] and state of polarization [32] and have been analyzed in a variety of experimental situations [33–36]. Photon pairs are especially useful in the context of fourth-order interferometric

studies [37–39,15,16,40–43], where they can be used to demonstrate a variety of nonclassical features.

While strong quantum correlations are present in both the low- and high-gain limits of the parametric amplification process, the nature of these correlations may be quite different, and the extent to which the features characteristic of two-photon entangled state sources persist as the gain of the generating process is increased is unclear. In this thesis, we explore the transition between the two-photon entangled states produced at the low-gain limit and the correlated states produced at the high-gain limit of the parametric amplification process. In particular, the effect of increased source gain on the output of fourth-order interferometric configurations is analyzed.

The analyses that form the core of this thesis use the properties of two-photon entangled state sources in interferometric systems as their starting point. We thus begin by using the remainder of this chapter to present a brief overview of the parametric downconversion process and introduce the two-photon entangled states produced at the low-gain limit of this process.
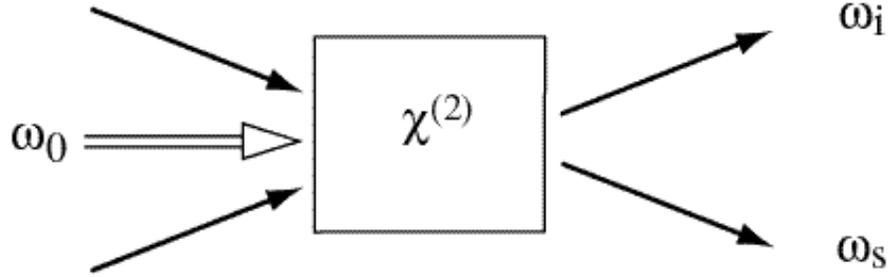
Figure 1.1: Parametric downconversion layout. The generated signal (ω_s) and idler (ω_i) beams are strongly correlated.

1.1 Parametric downconversion

Parametric amplification is a nonlinear optical process that couples three optical fields via a material polarization of the form

$$P_{NL}(\omega_0 - \omega_s) \propto \chi^{(2)}(\omega_0 - \omega_s, \omega_0, \omega_s)E(\omega_0)E^{(*)}(\omega_s) \tag{1.1}$$

where $P(\omega)$ and $E(\omega)$ represent the components of the polarization and the applied field at frequency ω. (Figure 1.1) This process is also known as difference-frequency generation, as applied fields at ω_s and ω_0 lead to the creation of a third field at $\omega_i = \omega_0 - \omega_s$. This interaction can be understood in terms of the absorption of photons at ω_0 accompanied by the generation of photon pairs at ω_s and ω_i (Figure 1.2). In addition to the generation of a field at frequency ω_i this interaction also leads to the amplification of the field applied at ω_s and the depletion of the field at ω_0. The generated beams are conventionally called the signal (ω_s) and idler (ω_i) beams, with the beam at ω_0 designated as the pump beam. While
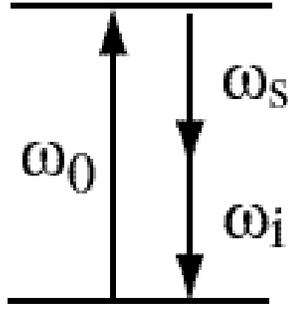
Figure 1.2: Parametric downconversion energy level diagram. Parametric downconversion creates photons at frequencies ω_s and ω_i while annihilating pump photons at frequency ω_0.

the above discussion presupposed the application of both a pump and signal field, the production of signal and idler photons may also occur spontaneously, with only a pump field incident on the material. This process of spontaneous parametric downconversion is a frequently analyzed source of strongly correlated photon pairs.

In understanding the correlations present in the output of the seeded and unseeded parametric amplifier, it is useful to note that in addition to the energy conservation relationship $\omega_s + \omega_i = \omega_0$, the interacting fields are also constrained by the value of the wavevector mismatch $\Delta\mathbf{k} = \mathbf{k}_0 - \mathbf{k}_s - \mathbf{k}_i$ (Figure 1.3). The efficiency of the downconversion process is strongly dependent on $\Delta\mathbf{k}$, with fields satisfying $\Delta\mathbf{k} = 0$ (perfect phase matching) generated the most efficiently. The properties of the signal and idler photons are not independent, but are thus associated by relationships of this type.
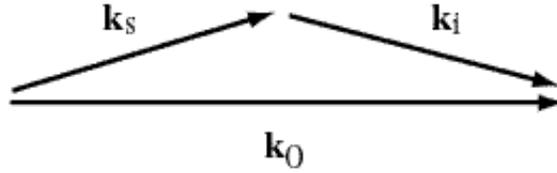
Figure 1.3: Parametric downconversion phase-matching diagram. Photons participating in the downconversion process must satisfy phase-matching relations.

1.2 Two-photon entangled states

An unseeded parametric amplifier produces an output of the form $\sum_m \rho^{(m)}|m\rangle_s|m\rangle_i$ in which the same number of photons is contained in the signal and idler modes. The distribution over m is affected by the source gain. As the gain is reduced, the contribution of the higher photon number terms is reduced; when the gain is very low, the output can be approximated by a state of the form $|1\rangle_s|1\rangle_i$, which consists of a single photon pair. As discussed in the previous section, the nature of the downconversion process leads to strong relationships between the characteristics of the photons in this pair. This property of the downconversion process has been exploited to generate two-photon entangled states for use in various experimental applications [44,45,2,46,47,30,48].

The degree of correlation between the signal and idler photons can be affected by both the material and pump field properties (Figure 1.4). In the limit of an infinite interaction region, perfect phase matching is required, providing a tight constraint on the signal-idler relationship. As this assumption is relaxed
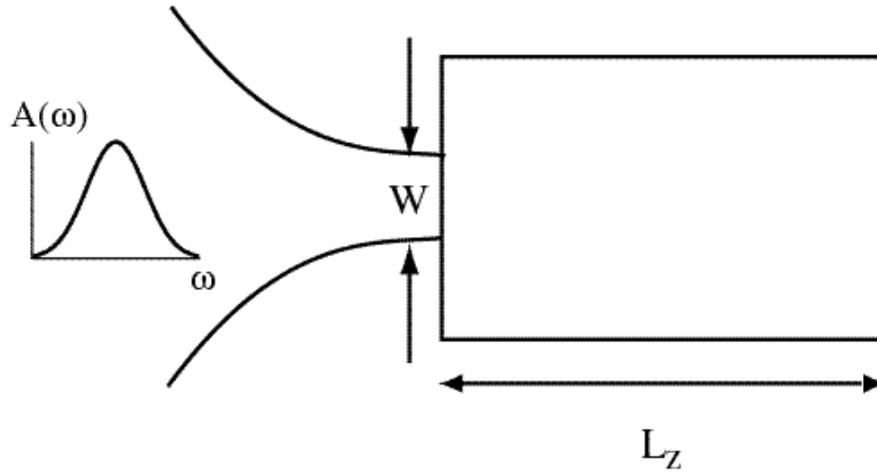
Figure 1.4: Factors affecting the degree of entanglement.

(e.g. finite nonlinear crystal length), some degree of mismatch can be tolerated, allowing a range of Δk_z values.

Similarly, in the limit of a monochromatic plane wave pump, there are single values assumed by ω_0 and $\mathbf{k}_0$ in the energy conservation and phase matching relationships; if these assumptions are violated, the relationship between various signal and idler parameters will not be as well specified. For instance, if the pump field has finite width, the additional transverse wavevector components present ($\mathbf{k}_{0\perp}$) allow the transverse component of the signal-idler wavevector sum $\mathbf{k}_{s\perp} + \mathbf{k}_{i\perp}$ to take on a range of values. Likewise, if a broadband pump is used, the range of frequencies present implies that the sum $\omega_s + \omega_i$ does not have a fixed value.

If only a single signal mode and a single idler mode are being considered, the two-photon state produced by a spontaneous parametric downconversion event (e.g. in an unseeded low-gain parametric amplifier) may be written in the form

$|1\rangle_s|1\rangle_i$. If more than one signal and idler mode are being analyzed, a more detailed notation is necessary.

In general, a multimode two-photon state may be written

$$|\psi\rangle = \int \int d\omega_s d\omega_i \psi(\omega_s, \omega_i)|\omega_s\rangle_s|\omega_i\rangle_i \qquad (1.2)$$

where $|\omega_s\rangle_s$ designates a single photon Fock state in the signal mode with frequency ω_s and $|\omega_i\rangle_i$ a single photon Fock state in the ω_i idler mode. The probability amplitude distribution in the case of perfect entanglement is given by $\psi(\omega_s, \omega_i) = \psi(\omega_s)\delta(\omega_i - f(\omega_s))$ and the output state can thus be written

$$|\psi\rangle = \int d\omega_s \psi_s(\omega_s)|\omega_s\rangle_s|f(\omega_i)\rangle_i. \qquad (1.3)$$

An example of this type of state is given by the output of a Type-I downconverter driven by a cw plane-wave pump

$$|\psi\rangle = \int d\omega_s \psi_s(\omega_s)|\omega_s\rangle_s|\omega_p - \omega_s\rangle_i, \qquad (1.4)$$

where the distribution $\psi_s(\omega_s)$ incorporates the interaction strength, mode spacing, and the phase matching function [49].

As discussed at the beginning of this section, under some conditions there may no longer be a one-to-one relationship between the signal and idler parameters.

A given signal mode may be associated with a range of idler modes; the signal and idler are now partially, rather than fully, entangled. This may be described in general by allowing the probability distribution $\psi(\omega_s, \omega_i)$ to be dependent on both the signal and idler parameters separately. In the limit of no entanglement, the distribution factors into the product of signal and idler distributions $\psi_s(\omega_s) \times \psi_i(\omega_i)$.

1.3 Overview of thesis

The two-photon entangled states introduced in this chapter have been extensively analyzed as sources for fourth-order interferometric systems. Three of these systems will be used in this thesis to explore the changes that occur in the output of an unseeded parametric amplifier as the mean number of photons in the output is increased from the regime in which single pairs of photons are produced to the regime where the mean photon number is high. The two-photon results that provide the starting point for this work are reviewed in Chapter 2. In this chapter, major findings in which two-photon entangled states are used in fourth-order interferometric setups are discussed. In particular, the interferometric configurations that will be the focus of later chapters are presented. The three interferometric arrangements of interest–the Hong-Ou-Mandel interferometer, the Mach-Zehnder interferometer, and quantum lithography–are discussed, with an emphasis on the results produced when entangled photon pairs are used as inputs.

The analyses of the effects of increased gain on these interferometric results begin in Chapter 3 with a single mode treatment. A model for the output of a parametric amplifier that allows the gain to be varied from the low levels used to produce entangled photon pairs to the higher levels at which multiple pairs are generated is used to determine the output of the Hong-Ou-Mandel interferometer, Mach-Zehnder interferometer, and quantum lithography arrangements. A generalized expression applicable to any four-port fourth-order interferometer is used to clarify the separate roles that source statistics and interferometer configurations play in determining the output when multiple-photon-pair sources are used.

The focus of Chapter 4 is the extension of the analysis of Chapter 3 to the case where the interferometer inputs consist of multiple modes. Multimode descriptions of the two-photon entangled state and the associated results for the Hong-Ou-Mandel interferometer are reviewed. These models are then used to analyze the effect of source asymmetry on the quantum lithography configuration. A multimode treatment of the state produced by the parametric amplifier is then presented, and the result applied to the Hong-Ou-Mandel interferometer and quantum lithography. The low- and high-gain parametric amplifier results are then compared to the two-photon entangled state results to investigate the effect of multiple photon pairs on fourth-order interferometric devices. The impact of the transfer characteristics of an interferometer using these sources on the output pattern is also explored using these models.

Chapter 5 focuses on vacuum-induced beam filamentation, which is another unseeded nonlinear interaction producing photon pairs. We begin by discussing the initiation of this process by vacuum fluctuations. This process is then compared to spontaneous parametric downconversion in the context of fourth-order interferometric systems.

Analyses of the high-gain limit of a parametric amplification source invite the question of whether the outputs produced by a high-gain parametric downconversion source can be duplicated by a coherent state source. Although two-photon entangled state sources have been shown to be superior to coherent state sources for the generation of many of these properties of interest, the extent to which the results produced by high-gain parametric downconversion retain this superiority is less clear. A related question is the extent to which the presence of a seed affects the character of the pattern produced by parametric downconversion at low and high gain levels. Chapter 6 returns to the single mode model of Chapter 3 to investigate coherent and seeded parametric amplifier source states as multiphoton pair fourth-order interferometric sources. Systems considered in this chapter are the Hong-Ou-Mandel interferometer and quantum lithography configurations.

Chapter 2

Fourth-Order Interferometry with Single-Pair Entangled States

2.1   Introduction

Many of the experiments in which two-photon entangled states have been utilized involve fourth-order interference [37–39,15,16,40,50,34,41,42]. As with conventional (second-order) interferometry, the recombination of field amplitudes creates an output pattern that is dependent on the path differences between interferometer arms, but in fourth-order interferometry pairs of photons, rather than single photons, are detected. This measurement may be accomplished via the registration of coincident photon detections or with the use of a two-photon absorbing substrate.

The Hong-Ou-Mandel interferometer is an extensively analyzed fourth-order interferometric configuration [51,38]. Consisting of a coincidence count detector placed at the two outputs of a beamsplitter, it has been used to investigate the

correlation time between the signal and idler photons issuing from a simultaneous downconversion event [51] as well as the role of spectral distinguishability in fourth-order interference [52–54].

The Mach-Zehnder interferometer is another fourth-order interferometric configuration. It is an arrangement that is well-known from second-order interferometry applications. It has also been utilized in fourth-order applications for the investigation of the nonclassical properties of two-photon entangled states. For fourth-order interferometry a coincidence count detector is placed across the interferometer output ports. Using this configuration, two-photon entangled states were shown to have an output that exhibits a dependence on the path difference between the two arms of the interferometer under conditions where this dependence is not present for coherent state input. [55]

The difference in interferometer output between two-photon entangled state and coherent state sources has also been investigated in the area of sub-Rayleigh-limit pattern formation. Entangled states of the form $|m\rangle|m\rangle$ have been proposed as sources for the generation of lithographic patterns with features smaller by a factor of $2m$ than that conventionally expected from the wavelength utilized. [6] In this configuration (for m = 1), a two-photon absorbing substrate rather than coincidence count detection is used to observe the interferometric effect.

We begin with a brief introduction to fourth-order interferometric quantities and the models used in the analysis of the Hong-Ou-Mandel interferometer, Mach-

Zehnder interferometer, and quantum lithography configurations. The results obtained with these models in the case of two-photon entangled state input are then reviewed.

2.2 Fourth-order interference

Fourth-order interferometry is a technique commonly used in tandem with two-photon entangled state sources [39,28]. Among the fourth-order interferometers used in this context are the Hong-Ou-Mandel interferometer [6] and the Mach-Zehnder interferometer [55]. In this section we review the quantities used in the analysis of these configurations, beginning with more familiar second-order interferometric expressions and connecting the fourth-order cross-correlation function to the coincidence count rates used to measure the output of these fourth-order interferometers.

The second-order cross-correlation function for a fluctuating complex analytic field operator E is given by

$$\Gamma^{(1,1)}(\mathbf{r}_1, \mathbf{r}_2; t_1, t_2) = \langle E^*(\mathbf{r}_1, t_1) E(\mathbf{r}_2, t_2) \rangle \tag{2.1}$$

The second-order cross-correlation function is intimately related to the characteristics of the interference pattern created by two pinholes placed in a stationary, ergodic, quasimonochromatic field, as can be seen in the expression for the inten-

sity at a point $\mathbf{r}$ in the viewing plane

$$\langle I(\mathbf{r},t)\rangle = |C_1|^2\langle I(\mathbf{r}_1,t)\rangle + |C_2|^2\langle I(\mathbf{r}_2,t)\rangle + 2Re[C_1^*C_2\Gamma^{(1,1)}(\mathbf{r}_1,\mathbf{r}_2;t_1,t_2)] \quad (2.2)$$

where $\mathbf{r}_1$ and $\mathbf{r}_2$ are the pinhole locations, t_1 and t_2 are the travel times for light to reach $\mathbf{r}$ from pinholes 1 and 2, and C_1 and C_2 are constants related to the pinhole properties. The fringe visibility is equal to the magnitude of the normalized cross-correlation function and the phase of the normalized cross-correlation function determines the offset of the fringes in the observation plane [56].

The second-order cross-correlation function can be generalized in quantum mechanical calculations to

$$\Gamma^{(1,1)}(\mathbf{r}_1,\mathbf{r}_2;t_1,t_2) = \langle \hat{E}^{(-)}(\mathbf{r}_1,t_1)\hat{E}^{(+)}(\mathbf{r}_2,t_2)\rangle \qquad (2.3)$$

where $\hat{E}^{(+)}$ corresponds to the field annihilation operator and $\hat{E}^{(-)}$ corresponds to the field creation operator. The cross-correlation function can be generalized to different orders in $\hat{E}^{(-)}$ and $\hat{E}^{(+)}$. In particular, the fourth-order cross correlation function is defined as

$$\Gamma^{(2,2)}(\mathbf{r}_1,\mathbf{r}_2,\mathbf{r}_3,\mathbf{r}_4;t_1,t_2,t_3,t_4) = \langle \hat{E}^{(-)}(\mathbf{r}_1,t_1)\hat{E}^{(-)}(\mathbf{r}_2,t_2)\hat{E}^{(+)}(\mathbf{r}_3,t_3)\hat{E}^{(+)}(\mathbf{r}_4,t_4)\rangle.$$

$$(2.4)$$

These correlation functions can be shown to be related to the probability of

photodetection with the field $\hat{E}$, with a photodetection probability involving N detectors proportional to the correlation function of 2Nth order [56]. Thus the instantaneous photodetection probability with a single photodetector is given by

$$P(\mathbf{r}, t) \propto \Gamma^{(1,1)}(\mathbf{r}, \mathbf{r}; t, t) \tag{2.5}$$

and the instantaneous photodetection probability for 2 detectors is given by

$$P(\mathbf{r}_1, t_1; \mathbf{r}_2, t_2) \propto \Gamma^{(2,2)}(\mathbf{r}_1, \mathbf{r}_2, \mathbf{r}_2, \mathbf{r}_1; t_1, t_2, t_2, t_1). \tag{2.6}$$

When interference is present, combining field variables at different displacements and times, the arguments in the correlation functions need not be symmetric.

2.3 Hong-Ou-Mandel interferometer

One well-analyzed example of a fourth-order interferometer is the Hong-Ou-Mandel interferometer [51,37,57]. This device consists of a 50/50 beamsplitter with a variable delay between the two input arms (Figure 2.1). Given an input consisting of a single photon in each arm, there are two paths that can lead to a coincidence count-both photons can be reflected or both transmitted. The destructive interference between these two possibilities leads to a decrease in the coincidence count rate from that naively expected. This decrease has been used
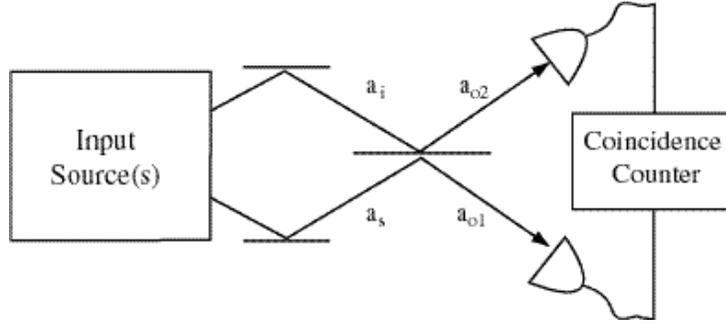
Figure 2.1: Hong-Ou-Mandel interferometer layout. This interferometer is used for fourth-order measurements.

to measure the temporal separation of two photons created by the same parametric downconversion event [51]. In order to consider the impact of a path difference between the two arms of the interferometer, it is necessary to utilize a multimode treatment of the input and output arms. However, the most striking feature-coincidence count cancellation-can be seen in a simple single mode treatment with no path difference between the two arms of the interferometer.

A beamsplitter can be described by equations with the general form

$$\hat{a}_{o_1} = \exp(i\phi_2) \left[\hat{a}_s \sqrt{R} \exp(i\alpha) + \hat{a}_i \sqrt{T}\right] \tag{2.7}$$

$$\hat{a}_{o_2} = \exp(i\phi_3) \left[\hat{a}_s \sqrt{T} + \hat{a}_i \sqrt{R} \exp(i(\pi - \alpha))\right], \tag{2.8}$$

where R and T are the reflectivity and transmissivity, respectively. For specificity, we will set the beamsplitter phase values to be $\phi_2 = \phi_3 = -\frac{\pi}{2}$ and $\alpha = \frac{\pi}{2}$, giving

the relationships [58]

$$\hat{a}_{o_1} = \sqrt{R}\hat{a}_s - i\sqrt{T}\hat{a}_i \tag{2.9}$$

$$\hat{a}_{o_2} = -i\sqrt{T}\hat{a}_s + \sqrt{R}\hat{a}_i. \tag{2.10}$$

The count rate in one of the output arms is given by

$$\langle \hat{a}_{o_1}^\dagger \hat{a}_{o_1} \rangle = R\langle \hat{a}_s^\dagger \hat{a}_s \rangle + T\langle \hat{a}_i^\dagger \hat{a}_i \rangle + i\sqrt{RT}[\langle \hat{a}_i^\dagger \hat{a}_s \rangle - \langle \hat{a}_s^\dagger \hat{a}_i \rangle] \tag{2.11}$$

and the coincidence count rate between the two detectors is given by

$$
\begin{aligned}
\langle \hat{a}_{o_1}^\dagger \hat{a}_{o_2}^\dagger \hat{a}_{o_2} \hat{a}_{o_1} \rangle = & \quad RT\langle \hat{a}_s^\dagger \hat{a}_s^\dagger \hat{a}_s \hat{a}_s \rangle + R^2 \langle \hat{a}_s^\dagger \hat{a}_i^\dagger \hat{a}_i \hat{a}_s \rangle \\
& + T^2 \langle \hat{a}_i^\dagger \hat{a}_s^\dagger \hat{a}_s \hat{a}_i \rangle + RT \langle \hat{a}_i^\dagger \hat{a}_i^\dagger \hat{a}_i \hat{a}_i \rangle \\
& + 2\ RT \langle \hat{a}_s^\dagger \hat{a}_s^\dagger \hat{a}_i \hat{a}_i \rangle - 2\ RT \langle \hat{a}_s^\dagger \hat{a}_i^\dagger \hat{a}_s \hat{a}_i \rangle
\end{aligned}
\tag{2.12}
$$

The single detector count rate can thus be found to be

$$
\langle \hat{a}_{o_1}^\dagger \hat{a}_{o_1} \rangle =
\begin{cases}
1 & \text{for } |11\rangle \\
|\alpha_0|^2 & \text{for } |\alpha_0\alpha_0\rangle
\end{cases}
\tag{2.13}
$$

where the relationship $R + T = 1$ has been used. We can see that in both cases the result is nonzero and is independent of the specific values of the reflectivity and transmissivity.

The coincidence count rate between the two detectors has the value for these states of

$$\langle \hat{a}_{o_1}^\dagger \hat{a}_{o_2}^\dagger \hat{a}_{o_2} \hat{a}_{o_1} \rangle = \begin{cases} (R-T)^2 & \text{for } |11\rangle \\ \\ |\alpha_0|^4 & \text{for } |\alpha_0\alpha_0\rangle \end{cases} \tag{2.14}$$

We can see that in this case the specific value of the coincidence count rate can depend on the value of the reflectivity and transmissivity. Furthermore, for the 50/50 beamsplitter of the HOMI, the coincidence count rate vanishes for two-photon entangled state input. This absence of coincidence counts when the single detector rates are nonzero is the signature of quantum interference in the HOMI. This stands in contrast to the results for coherent state input, for which the coincidence count rate simply equals the product of the single detector rates.

When the spectral distribution that is present in the interferometer source is to be considered, a multimode analysis using a field description such as that in Equation 1.2 is necessary. Using such a model, and assuming a Gaussian spectral distribution, the coincidence count rate is found to have the form [51]

$$Rate \propto R^2 + T^2 - 2RTe^{-\left(\frac{\tau}{\tau_c}\right)^2} \tag{2.15}$$

where τ is the time delay between the two arms and τ_c is the coherence time between the downconverted photons. This coherence time is determined by the width of the spectral distribution present in these two arms. The coincidence count rate plotted as a function of time delay thus has a minimum when the arms
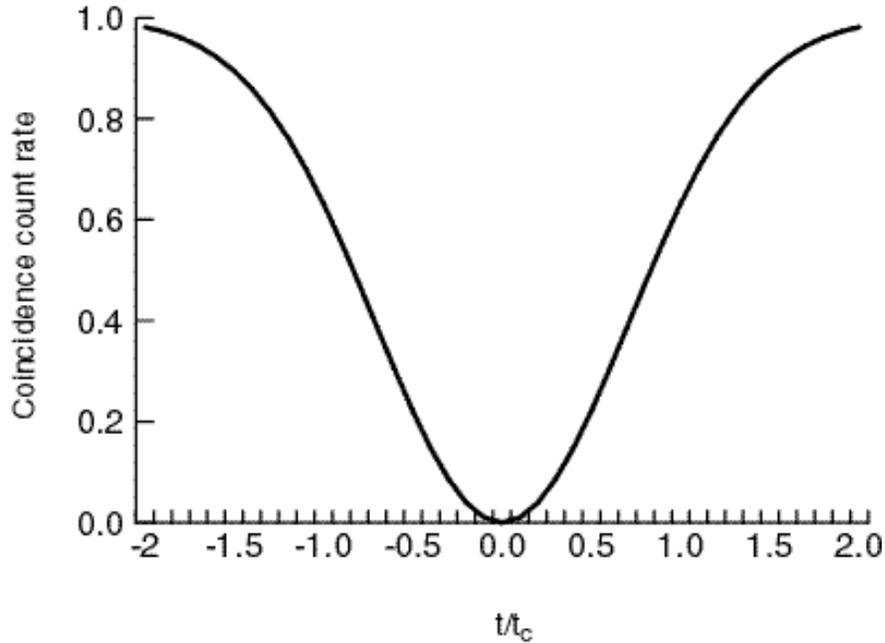
Figure 2.2: Hong-Ou-Mandel interferometer coincidence count rate. The count rate is plotted as a function of time delay between the two interferometer arms. As the time delay increases, the interference-created reduction in coincidence rate disappears. The time delay is normalized to the photon coherence time, which is the inverse of the spectral width.

are perfectly matched. For a 50/50 beamsplitter, the coincidence count rate at this minimum vanishes. As the time delay increases the coincidence count rate increases to its asymptotic value (Figure 2.2). The range of time over which this feature occurs provides a measure of the coherence time between the input arms of the interferometer. For a parametric downconversion source, this coherence time is a measure of the temporal separation between the photons from a single downconversion event. [51]

For type-I downconversion, the output spectral distribution is symmetric with respect to the signal and idler frequencies. The signal and idler photons are thus

indistinguishable. This condition produces the interference effect with the greatest visibility. For type-II downconversion with a broadband pump, however, the output spectra of the signal and idler photons can differ. This difference increases the distinguishability of the photons, and this spectral distinguishability leads to a loss of contrast in the interference pattern produced [52–54]. Visibility can be restored through the use of spectral filtering [59,53] or source symmetrization [49].

2.4 Mach-Zehnder interferometer

The Mach-Zehnder interferometer is another fourth-order configuration that has been explored using two-photon entangled state input [55,39,5,4,60,61]. As with the second-order Mach-Zehnder, the input beams are combined with a beamsplitter, directed along two arms that may differ in pathlength, and recombined using a second beamsplitter. In the fourth-order interferometer, the output is detected with a coincidence count detector placed across the two output ports of the second beamsplitter (Figure 2.3).

The input and output modes of the Mach-Zehnder are related by

$$\hat{a}_{o_1} = \frac{1}{2}(1 - e^{i\chi}) \ \hat{a}_s + \frac{-i}{2}(1 + e^{i\chi}) \ \hat{a}_i \tag{2.16}$$

$$\hat{a}_{o_2} = \frac{-i}{2}(1 + e^{i\chi}) \ \hat{a}_s + \frac{1}{2}(-1 + e^{i\chi}) \ \hat{a}_i \tag{2.17}$$

where χ is the phase difference arising from the difference in pathlength between
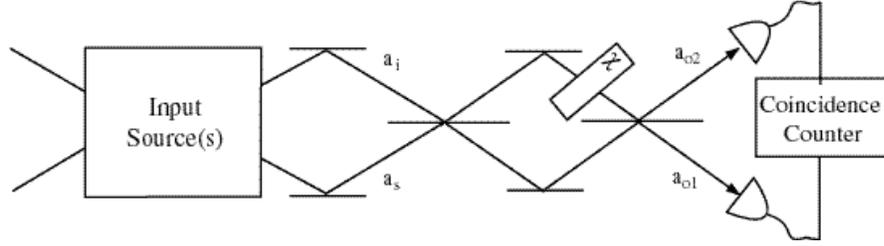
Figure 2.3: Mach-Zehnder interferometer layout. The coincidence counter displayed would be used for fourth-order interferometric measurements. For second-order measurements, the output of a single photodetector would be used.

the two arms. Using these relationships, the probability of a photodetection at one of the output ports is proportional to $\Gamma^{(1,1)}(\mathbf{r}, \mathbf{r}; t, t) \propto \langle \hat{a}_{o_1}^\dagger \hat{a}_{o_1} \rangle$ which has the value

$$\langle \hat{a}_{o_1}^\dagger \hat{a}_{o_1} \rangle = \frac{1}{2}(1 - \cos\chi)\langle \hat{a}_s^\dagger \hat{a}_s \rangle + \frac{1}{2}(1 + \cos\chi)\langle \hat{a}_i^\dagger \hat{a}_i \rangle \tag{2.18}$$

$$+ \frac{1}{2}\sin\chi[\langle \hat{a}_s^\dagger \hat{a}_i \rangle + \langle \hat{a}_i^\dagger \hat{a}_s \rangle]. \tag{2.19}$$

When a coherent state is sent into one input port with the other left empty $(|\alpha_0 0\rangle)$, the single detector count rate is proportional to

$$\langle \hat{a}_{o_1}^\dagger \hat{a}_{o_1} \rangle = \frac{1}{2}|\alpha_0|^2(1 - \cos\chi). \tag{2.20}$$

This pattern has a visibility of one. For a two-photon entangled state, the single detector count rate has the value

$$\langle \hat{a}_{o_1}^\dagger \hat{a}_{o_1} \rangle = 1 \tag{2.21}$$

which is invariant under changes in χ. The single detector rate for the second detector has the form $\langle \hat{a}_{o_2}^\dagger \hat{a}_{o_2} \rangle = \frac{1}{2}|\alpha_0|^2(1 + \cos\chi)$ for coherent state input, and $\langle \hat{a}_{o_2}^\dagger \hat{a}_{o_2} \rangle = 1$ for a two-photon entangled state. Using these values, we can see that the accidental coincidence count rate for these states is

$$\langle \hat{a}_{o_1}^\dagger \hat{a}_{o_1} \rangle \langle \hat{a}_{o_2}^\dagger \hat{a}_{o_2} \rangle = \begin{cases} 1 & \text{for } |11\rangle \\[2mm] \frac{1}{4}|\alpha_0|^4 \sin^2\chi & \text{for} |\alpha_0 0\rangle \end{cases} \tag{2.22}$$

We can thus see that the coincidence rate naively expected from the second-order results is χ-dependent in the case of coherent state input and χ-independent in the case of two-photon entangled state input.

This result can be contrasted with the results for the fourth-order Mach-Zehnder interferometer [39], where the coincidence counts between the two output ports are detected. In this case the relevant quantity is the fourth-order cross-correlation function $\Gamma^{(2,2)}(\mathbf{r}_1, \mathbf{r}_2, \mathbf{r}_2, \mathbf{r}_1; t_1, t_2, t_2, t_1) \propto \langle \hat{a}_{o_1}^\dagger \hat{a}_{o_2}^\dagger \hat{a}_{o_2} \hat{a}_{o_1} \rangle$ which has the value

$$
\begin{aligned}
\langle \hat{a}_{o_1}^\dagger \hat{a}_{o_2}^\dagger \hat{a}_{o_2} \hat{a}_{o_1} \rangle =\ & \tfrac{1}{4}(1 - \cos^2\chi)[\langle \hat{a}_s^\dagger \hat{a}_s^\dagger \hat{a}_s \hat{a}_s \rangle + \langle \hat{a}_i^\dagger \hat{a}_i^\dagger \hat{a}_i \hat{a}_i \rangle] \\
& + \tfrac{1}{4}(1 - \cos\chi)^2 \langle \hat{a}_s^\dagger \hat{a}_i^\dagger \hat{a}_i \hat{a}_s \rangle \\
& + \tfrac{1}{4}(1 + \cos\chi)^2 \langle \hat{a}_i^\dagger \hat{a}_s^\dagger \hat{a}_s \hat{a}_i \rangle \\
& + \tfrac{1}{2}\sin\chi(1 + \cos\chi)[\langle \hat{a}_s^\dagger \hat{a}_s^\dagger \hat{a}_s \hat{a}_i \rangle - \langle \hat{a}_i^\dagger \hat{a}_s^\dagger \hat{a}_i \hat{a}_i \rangle] \\
& - \tfrac{1}{2}\sin^2\chi[\langle \hat{a}_s^\dagger \hat{a}_s^\dagger \hat{a}_i \hat{a}_i \rangle + \langle \hat{a}_s^\dagger \hat{a}_i^\dagger \hat{a}_s \hat{a}_i \rangle] \\
& + \tfrac{1}{2}\sin\chi(1 - \cos\chi)[\langle \hat{a}_s^\dagger \hat{a}_i^\dagger \hat{a}_i \hat{a}_i \rangle + \langle \hat{a}_s^\dagger \hat{a}_s^\dagger \hat{a}_i \hat{a}_s \rangle]
\end{aligned}
\tag{2.23}
$$

Figure 2.4: Mach-Zehnder interferometer single detector and joint detection probabilities. The probabilities are displayed as functions of the phase difference between the two interferometer arms. The joint detection probability (solid line) is dependent on the phase difference even though the single detector probability (dashed line) is constant.

For the states considered above, the coincidence count rate (Figure 2.4) is then found to be proportional to

$$\langle \hat{a}_{o_1}^\dagger \hat{a}_{o_2}^\dagger \hat{a}_{o_2} \hat{a}_{o_1} \rangle = \begin{cases} \frac{1}{4}|\alpha_0|^4 \sin^2\chi & \text{for } |\alpha_0 \ 0\rangle \\ \cos^2\chi & \text{for } |11\rangle \end{cases} \quad (2.24)$$

Both inputs produce a phase-dependent coincidence count rate. However, comparison to the accidental coincidence count rate $\langle \hat{a}_{o_1}^\dagger \hat{a}_{o_1} \rangle \langle \hat{a}_{o_2}^\dagger \hat{a}_{o_2} \rangle$ shows that the result with coherent state input is simply equal to the accidental rate, whereas the two-photon entangled state result significantly differs from the naively expected rate for that state.
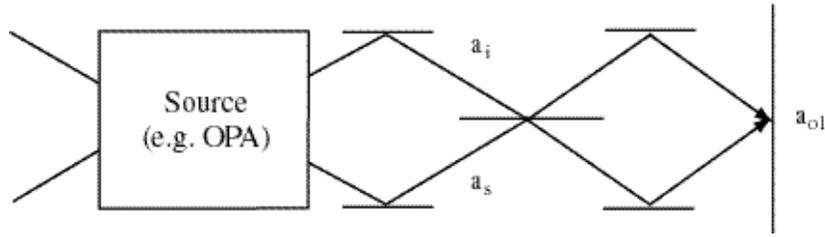
Figure 2.5: Quantum lithography configuration. The interferometric pattern is detected via two-photon absorption rather than coincidence count detection.

2.5 Quantum lithography

Two-photon states have been predicted to produce sub-Rayleigh-limit features in configurations like that shown in Figure 2.5 [6]. In this arrangement, source beams are sent into the input ports of a 50/50 beamsplitter, and the resulting beams are then recombined at an angle 2θ onto a two-photon absorber. The angular separation introduces an effective phase shift of $2kx\sin\theta$ between the two outputs from the beamsplitter, where x is the transverse coordinate along the observation plane. With conventional classical interferometric lithography, the resulting pattern has a minimum fringe spacing of $\lambda/2$ which occurs at grazing incidence $(\theta = \pi/2)$.

With an input of the form $|1\rangle|1\rangle$, the resulting pattern has a minimum fringe spacing that is decreased below this classical limit by a factor of 2 [6]. Spontaneous parametric downconversion has been proposed for use in this arrangement as a source of two-photon entangled states. The resulting reduction in fringe spacing can be seen in the following single-mode analysis.

The relationship between the source beams and the beams directed onto the two-photon absorber is given by

$$\hat{a}_1 = \frac{1}{\sqrt{2}} \left[\hat{a}_s - i\hat{a}_i \right] \tag{2.25}$$

$$\hat{a}_2 = \frac{1}{\sqrt{2}} \left[-i\hat{a}_s + \hat{a}_i \right]. \tag{2.26}$$

The phase shift between these two beams as they recombine at a location with transverse coordinate x can be written $\chi = 2kx \sin\theta$, where θ is the angle between the two beams. The field detected at this location can be represented with the annihilation operator $\hat{a}_3$ where

$$\hat{a}_3 = \hat{a}_1 + e^{i\chi}\hat{a}_2. \tag{2.27}$$

In terms of the input modes to the beamsplitter this expression can be written

$$\hat{a}_3 = \frac{1}{\sqrt{2}} \left[(1 - ie^{i\chi})\hat{a}_s + (-i + e^{i\chi})\hat{a}_i \right]. \tag{2.28}$$

To see the output generated by a two-photon entangled state input into the beamsplitter, we can evaluate $\langle \hat{a}_3^\dagger \hat{a}_3^\dagger \hat{a}_3 \hat{a}_3 \rangle$ using a state of the form $|1\rangle_s |1\rangle_i$. This gives the result

$$\langle \hat{a}_3^\dagger \hat{a}_3^\dagger \hat{a}_3 \hat{a}_3 \rangle = 2(1 + \cos 2\chi). \tag{2.29}$$
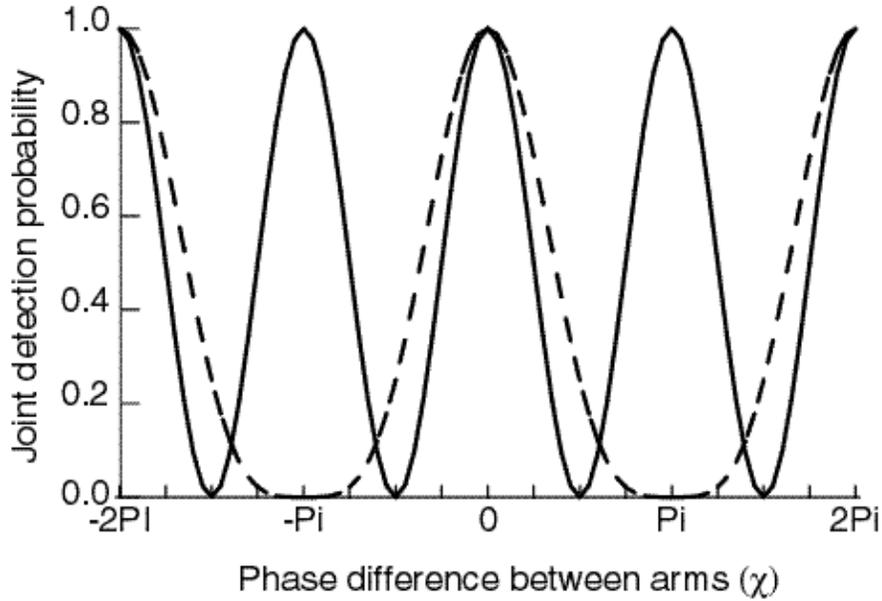
Figure 2.6: Quantum lithography output patterns produced by two-photon entangled state (solid line) and coherent state (dashed line) input fields. The patterns are shown as a function of $\chi = 2kx$ where x is the transverse coordinate in the observation plane and k is the wavevector of the writing beams. The pattern created with a two-photon entangled state input varies more rapidly with transverse position than the pattern created with the coherent state input.

We can see that the total coincidence count rate will vary as $2\chi = 4kx \sin \theta$, which is twice as rapid a dependence on χ as with standard classical techniques [6] (Figure 2.6). This rapid dependence has been interpreted in the context of the de Broglie wavelength of the photon pair, which is half the wavelength of the individual photons [62,16,63].

This reduction in fringe spacing beyond the Rayleigh limit has been demonstrated in principle in an experiment utilizing a beamsplitter and coincidence count detector in place of the two-photon absorbing substrate [8]. The $|2\rangle|0\rangle + |0\rangle|2\rangle$ state that can be generated by a $|1\rangle|1\rangle$ state followed by a beamsplitter
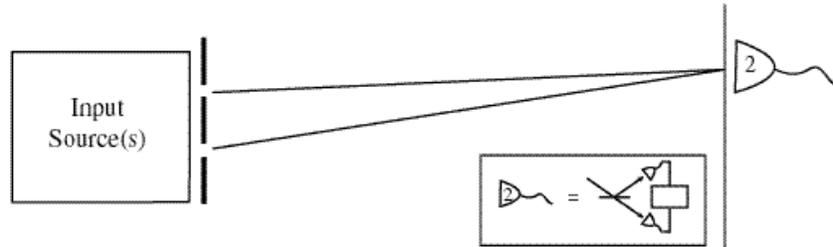
Figure 2.7: Quantum lithography in-principle realization. In-principle observation of reduced fringe width using two-photon entangled states. The entangled states are generated with a double slit placed after the parametric downconverter used to generate the observed photons. The experimental setup uses a beamsplitter and coincidence count detector in place of a two-photon absorbing substrate.

was instead generated with a double-slit mask placed after a parametric downconverter in such a manner that both of the downconverted photons exit through the same slit. The predicted change in spacing was observed when the slits were illuminated by the downconverter but not when the slits were illuminated by a coherent state input (Figure 2.7).

Reductions in effective wavelength with a fourth-order interferometric experiment have also been observed within the framework of de Broglie wavelength measurement [62]. A wavepacket of m photons can be considered to have a de Broglie wavelength of λ/m, where λ is the wavelength of the individual photons. The entangled states considered above thus have a de Broglie wavelength half that of the photons they contain. When used in a fourth-order interferometric arrangement such as a beamsplitter and coincidence count detector placed after a double slit, the resulting pattern has a spacing consistent with the $\lambda/2$ de

Broglie wavelength as long as the spatial profile of the beam is of the appropriate shape [62].

It should be noted that classical methods have also been proposed to achieve a reduction in fringe spacing of this size [64]. However, the possible extension of this method to $2m$-photon entangled states, with the concomitant improvement by a factor of $2m$, makes quantum lithography an area of special interest.

2.6   Conclusion

In this chapter, we have reviewed results obtained with two-photon entangled states in the Hong-Ou-Mandel interferometer, Mach-Zehnder interferometer, and quantum lithography configurations. Two-photon entangled states used as inputs to the Hong-Ou-Mandel interferometer exhibit a reduction in coincidence counts below the level expected based on the single detector rates. In the Mach-Zehnder interferometer, the coincidence count rate obtained with two-photon entangled state input exhibits a variation with phase difference between the two arms of the interferometer that is not present in the single-detector rates; this behavior can be contrasted to that obtained with coherent state input, where the coincidence rate simply equals the product of the single detector rates. Two-photon entangled states in the quantum lithography configuration produce a pattern which varies as $\lambda/4$ rather than the $\lambda/2$ variation produced by conventional classical interferometric lithography. In each case, two-photon entangled states produce results

that significantly differ from those produced with coherent state input. In the next chapter, we will consider whether the interesting effects associated with two-photon entangled states persist when the gain of the parametric downconversion source used to produce these two-photon states is increased.

Chapter 3

High-Gain Contributions to Fourth-Order Interferometric Output

3.1 Introduction

The output of a vacuum-initiated parametric downconverter consists of a superposition of states containing multiple photon pairs, with one member of each pair emitted into the signal mode and the other into the idler mode. These states can be written in the form $|m\rangle_s|m\rangle_i$. The two-photon entangled state experiments described in the previous chapter are conducted at gain levels low enough that the output can be considered to consist only of the vacuum and states containing a single photon pair (i.e. $|1\rangle_s|1\rangle_i$). These experiments are typically conducted under conditions with low count rates, with the rarity of photon creation events ensuring that multiple pair states can be neglected.

In applications such as quantum lithography, these low count rates, combined

with the low cross-section for two-photon absorption, are of practical concern. While the correlation between the photons in an entangled pair may lead to two-photon absorption rates that are linear in intensity [65,66], it is nevertheless unclear whether low detection rates will be problematic in a practical context. Raising gain levels, with the attendant production of additional photon pairs, is a seemingly straightforward way of circumventing this problem, however it is also to be expected that these additional photon pairs will alter the character of the fourth-order interferometric effects.

In this chapter, the effect of these additional photon pairs on the patterns produced by selected fourth-order interferometric arrangements is analyzed. We begin by discussing the limitations presented by low-gain sources in certain experimental configurations. The model used for describing the output of spontaneous parametric downconversion in the high-gain limit is then outlined. The effect of increased single-pass gain on the output of a Hong-Ou-Mandel interferometer is presented, and the result generalized to any fourth-order four-port interferometer. This model is then applied to the Mach-Zehnder and quantum lithography configurations. The effect of increased gain in these situations is presented.

We find that in the Hong-Ou-Mandel and Mach-Zehnder arrangements the presence of multiple photon pairs causes the disappearance of effects such as coincidence count cancellation, but that in the quantum lithography configuration desirable effects are preserved even in the high-gain limit. These results are in-

terpreted in the context of multiple photon pair contributions to interferometric output.

3.2 Parametric downconversion as a multiphoton source

At low gain levels, spontaneous parametric downconversion is a source of individual pairs of entangled photons. In the simplest case, when only a single signal and idler mode are being considered, this output can be written $|1>_s |1>_i$. When gain is increased, multiple pairs may be generated, leading to an output that is a superposition of states of the form $|m>_s |m>_i$. As the single pass gain parameter is increased from low values where the mean photon number is much less than one to the regime where there is a significant probability of states with photon numbers much greater than one, the interferometric output is modified in a continuous fashion from a biphoton-like result to one applicable when multiple photons are present. The impact of this transition on important properties such as interference visibility can then be determined.

A simple model for parametric downconversion can be used to investigate the transition from single photon pairs to photon numbers $>> 1$ (Figure 3.1). The interaction between the signal mode $\hat{a}_s$ and idler mode $\hat{a}_i$ can be described by the
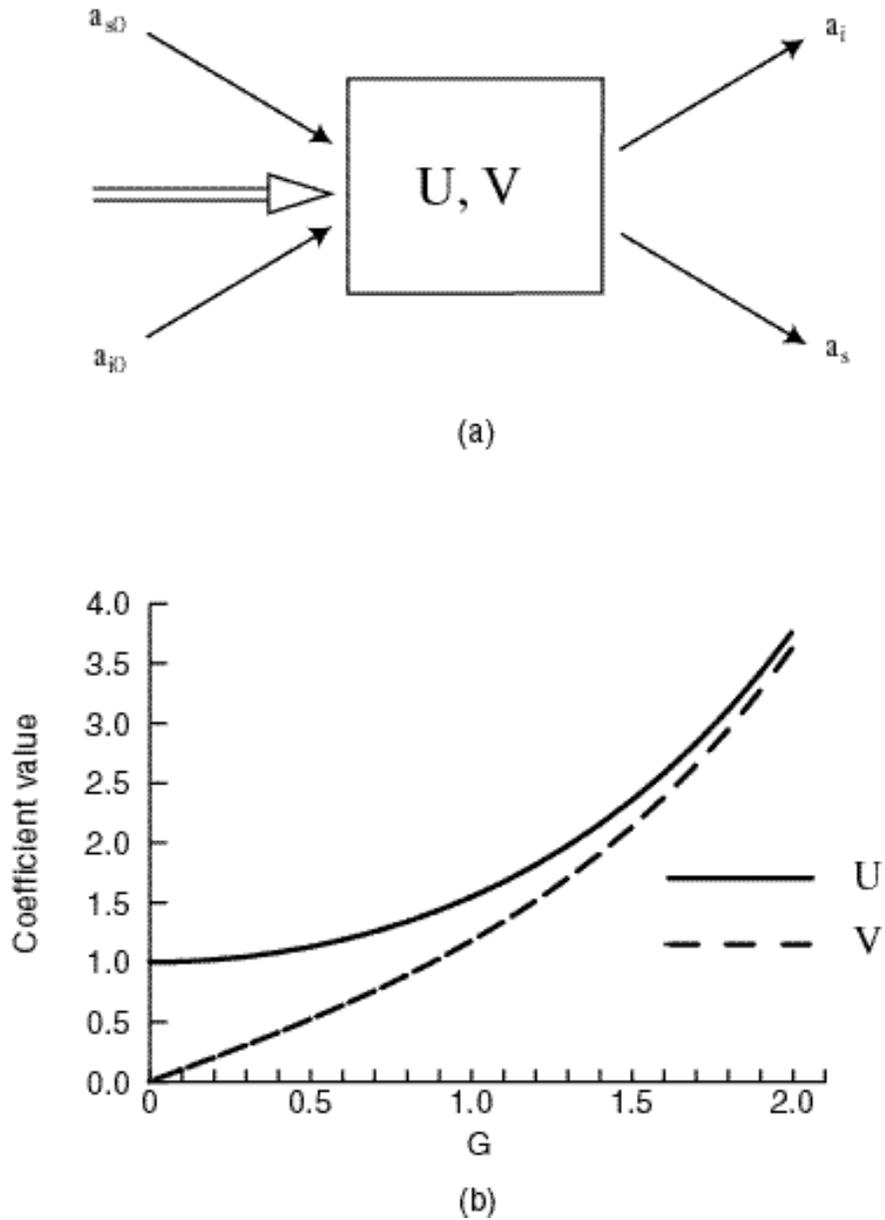
Figure 3.1: Parametric downconversion. (a) The downconversion process couples a single signal mode to a single idler mode. (b) The coefficients U and V describe the interaction. The input may be initiated by seeding or by vacuum state input.

interaction Hamiltonian

$$\hat{H} = \hbar g[\hat{a}_s^\dagger \hat{a}_i^\dagger v_0 + h.c.] \tag{3.1}$$

The corresponding equations of motion are

$$\frac{d\hat{a}_s}{dt} = -igv_0\hat{a}_i^\dagger \tag{3.2}$$

$$\frac{d\hat{a}_i}{dt} = -igv_0\hat{a}_s^\dagger \tag{3.3}$$

and have the solutions

$$\hat{a}_s = U\hat{a}_{s0} + V\hat{a}_{i0}^\dagger \tag{3.4}$$

$$\hat{a}_i = U\hat{a}_{i0} + V\hat{a}_{s0}^\dagger \tag{3.5}$$

where

$$U = \cosh G \tag{3.6}$$

$$V = -i\exp(i\theta)\sinh G, \tag{3.7}$$

G represents the gain of the process and is dependent on the pump amplitude and the size of the material nonlinearity. This gain factor may be written as $G = g|v_0|t$ where t is the interaction time, $|v_0|$ is the pump amplitude, and g is proportional to $\chi^{(2)}$ (Figure 3.1).
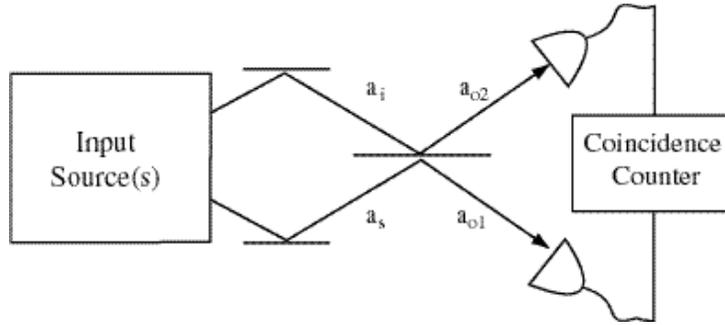
Figure 3.2: Layout of a Hong-Ou-Mandel interferometer.

3.3 Effect of increased gain on the Hong-Ou-Mandel interferometer

Before considering the effect of increasing gain on the output of a generalized fourth-order interferometer, we can consider the effect of increased gain on a well-analyzed fourth-order phenomenon-the reduction of coincidence count levels in a Hong-Ou-Mandel interferometer.

In the Hong-Ou-Mandel interferometer [51], source beams are directed into the input ports of a 50/50 beamsplitter and a photon counting detector is placed at each output (Fig. 3.2). When the low-gain output generated by spontaneous parametric downconversion is used as an input, the rate of coincidence counts drops to zero for equal pathlengths. If a pathlength difference between the two input arms is introduced, the coincidence count rate becomes nonzero; as the difference increases, the rate increases to its asymptotic value. We can look at the absence or presence of coincidence counts in the equal path configuration as

gain is increased to monitor the impact of multiphoton states on fourth-order interferometric effects.

The two beams from the parametric amplifier are directed into the two input ports of the 50:50 beamsplitter shown in Figure 3.2, where they are combined. Using the beamsplitter relationships

$$\hat{a}_{o_1} = \frac{1}{\sqrt{2}} \left[-\hat{a}_s + i\hat{a}_i \right] \tag{3.8}$$

$$\hat{a}_{o_2} = \frac{1}{\sqrt{2}} \left[i\hat{a}_s - \hat{a}_i \right], \tag{3.9}$$

the output fields are expressed as

$$\hat{a}_{o_1} = \frac{1}{\sqrt{2}} \left[(U\hat{a}_{s0} + V\hat{a}_{i0}^\dagger) - i(U\hat{a}_{i0} + V\hat{a}_{s0}^\dagger) \right] \tag{3.10}$$

and

$$\hat{a}_{o_2} = \frac{1}{\sqrt{2}} \left[-i(U\hat{a}_{s0} + V\hat{a}_{i0}^\dagger) + (U\hat{a}_{i0} + V\hat{a}_{s0}^\dagger) \right]. \tag{3.11}$$

The coincidence count rate is given by $\langle \hat{a}_{o_1}^\dagger \hat{a}_{o_2}^\dagger \hat{a}_{o_2} \hat{a}_{o_1} \rangle$ and for a vacuum state input to the material, becomes

$$\langle 0, 0 | \hat{a}_{o_1}^\dagger \hat{a}_{o_2}^\dagger \hat{a}_{o_2} \hat{a}_{o_1} | 0, 0 \rangle = |V|^4 \tag{3.12}$$
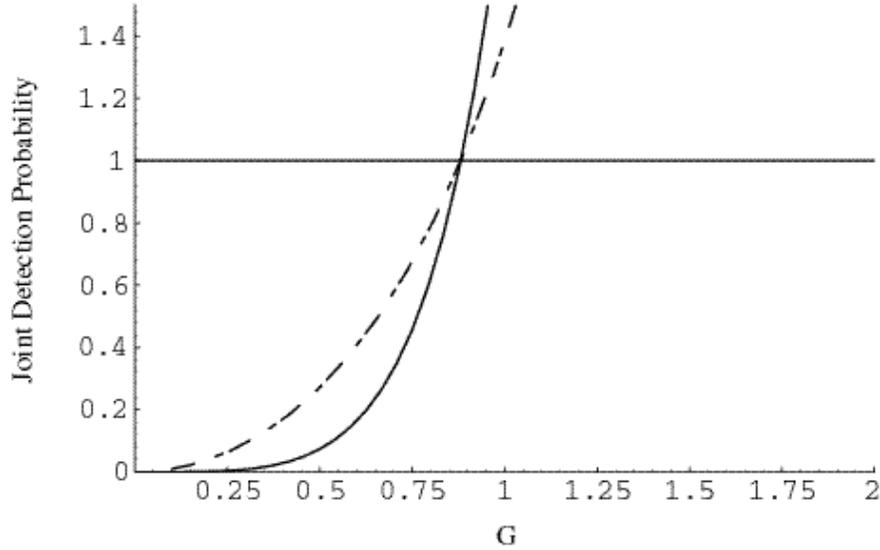
Figure 3.3: Hong-Ou-Mandel interferometer coincidence count rate as a function of gain. Joint detection probability (solid) at the beamsplitter output ports normalized to the single detector probability (dashed line) as a function of source nonlinear interaction strength. The horizontal line indicates the joint detection probability normalized to the product of single detection probabilities.

This implies that the disappearance of the coincidence count rate is dependent on the specific values of U and V and is not in general zero.

The coefficients U and V are given by Eqns. 4.3 and 4.4. From these quantities, the coincidence count rate can be plotted as a function of the interaction strength G as shown in Figure 3.3. We can see that the coincidence rate deviates significantly from zero even at values of G where the mean output photon number is approximately one.

Given a vacuum input, the output state arising from a parametric downconverter can be written as the sum of states of the form $|n, n\rangle$ [18]. As the gain is increased, the relative contribution of states with greater n also increases. The

presence of these states leads to a deviation of the coincidence count rate from its

value of 0 for $|1, 1\rangle$, as seen in Eq. 3.12. It is straightforward to show that a state

$|\psi\rangle_1 = |n, n\rangle$ injected into two ports of a beamsplitter described by Eqns. 3.8 and

3.9 has a coincidence count rate at the output $\langle \hat{a}_{o_1}^\dagger \hat{a}_{o_2}^\dagger \hat{a}_{o_2} \hat{a}_{o_1} \rangle = \frac{1}{2}n(n-1)$. For

a $|1, 1\rangle$ input this quantity vanishes; if a $|2, 2\rangle$ state is input into a beamsplitter,

the joint detection probability is no longer 0. This is also true for any $n > 1$. As

the nonlinear interaction strength is increased and more photons are produced,

components such as these will make nonnegligible contributions to the output

from the nonlinear material. Even at values of the single-pass gain where the

mean photon number is smaller than one, states such as $|2, 2\rangle$ are present; thus

the coincidence count rate only truly vanishes when the single-pass gain goes to

zero.

3.4   Multi-pair fourth-order interferometry

From the results in the previous section, we can see that the presence of additional

photon pairs in the input to a particular fourth-order interferometric configura-

tion led to the disappearance of a biphoton-related phenomenon. In this section,

a generalized four-port fourth-order interferometer with multiphoton input is con-

sidered, allowing a unified treatment of the HOMI, Mach-Zehnder, and quantum

lithography configurations. The following calculation separates interferometer-

dependent coefficients from input-state-dependent expectation values, showing explicitly the origin of additional contributions arising from multiple pair states.

We begin by using the HOMI to identify the specific contributions introduced by the presence of multiple pairs, examining in this case the output from a beamsplitter with variable reflection and transmission properties. For a beamsplitter describable by

$$\hat{a}_{o_1} = \sqrt{R}\hat{a}_s - i\sqrt{T}\hat{a}_i \tag{3.13}$$

$$\hat{a}_{o_2} = -i\sqrt{T}\hat{a}_s + \sqrt{R}\hat{a}_i, \tag{3.14}$$

the coincidence count rate is given by

$$
\begin{aligned}
\langle \hat{a}_{o_1}^\dagger \hat{a}_{o_2}^\dagger \hat{a}_{o_2} \hat{a}_{o_1} \rangle \;=\; & RT\langle \hat{a}_s^\dagger \hat{a}_s^\dagger \hat{a}_s \hat{a}_s \rangle + R^2 \langle \hat{a}_s^\dagger \hat{a}_i^\dagger \hat{a}_i \hat{a}_s \rangle \\
& + T^2 \langle \hat{a}_i^\dagger \hat{a}_s^\dagger \hat{a}_s \hat{a}_i \rangle + RT\langle \hat{a}_i^\dagger \hat{a}_i^\dagger \hat{a}_i \hat{a}_i \rangle \\
& + 2\ RT\langle \hat{a}_s^\dagger \hat{a}_s^\dagger \hat{a}_i \hat{a}_i \rangle - 2\ RT\langle \hat{a}_s^\dagger \hat{a}_i^\dagger \hat{a}_s \hat{a}_i \rangle.
\end{aligned}
\tag{3.15}
$$

From the first four terms in this expression we can identify the four paths by which coincidence counts can be generated. These paths are shown in Figure 3.4. Paths (b) and (c) are the only paths that are present when the input is a biphoton. Path (b) corresponds to both input photons being reflected; path (c) corresponds to both input photons being transmitted. Paths (a) and (d) are present if more than one pair is present at the interferometer input. Path (a) arises when two photons from the signal arm are detected at the output, while path (d) arises when two
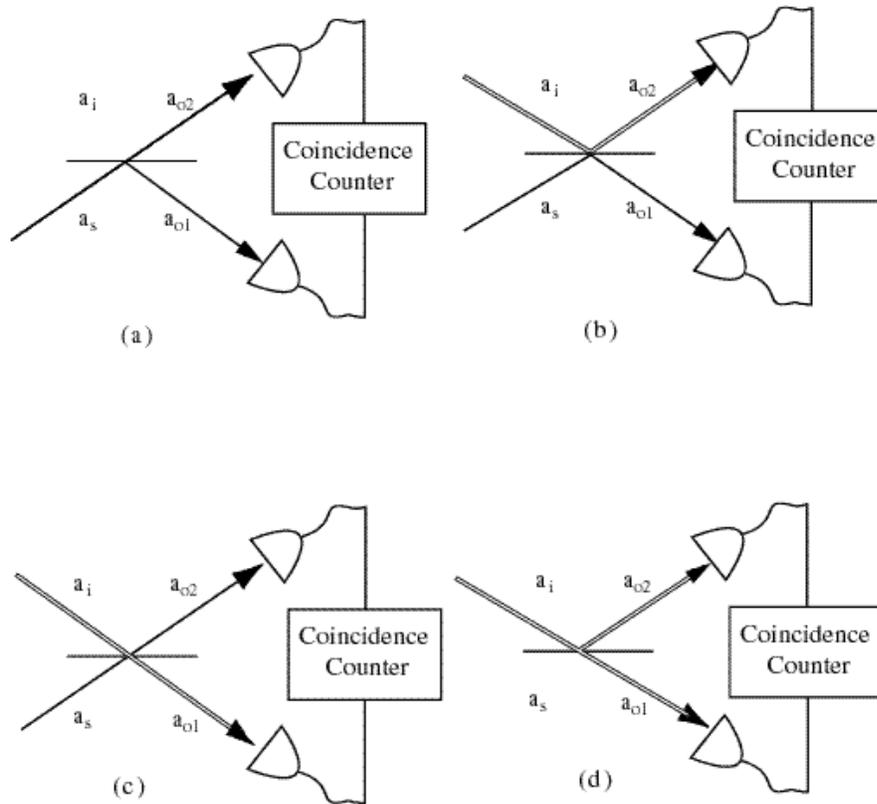
Figure 3.4: Possible contributions to the Hong-Ou-Mandel interferometer coincidence count rate. Processes (b) and (c) are present at both low and high gain levels. Processes (a) and (d) are not present when there is only one photon per mode.

photons from the idler arm are detected. In both cases one photon is reflected while the other is transmitted. The remaining two terms in Equation 3.15 reflect interference between different paths. For a $|1, 1 >$ state, the first, fourth, and fifth terms are zero, which is consistent with the identification of paths (a) and (d) with terms present only if multiple pairs are at the input.

We can now analyze a generalized four-port interferometer. Such an interferometer can be described with the relationships

$$\begin{pmatrix} \hat{a}_{o_1} \\ \hat{a}_{o_2} \end{pmatrix} = \begin{pmatrix} A & B \\ C & D \end{pmatrix} \begin{pmatrix} \hat{a}_s \\ \hat{a}_i \end{pmatrix} \tag{3.16}$$

where $\hat{a}_s$ and $\hat{a}_i$ are the input signal and idler modes and $\hat{a}_{o_1}$ and $\hat{a}_{o_2}$ are output

modes. The joint detection probability is then given by

$$
\begin{aligned}
\langle \hat{a}_{o_1}^\dagger \hat{a}_{o_2}^\dagger \hat{a}_{o_2} \hat{a}_{o_1} \rangle \;=\; & |C|^2 |A|^2 \langle \hat{a}_s^\dagger \hat{a}_s^\dagger \hat{a}_s \hat{a}_s \rangle \\
& + |D|^2 |A|^2 \langle \hat{a}_s^\dagger \hat{a}_i^\dagger \hat{a}_i \hat{a}_s \rangle \\
& + |C|^2 |B|^2 \langle \hat{a}_i^\dagger \hat{a}_s^\dagger \hat{a}_s \hat{a}_i \rangle \\
& + |D|^2 |B|^2 \langle \hat{a}_i^\dagger \hat{a}_i^\dagger \hat{a}_i \hat{a}_i \rangle \\
& + 2\;\mathrm{Re} C^* A^* D A \langle \hat{a}_s^\dagger \hat{a}_s^\dagger \hat{a}_i \hat{a}_s \rangle \\
& + 2\;\mathrm{Re} C^* A^* C B \langle \hat{a}_s^\dagger \hat{a}_s^\dagger \hat{a}_s \hat{a}_i \rangle \\
& + 2\;\mathrm{Re} C^* A^* D B \langle \hat{a}_s^\dagger \hat{a}_s^\dagger \hat{a}_i \hat{a}_i \rangle \\
& + 2\;\mathrm{Re} D^* A^* C B \langle \hat{a}_s^\dagger \hat{a}_i^\dagger \hat{a}_s \hat{a}_i \rangle \\
& + 2\;\mathrm{Re} D^* A^* D B \langle \hat{a}_s^\dagger \hat{a}_i^\dagger \hat{a}_i \hat{a}_i \rangle \\
& + 2\;\mathrm{Re} C^* B^* D B \langle \hat{a}_i^\dagger \hat{a}_s^\dagger \hat{a}_i \hat{a}_i \rangle
\end{aligned}
\tag{3.17}
$$

By analogy with the HOMI calculation, we can identify the expectation values present in the first four terms with the individual contributions of the four paths shown in Figure 3.4. The four paths can be grouped into two types: single-input paths, in which the detected photons arise from only one input arm, and dual-input paths, in which both input arms contribute one photon. Paths (b) and (c) are dual-input paths and differ only in the specific mapping of each input arm onto the output arms. These paths are the only paths present when the input is a biphoton. The single-input paths (a) and (d) are present when multiple-photon inputs are used. These paths are not present with a biphoton input and,

when introduced by increasing gain, contribute to a degradation of visibility in the Hong-Ou-Mandel configuration. The remaining six terms arise from interference between each of these paths; for many input states most of these terms vanish.

This situation is summarized in Table 3.1, which shows the value of each of the terms in Equation 3.17 for different input states. For states generated by spontaneous parametric downconversion, all of the interference terms are zero except for the term generated by the interference of the two paths in which one signal and one idler photon are detected. Furthermore, for a biphoton input, the first and fourth terms, corresponding to the single-input paths, are also zero as they require at least two photons in the involved input arm. We can also note that all of the terms are present if coherent state inputs are used. In the quantum lithography configuration, we will see that the presence of these additional terms with coherent state input leads to components with undesired wider fringe spacing.

In addition to the expectation values shown in Table 3.1, the value of the joint detection probability is determined by the interferometer-dependent coefficients that multiply each expectation value (e.g. $|C|^2|A|^2$ for $\langle \hat{a}_s^\dagger \hat{a}_s^\dagger \hat{a}_s \hat{a}_s \rangle$). The values of these coefficients for various interferometers are shown in Table 3.2. In the case of an OPA, the "interferometer" is simply the direct mapping of the signal to output 1 and the idler to output 2, that is, $A = D = 1$, $B = C = 0$, while for

		$|1\,1\rangle$	$|m\,m\rangle$	$|\alpha_0\,\alpha_0\rangle$	OPA
	$\langle a_s^\dagger a_s^\dagger a_s a_s\rangle$	0	$m(m-1)$	$|\alpha_0|^4$	$2(\bar{m})^2$
	$\langle a_s^\dagger a_i^\dagger a_i a_s\rangle$	1	m^2	$|\alpha_0|^4$	$2(\bar{m})^2 + \bar{m}$
	$\langle a_i^\dagger a_s^\dagger a_s a_i\rangle$	1	m^2	$|\alpha_0|^4$	$2(\bar{m})^2 + \bar{m}$
	$\langle a_i^\dagger a_i^\dagger a_i a_i\rangle$	0	$m(m-1)$	$|\alpha_0|^4$	$2(\bar{m})^2$
	$\langle a_s^\dagger a_s^\dagger a_i a_s\rangle$	0	0	$|\alpha_0|^4$	0
	$\langle a_s^\dagger a_s^\dagger a_s a_i\rangle$	0	0	$|\alpha_0|^4$	0
	$\langle a_s^\dagger a_s^\dagger a_i a_i\rangle$	0	0	$|\alpha_0|^4$	0
	$\langle a_s^\dagger a_i^\dagger a_s a_i\rangle$	1	m^2	$|\alpha_0|^4$	$2(\bar{m})^2 + \bar{m}$
	$\langle a_s^\dagger a_i^\dagger a_i a_i\rangle$	0	0	$|\alpha_0|^4$	0
	$\langle a_i^\dagger a_s^\dagger a_i a_i\rangle$	0	0	$|\alpha_0|^4$	0

single-input terms = both detected photons arise from a single input arm

dual-input terms = detected photons arise from both input arms

Table 3.1: Coincidence count rate contributions (Eq. 3.17) for various input states. The diagrammatic representation for each expectation value is shown on the left. Here "$|mm\rangle$" designates the situation in which exactly m photons fall onto each input port, "$|\alpha_0\alpha_0\rangle$" the situation in which the same coherent state falls onto each input port, and "OPA" the situation in which the signal and idler beams from an optical parametric amplifier are used as inputs.

		OPA	HOMI	MZ	QL
	$|C|^2|A|^2$	0	1/4	$1/4 \, (1-\cos^2\chi)$	$(1+\sin\chi)^2$
	$|D|^2|A|^2$	1	1/4	$1/4 \, (1-\cos\chi)^2$	$1-\sin^2\chi$
	$|C|^2|B|^2$	0	1/4	$1/4 \, (1+\cos\chi)^2$	$1-\sin^2\chi$
	$|D|^2|B|^2$	0	1/4	$1/4 \, (1-\cos^2\chi)$	$(1-\sin\chi)^2$
	$2\mathrm{Re}[C^*A^*DA]$	0	0	$-1/2 \, \sin\chi \, (1-\cos\chi)$	$2\cos\chi \, (1+\sin\chi)$
	$2\mathrm{Re}[C^*A^*CB]$	0	0	$1/2 \, \sin\chi \, (1+\cos\chi)$	$2\cos\chi \, (1+\sin\chi)$
	$2\mathrm{Re}[C^*A^*DB]$	0	1/2	$-1/2 \, \sin^2\chi$	$2\cos^2\chi$
	$2\mathrm{Re}[D^*A^*CB]$	0	-1/2	$-1/2 \, \sin^2\chi$	$2\cos^2\chi$
	$2\mathrm{Re}[D^*A^*DB]$	0	0	$1/2 \, \sin\chi \, (1-\cos\chi)$	$2\cos\chi \, (1-\sin\chi)$
	$2\mathrm{Re}[C^*B^*DB]$	0	0	$-1/2 \, \sin\chi \, (1+\cos\chi)$	$2\cos\chi \, (1-\sin\chi)$

 single-input terms = both detected photons arise from a single input arm
 dual-input terms = detected photons arise from both input arms

Table 3.2: Coincidence count rate coefficients for various interferometers. For four different situations (listed at the top) the coefficient of the quantum expectation value of each contribution (listed on the left along with its diagrammatic representation) to Eq. 3.17 is given. OPA refers to the joint detection probability at the output of an optical parametric amplifier, HOMI refers to the joint detection probability at the output of a 50/50 beamsplitter, and QL refers to the two-photon absorption rate at the recording plane in a quantum lithography configuration.

the HOMI, the transfer matrix elements are given by

$$A = D = \frac{1}{\sqrt{2}} \tag{3.18}$$

$$B = C = \frac{-i}{\sqrt{2}}. \tag{3.19}$$

In the case of a measurement made directly at the outputs of an optical parametric amplifier, Equation 3.17 reduces to $\langle \hat{a}_s^\dagger \hat{a}_i^\dagger \hat{a}_i \hat{a}_s \rangle$, which is simply the joint detection probability for the signal and idler modes. From Table 3.1, we can see that, as expected, the joint detection rate from the parametric amplifier is increased over the level produced by coherent state input. The second column in Table 3.2 shows the Hong-Ou-Mandel interferometer coefficients. The negative sign on the dual-input interference term reflects the phase relationship that allows quantum interference to reduce the observed coincidence count rate. The single-input interference term $\langle \hat{a}_s^\dagger \hat{a}_s^\dagger \hat{a}_i \hat{a}_i \rangle$ is also nonzero; however this term is zero for parametric amplifier outputs at both biphoton and high-gain levels. For coherent state input this term is present and leads to a net coincidence rate that shows no interference properties.

Using this framework to calculate the Hong-Ou-Mandel interferometer joint detection probability gives

$$
\begin{aligned}
\langle \hat{a}_{o_1}^\dagger \hat{a}_{o_2}^\dagger \hat{a}_{o_2} \hat{a}_{o_1} \rangle &= \tfrac{1}{4}[\langle \hat{a}_s^\dagger \hat{a}_s^\dagger \hat{a}_s \hat{a}_s \rangle + \langle \hat{a}_s^\dagger \hat{a}_i^\dagger \hat{a}_i \hat{a}_s \rangle + \langle \hat{a}_i^\dagger \hat{a}_s^\dagger \hat{a}_s \hat{a}_i \rangle + \langle \hat{a}_i^\dagger \hat{a}_i^\dagger \hat{a}_i \hat{a}_i \rangle] \\
&\quad + \tfrac{1}{2}[\langle \hat{a}_s^\dagger \hat{a}_s^\dagger \hat{a}_i \hat{a}_i \rangle - \langle \hat{a}_s^\dagger \hat{a}_i^\dagger \hat{a}_s \hat{a}_i \rangle]
\end{aligned}
\tag{3.20}
$$
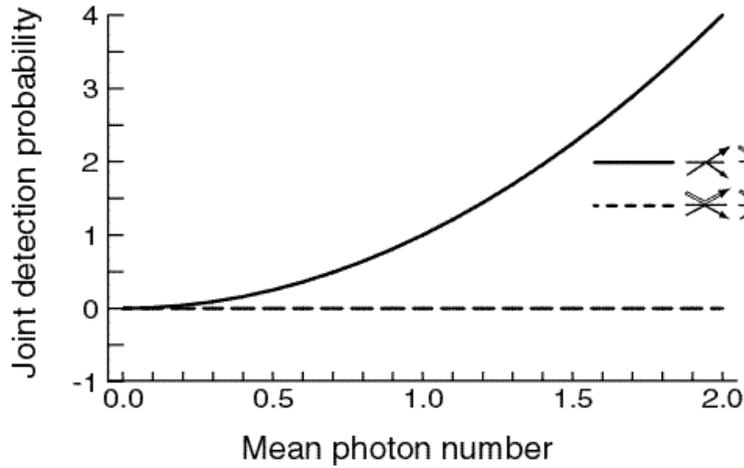
Figure 3.5: Single-input (solid line) and dual-input (dashed line) contributions to the Hong-Ou-Mandel interferometer coincidence count rate. The dual-input contribution vanishes at all values of the mean photon number.

with the following results for each of the states considered. For a biphoton input, $\langle \hat{a}_{o_1}^\dagger \hat{a}_{o_2}^\dagger \hat{a}_{o_2} \hat{a}_{o_1} \rangle = 0$. For a Fock states in both signal and idler arms, the joint detection probability is $\frac{1}{2} m(m-1)$ and for a parametric amplifier the probability is $\overline{m}^2$. Rewriting this last result using $\overline{m} = |V|^2$ returns the previously obtained result of $|V|^4$ (Eq. 3.12).

Figure 3.5 shows this result with the contributions of the single- and dual-input terms displayed separately. The dual-input terms combine to give a net probability of zero; these are the only terms present for a biphoton input, leading to the coincidence count cancellation that is the hallmark of the Hong-Ou-Mandel interferometer. The single-input terms that become dominant as the photon number increases lead to a joint detection probability of $\overline{m}^2$ for the parametric amplifier. We can note that this has the same form as the probability for a coherent state

input $\langle \hat{a}_{o_1}^\dagger \hat{a}_{o_2}^\dagger \hat{a}_{o_2} \hat{a}_{o_1} \rangle = |\alpha_0|^4 = \overline{m}^2$, with both being equal to the product of the single detector probabilities. Inspection of Tables 3.1 and 3.2 shows that this apparent similarity arises through the contribution of different terms in each case.

3.5 Multi-pair Mach-Zehnder interferometry

The analysis of the Hong-Ou-Mandel interferometer in the earlier sections was restricted to the case where the signal and idler beams are each emitted into a single mode. Because variations in the frequency of the signal and idler photons are not considered, the effect of a phase difference between the two paths in a HOMI cannot be analyzed with this simple model and thus the effect of increased gain on the interference pattern as a whole cannot be analyzed. In the Mach-Zehnder configuration (Figure 2.3), however, the presence of an additional recombination of the beams at the second beamsplitter allows us to analyze the visibility within the constraints of this model.

In this section the generalized formalism of the previous section is applied to the fourth-order Mach-Zehnder interferometer, which is described by the matrix elements

$$A = -D = \frac{1}{2}(1 - e^{i\chi}) \tag{3.21}$$

$$B = C = \frac{-i}{2}(1 + e^{i\chi}) \tag{3.22}$$

where χ is the phase shift between the two arms of the interferometer. Table 3.2 shows the relevant coefficients for joint detection probability given these matrix elements. The dual-input terms and the single-input terms have different dependences on χ, implying that the relative contributions of these terms can affect the visibility of the fourth-order interference pattern. This can be seen by writing out the expression for the joint detection probability

$$
\begin{aligned}
\langle \hat{a}_{o_1}^\dagger \hat{a}_{o_2}^\dagger \hat{a}_{o_2} \hat{a}_{o_1} \rangle &= \tfrac{1}{4}(1 - \cos^2\chi)[\langle \hat{a}_s^\dagger \hat{a}_s^\dagger \hat{a}_s \hat{a}_s \rangle + \langle \hat{a}_i^\dagger \hat{a}_i^\dagger \hat{a}_i \hat{a}_i \rangle] \\
&\quad + \tfrac{1}{4}(1 - \cos\chi)^2 \langle \hat{a}_s^\dagger \hat{a}_i^\dagger \hat{a}_i \hat{a}_s \rangle \\
&\quad + \tfrac{1}{4}(1 + \cos\chi)^2 \langle \hat{a}_i^\dagger \hat{a}_s^\dagger \hat{a}_s \hat{a}_i \rangle \\
&\quad + \tfrac{1}{2}\sin\chi(1 + \cos\chi)[\langle \hat{a}_s^\dagger \hat{a}_s^\dagger \hat{a}_s \hat{a}_i \rangle - \langle \hat{a}_i^\dagger \hat{a}_s^\dagger \hat{a}_i \hat{a}_i \rangle] \\
&\quad - \tfrac{1}{2}\sin^2\chi[\langle \hat{a}_s^\dagger \hat{a}_s^\dagger \hat{a}_i \hat{a}_i \rangle + \langle \hat{a}_s^\dagger \hat{a}_i^\dagger \hat{a}_s \hat{a}_i \rangle] \\
&\quad + \tfrac{1}{2}\sin\chi(1 - \cos\chi)[\langle \hat{a}_s^\dagger \hat{a}_i^\dagger \hat{a}_i \hat{a}_i \rangle - \langle \hat{a}_s^\dagger \hat{a}_s^\dagger \hat{a}_i \hat{a}_s \rangle]
\end{aligned}
\tag{3.23}
$$

Using the expectation values displayed in Table 3.2, this expression reduces to

$$
\langle \hat{a}_{o_1}^\dagger \hat{a}_{o_2}^\dagger \hat{a}_{o_2} \hat{a}_{o_1} \rangle = \cos^2\chi
\tag{3.24}
$$

for a biphoton input,

$$
\langle \hat{a}_{o_1}^\dagger \hat{a}_{o_2}^\dagger \hat{a}_{o_2} \hat{a}_{o_1} \rangle = \frac{1}{2}m(m - 1) + \frac{1}{2}m(m + 1)\cos^2\chi
\tag{3.25}
$$
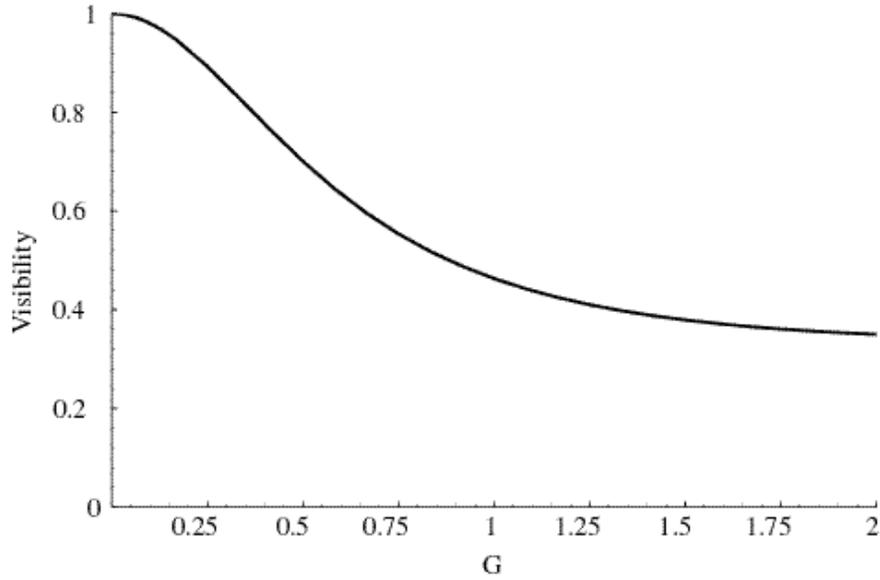
Figure 3.6: Mach-Zehnder fourth-order interference visibility for the parametric amplifier as a function of source nonlinear interaction strength.

for a $|mm\rangle$ input, and

$$\langle \hat{a}_{o_1}^\dagger \hat{a}_{o_2}^\dagger \hat{a}_{o_2} \hat{a}_{o_1} \rangle = \overline{m}^2 + \overline{m}(\overline{m}+1)\cos^2\chi \qquad (3.26)$$

for a parametric amplifier input. The corresponding visibilities are 1 for a biphoton, $(m+1)/(3m-1)$ for a $|mm\rangle$ state, and $(\overline{m}+1)/(3\overline{m}+1)$ for a parametric amplifier. As expected, the largest visibility occurs with a biphoton input. A multiple pair input state has a visibility that decreases with increasing photon number in each input mode. As expected, the parametric amplifier source has visibility that is dependent on the mean photon number $\overline{m}$, approaching unity for low $\overline{m}$ and tending to $1/3$ as $\overline{m}$ increases (Fig. 3.6).

A coherent state input leads to contributions from all terms, giving a joint de-

tection probability of $\langle \hat{a}_{o_1}^\dagger \hat{a}_{o_2}^\dagger \hat{a}_{o_2} \hat{a}_{o_1} \rangle = |\alpha_0|^4 \cos^2\chi$. This has the same dependence on χ as that for a biphoton input and a visibility of 1. While the introduction of single-input terms led to a decrease in visibility for high-gain parametric amplifier input, the presence of additional terms in the coherent state case does not lead to low visibility, but rather to a visibility of 1 even with large mean photon number.

3.6 Quantum lithography with multiple photon pairs

In the HOMI configuration we have seen that the introduction of multiple pair states as parametric amplifier gain is increased leads to fourth-order interferometric output that resembles that produced by coherent state input. With the fourth-order Mach-Zehnder interferometer, the introduction of multiple pair states lead to a result with a visibility that not only is lower than that obtained with biphoton input, but also lower than that obtained with coherent state input. In the context of quantum lithography (Fig. 2.5), we will see that although increased gain leads to a degradation in visibility relative to that obtained with biphoton input, the desirable sub-Rayleigh pattern characteristics are preserved with multiple pair states and are not preserved with coherent state input [67]. In particular, while the interplay of the interferometer coefficients and the states' expectation values lead to similar results with coherent and parametric amplifier inputs for

the HOMI, the different weightings for each state present in the quantum lithography case lead to qualitatively different results for the parametric amplifier and coherent output states, even at high gain.

The matrix elements for quantum lithography are given by

$$A = C = \frac{1}{\sqrt{2}} - \frac{i}{\sqrt{2}} e^{i\chi} \tag{3.27}$$

$$B = D = \frac{-i}{\sqrt{2}} + \frac{1}{\sqrt{2}} e^{i\chi} \tag{3.28}$$

where χ is proportional to the transverse coordinate across the substrate. It should be noted that in the quantum lithography configuration, the joint detection probability is related to the dose rate at a two-photon absorbing substrate rather than to a traditional coincidence count detection system. Note also that since the two outputs of the beamsplitter are combined on the lithographic plate, the relevant field modes $\hat{a}_{o_1}$ and $\hat{a}_{o_2}$ of the general theory are identical in this case, i.e. $\hat{a}_{o_1} = \hat{a}_{o_2}$. The quantum lithography coefficients, shown in the last column of Table 3.2, are all non-zero and phase dependent. Thus states with different dual- and single-input contributions can have net dose patterns that vary in spatial frequency as well as overall magnitude.

The joint detection probability for the quantum lithography configuration is

given by

$$
\begin{aligned}
\langle \hat{a}_{o_1}^\dagger \hat{a}_{o_2}^\dagger \hat{a}_{o_2} \hat{a}_{o_1} \rangle =\ & (1+\sin^2\chi)[\langle \hat{a}_s^\dagger \hat{a}_s^\dagger \hat{a}_s \hat{a}_s \rangle + \langle \hat{a}_i^\dagger \hat{a}_i^\dagger \hat{a}_i \hat{a}_i \rangle] \\
& +(1-\sin^2\chi)[\langle \hat{a}_s^\dagger \hat{a}_i^\dagger \hat{a}_i \hat{a}_s \rangle + \langle \hat{a}_i^\dagger \hat{a}_s^\dagger \hat{a}_s \hat{a}_i \rangle + 2\langle \hat{a}_s^\dagger \hat{a}_s^\dagger \hat{a}_i \hat{a}_i \rangle + 2\langle \hat{a}_s^\dagger \hat{a}_i^\dagger \hat{a}_s \hat{a}_i \rangle] \\
& +2\ \sin\chi[\langle \hat{a}_s^\dagger \hat{a}_s^\dagger \hat{a}_s \hat{a}_s \rangle - \langle \hat{a}_i^\dagger \hat{a}_i^\dagger \hat{a}_i \hat{a}_i \rangle] \\
& +2\ \cos\chi[\langle \hat{a}_s^\dagger \hat{a}_s^\dagger \hat{a}_i \hat{a}_s \rangle + \langle \hat{a}_s^\dagger \hat{a}_s^\dagger \hat{a}_s \hat{a}_i \rangle + \langle \hat{a}_s^\dagger \hat{a}_i^\dagger \hat{a}_i \hat{a}_i \rangle + \langle \hat{a}_i^\dagger \hat{a}_i^\dagger \hat{a}_s \hat{a}_i \rangle] \\
& +2\ \sin\chi\ \cos\chi[\langle \hat{a}_s^\dagger \hat{a}_s^\dagger \hat{a}_i \hat{a}_s \rangle + \langle \hat{a}_s^\dagger \hat{a}_s^\dagger \hat{a}_s \hat{a}_i \rangle - \langle \hat{a}_s^\dagger \hat{a}_i^\dagger \hat{a}_i \hat{a}_i \rangle - \langle \hat{a}_i^\dagger \hat{a}_i^\dagger \hat{a}_s \hat{a}_i \rangle]
\end{aligned}
$$
$$(3.29)$$

and reduces to $\langle \hat{a}_{o_1}^\dagger \hat{a}_{o_2}^\dagger \hat{a}_{o_2} \hat{a}_{o_1} \rangle = 4(1-\sin^2\chi)$ for a biphoton input, $(1+\sin^2\chi)[2m(m-1)]+(1-\sin^2\chi)[4m^2]$ for a $|mm\rangle$ input, and $(1+\sin^2\chi)[4\overline{m}^2]+(1-\sin^2\chi)[8\overline{m}^2+4\overline{m}]$ for a parametric amplifier input, where the terms proportional to $1+\sin^2\chi$ arise from the single-input paths and the $1-\sin^2\chi$ terms arise from the dual-input paths. Figure 3.7 shows the parametric amplifier joint detection probability, with the relative size of the single-input versus the dual-input contribution plotted as a function of mean photon number. Recalling that the optimum visibility of unity is achieved with a biphoton input which has no single-input contribution, it can be seen that as the single-input contribution increases relative to the dual-input contribution the visibility decreases to its limiting value of $1/5$.

For each of the states generated by parametric downconversion, only terms that oscillate at twice the phase difference are present. The absence of terms oscillating as χ indicate that the patterns produced will have periods smaller than the Rayleigh limit without undesired slower terms. This stands in contrast to the
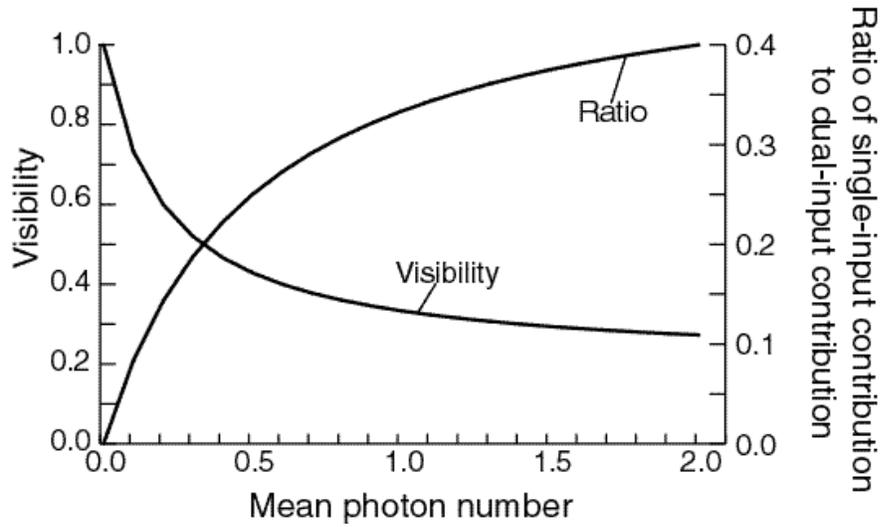
Figure 3.7: Quantum lithography visibility as a function of mean photon number. The visibility decreases as the relative contribution of the single-input terms increases.

probability produced by coherent state inputs$\langle \hat{a}_{o_1}^\dagger \hat{a}_{o_2}^\dagger \hat{a}_{o_2} \hat{a}_{o_1} \rangle = \{2(1 + \sin^2\chi) + 6(1 - \sin^2\chi) + 8\cos\chi\}|\alpha_0|^4$. While the "fast" $\sin^2\chi$ terms are present, the $\cos\chi$ term indicates the presence of undesired slower frequencies.

3.7 Conclusion

In this chapter, the results of calculations determining the effect of increased source gain on the output of three fourth-order interferometric configurations are presented. In these calculations, we have used a model of spontaneous parametric downconversion in which a single signal mode and a single idler mode are coupled. This model allows the gain to be varied in a continuous manner between the low- and high-gain limits. Although the low-gain limit of this model approximates

a $|11\rangle$ state input, the presence of states such as $|22\rangle$ can cause the results to deviate from the biphoton results even at low mean photon numbers. Because of this, interferometer output patterns at high-gain are contrasted with both the low-gain results and the results obtained with a pure $|11\rangle$ state.

A two-photon entangled state used as a source for a Hong-Ou-Mandel interferometer produces no coincidence counts when the arms are matched in pathlength, even though the single detector rates are nonvanishing. The output obtained with a spontaneous parametric downconverter deviated from this result at both low- and high-gain levels. In general, the coincidence rate for the downconverter output is equal to the product of the single detector rates, showing no coincidence count cancellation even with equal arm pathlengths.

In a Mach-Zehnder interferometer, a two-photon entangled state source produces a fourth-order output proportional to $\cos^2 \chi$, where χ is the phase difference between the two arms; this pattern has a visibility of one. When an unseeded parametric amplifier is used, the pattern has the $\cos^2 \chi$ dependence of the entangled state accompanied by an additional background term. The size of the background relative to the phase-dependent component varies with gain level. As the gain is lowered to zero, the visibility approaches one; in the high-gain limit, the visibility decreases to the asymptotic value of $1/3$.

In the third configuration, that of quantum lithography, a two-photon entangled state produces a pattern that varies as $\cos^2 \chi$ where χ is the position-

dependent phase difference between the illuminating beams. This pattern has the desired rapid dependence on χ as well as a visibility of one. An unseeded parametric amplifier produces a pattern that also varies as $\cos^2\chi$ but, as in the Mach-Zehnder case, that is accompanied by a gain-dependent background term. In the low-gain limit, the visibility approaches the two-photon entangled state value of 1. As the gain is increased, the visibility is reduced to a value of 1/5.

The differences among the various results can be understood by decomposing the expression for the joint detection probability of a generalized four-port fourth-order interferometer into state-dependent and interferometer-dependent factors. From this analysis, it can be seen that the loss of visibility arises from the presence of coincidence counts due to photons from a single input arm. These single-input-arm terms are not present in the two-photon entangled state case, where all coincidences are attributable to pathways involving both input arms. Understanding how to alter the relative amounts of each type of contribution by considering a multimode analysis of these fourth-order interferometric systems is thus of interest.

Chapter 4

Multimode Properties of Multi-Pair Fourth-Order Interferometry

4.1 Introduction

In the previous chapter, the transition from two-photon entangled states to input states with multiple pairs was analyzed to see the effect of increased source gain on the output of various fourth-order interferometric systems. In all of the cases analyzed, the introduction of multiple photon pairs via increased gain led to decreases in properties characteristic of the two-photon entangled state. In some cases, desired properties such as coincidence count cancellation vanished entirely; in others, the properties such as sub-Rayleigh spatial features were retained, but with diminished visibility.

These analyses explored the origin of these differences by separating the effect of the different interferometric configurations from the properties of the various

input states considered. This framework allowed the identification of coincidence rate contributions that occur only when multiple photon pairs are present and a comparison of the role of these terms in different systems.

While these analyses outlined important features of the low-gain to high-gain transition, they were restricted to the case where the signal and idler output beams can be approximated as each consisting of a single mode. The analyses thus could not encompass aspects of the photon source such as the distribution of the output across different modes. In practice, these features of the light source are also important determinants of the quantum properties visible in a particular set-up.

In this chapter, we use a multimode treatment to compare the output of fourth-order interferometric systems produced by two-photon and four-photon input states. We again distinguish terms present only with multiple photon pairs from terms present with two-photon states, analyzing the effect that the source mode distribution has on the contribution of each of these terms.

We again find that the presence of these multiple photon pair terms in the high-gain limit leads to significant differences in output from the two-photon case. We find, however, that the mode selection properties of the interferometric system can be used to influence the character of the output produced in the low- and high-gain limits. In some cases, the effect of mode selection can be used to reduce the effect of the multiple photon pair terms, suggesting that for certain systems

the degradative effect of increased gain can be mitigated by the appropriate ma-
nipulation of system properties.

We begin by presenting the model we will use to describe the unseeded para-
metric amplifier. We then use this model to calculate the output produced by
these states in a generalized four-port fourth-order interferometric system. The
differing effect of mode selection on the various terms contributing to two-photon
detection is described. These results are then applied to the Hong-Ou-Mandel
interferometer and quantum lithography configurations. The effects of a nonde-
generate mode distribution across the signal and idler on the multiple pair and
single pair output patterns as well as the interaction of mode selection with the
mode distribution on these output are presented.

4.2   Multimode source states

The output of a parametric downconverter consists of a superposition of states of
the form $|m\rangle_s|m\rangle_i$, where s and i designate the signal and idler modes. This can
be written $|\psi\rangle = \sum_m \rho^{(m)}|m\rangle_s|m\rangle_i$, where the distribution ρ among these states is
dependent on the source gain. At low gain levels, this series is truncated after the
$m = 0$ and $m = 1$ terms; the parametric downconverter can thus be treated as a
two-photon source. As the gain increases, states consisting of multiple pairs such
as $|2\rangle_s|2\rangle_i$ (four-photon) and $|3\rangle_s|3\rangle_i$ (six-photon) become increasingly important,
requiring a model that includes these higher-order components.

In this section, we will begin by describing the multimode parametric amplifier model used to analyze the effects of increased gain on the fourth-order interferometric patterns generated by this type of source. It should be noted that the state produced by a low-gain parametric amplifier is not formally equal to a biphoton state due to the inclusion of higher-order terms. Thus, for reasons of comparison, a multimode treatment of a biphoton state is also included.

4.2.1 Multimode parametric amplifier model

In Chapter 3, the signal and idler outputs of a parametric downconverter were described using the single mode operators $\hat{a}_s$ and $\hat{a}_i$, related to the downconverter input modes $\hat{a}_{s0}$ and $\hat{a}_{i0}$ by relationships of the form

$$\hat{a}_s = U\hat{a}_{s0} + V\hat{a}_{i0}^\dagger \tag{4.1}$$

$$\hat{a}_i = U\hat{a}_{i0} + V\hat{a}_{s0}^\dagger \tag{4.2}$$

where

$$U = \cosh G \tag{4.3}$$

$$V = -i\exp(i\theta)\sinh G. \tag{4.4}$$

The effect of increased gain was observed by increasing either the gain parameter G or the mean single-arm photon number $\overline{m} = |V|^2$.

We now generalize this theory by allowing a distribution of signal and idler modes to be present. We retain the assumption that a given idler mode is coupled to one and only one signal mode, with the frequencies of these modes related by $\omega_s + \omega_i = \omega_0$ where ω_s, ω_i, and ω_0 are the frequencies of the signal, idler, and pump beam respectively.

The relationship between a signal mode at ω and an idler mode at $\omega_0 - \omega$ is now dictated by the frequency-dependent coefficients

$$U(\omega) = \cosh G(\omega) \tag{4.5}$$

$$V(\omega) = -i \exp(i\theta) \sinh G(\omega) \tag{4.6}$$

where

$$\hat{a}_s(\omega) = U(\omega)\hat{a}_{s0}(\omega) + V(\omega)\hat{a}_{i0}^\dagger(\omega_0 - \omega) \tag{4.7}$$

$$\hat{a}_i(\omega_0 - \omega) = U(\omega)\hat{a}_{i0}(\omega_0 - \omega) + V(\omega)\hat{a}_{s0}^\dagger(\omega). \tag{4.8}$$

Note that the gain parameter G is now frequency-dependent, incorporating a factor that is dependent on the specific distribution of gain across frequencies as well as a factor that is dependent on the overall gain level as governed by quantities such as the pump strength. The form of the distribution of frequencies that see gain is dependent on the material and pump parameters.

For field operators of the general form

$$\hat{E}^{(+)}(\mathbf{r}, t) = \int d\omega N(\omega)\hat{a}(\omega)e^{i(\mathbf{k}(\omega)\cdot\mathbf{r}-\omega t)}, \qquad (4.9)$$

the single photon detection probability in the signal arm for an unseeded parametric amplifier can be shown to be given by

$$\langle \hat{E}_s^{(-)}(\mathbf{r}, t)\hat{E}_s^{(+)}(\mathbf{r}, t)\rangle = \int d\omega |N(\omega)|^2 |V(\omega)|^2. \qquad (4.10)$$

The idler single detector probability for the unseeded case is similarly given by

$$\langle \hat{E}_i^{(-)}(\mathbf{r}, t)\hat{E}_i^{(+)}(\mathbf{r}, t)\rangle = \int d\omega |N(\omega)|^2 |V(\omega_0 - \omega)|^2. \qquad (4.11)$$

As in the single-mode model used in Chapter 3, the quantity $|V|^2$ is an indicator of the number of photons created in each arm. In the unseeded case, this number grows from zero.

We can see that if $|V(\omega)|^2$ is centered around a frequency ω_s^0, the signal beam will have a distribution of frequencies centered around ω_s^0; $V(\omega)$ can thus be regarded as a signal frequency distribution function. Furthermore, the corresponding idler beam has a distribution of frequencies governed by $|V(\omega_0 - \omega)|^2$. This distribution will be centered on $\omega_0 - \omega_s^0$. The signal and idler distributions will be degenerate if $\omega_s^0 = \omega_0/2$ and nondegenerate otherwise. If the distributions

are nondegenerate, the signal and idler distributions are centered around different frequencies and thus may be distinguished to some degree by their spectral content.

4.2.2 Two-photon entangled state

In general, the output state containing a single photon pair can be described by [39]

$$|\psi_1\rangle = \int\int d\omega_s d\omega_i \phi(\omega_s, \omega_i)|\omega_s\rangle_s|\omega_i\rangle_i \tag{4.12}$$

where, in the limit of perfect entanglement,

$$\phi(\omega_s, \omega_i) = \phi'(\omega_s)\delta(\omega_0 - \omega_s - \omega_i) \tag{4.13}$$

and, in the limit of no entanglement,

$$\phi(\omega_s, \omega_i) = \phi'(\omega_s)\phi''(\omega_i). \tag{4.14}$$

For states generated by parametric downconversion, the degree of entanglement is dependent on experimental parameters such as the length of the interaction region (determined by the nonlinear crystal length), the beam width at the crystal, and the spectral width of the input beam [28,68,29]. It is possible to have $\omega_s + \omega_i$ take on a range of values, depending on the value of the relevant physical

parameters. In this analysis, as in Section 4.2.1, the relationship $\omega_s + \omega_i = \omega_0$ is assumed.

For a state of the form given in Equation 4.12, the normalization condition $\langle \psi_1 | \psi_1 \rangle = 1$, requires that

$$\int \int d\omega_s d\omega_i |\phi(\omega_s, \omega_i)|^2 = 1 \tag{4.15}$$

Note that the total output state is given by

$$|\psi\rangle = \rho^{(0)} |\text{vac}\rangle_s |\text{vac}\rangle_i + \rho^{(1)} |\psi_1\rangle. \tag{4.16}$$

If

$$|\rho^{(0)}|^2 + |\rho^{(1)}|^2 = 1 \tag{4.17}$$

and

$$\langle \psi_1 | \psi_1 \rangle = 1 \tag{4.18}$$

the output state will be properly normalized.

We can now use these multimode models with a generalized fourth-order interferometer to compare the output produced by an unseeded parametric amplifier operated at both low- and high-gain with the output produced by a two-photon

entangled state. The multimode nature of these models allows us to examine the effect of the interferometer characteristics on the output patterns generated. This generalized description will then be interpreted in the context of the Hong-Ou-Mandel interferometer and quantum lithography configurations.

4.3   Generalized multimode fourth-order interferometer

We assume field operators of the form given in Equation 4.9 and interferometer input-output relationships of the form

$$
\begin{pmatrix} \hat{a}_{o_1}(\omega) \\ \hat{a}_{o_2}(\omega) \end{pmatrix} = \begin{pmatrix} A(\omega) & B(\omega) \\ C(\omega) & D(\omega) \end{pmatrix} \begin{pmatrix} \hat{a}_s(\omega) \\ \hat{a}_i(\omega) \end{pmatrix}
\tag{4.19}
$$

where $\hat{a}_s$ and $\hat{a}_i$ are the input signal and idler modes and $\hat{a}_{o_1}$ and $\hat{a}_{o_2}$ are the output modes. We can note that these are the same input-output relationships used in Chapter 3, with the additional specification of the frequency dependence associated with each operator.

If in addition we assume spectral filters in each arm $f_1(\omega)$ and $f_2(\omega)$, the interferometer output field operators can be written

$$
\hat{E}_1^{(+)}(\mathbf{r},t) = \int d\omega N(\omega) f_1(\omega) \hat{a}_{o_1}(\omega) e^{i(\mathbf{k}(\omega)\cdot\mathbf{r} - \omega t)}
\tag{4.20}
$$

where $\hat{a}_{o_1}(\omega) = A(\omega)\hat{a}_s(\omega) + B(\omega)\hat{a}_i(\omega)$ and

$$\hat{E}_2^{(+)}(\mathbf{r}, t) = \int d^3k N(\omega) f_2(\omega) \hat{a}_{o_2}(\omega) e^{i(\mathbf{k}(\omega) \cdot \mathbf{r} - \omega t)} \tag{4.21}$$

where $\hat{a}_{o_2}(\omega) = C(\omega)\hat{a}_s(\omega) + D(\omega)\hat{a}_i(\omega)$.

As discussed in Section 2.2 the instantaneous two-photon detection probability density is given by the fourth-order correlation function

$$
\begin{aligned}
P(\mathbf{r}_1, t_1; \mathbf{r}_2, t_2) &= \Gamma^{(2,2)}(\mathbf{r}_1, \mathbf{r}_2, \mathbf{r}_2, \mathbf{r}_1; t_1, t_2, t_2, t_1) \tag{4.22} \\
&= \langle \hat{E}^{(-)}(\mathbf{r}_1, t_1) \hat{E}^{(-)}(\mathbf{r}_2, t_2) \hat{E}^{(+)}(\mathbf{r}_2, t_2) \hat{E}^{(+)}(\mathbf{r}_1, t_1) \rangle \tag{4.23}
\end{aligned}
$$

where t_1 and t_2 are the times at which the output photons are detected. The instantaneous probability can be integrated over the coincidence count resolution time T_{cr} to give the coincidence count rate

$$R(\mathbf{r}_1, \mathbf{r}_2; t_1) = \int_{-T_{cr}/2}^{T_{cr}/2} d\tau P(\mathbf{r}_1, t_1; \mathbf{r}_2, t_1 + \tau) \tag{4.24}$$

This can in turn be integrated over the detector resolution time T_d to give the coincidence count probability for a given set of temporal parameters

$$
\begin{aligned}
P_{12}(\mathbf{r}_1, \mathbf{r}_2) &= \int_{-T_d/2}^{T_d} dt R(\mathbf{r}_1, \mathbf{r}_2; t) \tag{4.25} \\
&= \int_{-T_d/2}^{T_d/2} dt_1 \int_{-T_{cr}/2}^{T_{cr}/2} d\tau P(\mathbf{r}_1, t_1; \mathbf{r}_2, t_1 + \tau) \tag{4.26}
\end{aligned}
$$

$$= \int_{-T_d/2}^{T_d/2} dt_1 \int_{-T_{cr}/2}^{T_{cr}/2} d\tau$$

$$\times \quad \langle \hat{E}^{(-)}(\mathbf{r}_1, t_1) \hat{E}^{(-)}(\mathbf{r}_2, t_1 + \tau) \hat{E}^{(+)}(\mathbf{r}_2, t_1 + \tau) \hat{E}^{(+)}(\mathbf{r}_1, t_1) \rangle \quad (4.27)$$

From Equations 4.20, 4.21 and 4.24 we can see that, as in Chapter 3, the coincidence count rate will be dependent on both the interferometer coefficients A, B, C, and D and state-dependent expectation values of the form $\langle \hat{a}^\dagger \hat{a}^\dagger \hat{a} \hat{a} \rangle$. Because these expectation values are assessed in terms of operators at the interferometer input, they can be calculated for the interferometer source independent of the specifics of the interferometer used.

4.3.1 Expectation values at the source output

We can now used the states defined in Section 4.2 to calculate the expectation values at the interferometer input. These values are dependent only on the source characteristics.

Parametric amplifier

The expectation values describing the output of an unseeded parametric amplifier can be calculated using Equations 4.7 and 4.8 together with a source input state of the form $|vac\rangle_s |vac\rangle_i$ where $|vac\rangle$ now represents a multimode vacuum state. As in the single-mode case presented in Chapter 3 terms such as $\langle \hat{a}_s^\dagger \hat{a}_i^\dagger \hat{a}_s \hat{a}_s \rangle$ vanish.

The nonzero terms are:

$$\langle \hat{a}_s^\dagger(\omega''')\hat{a}_s^\dagger(\omega'')\hat{a}_s(\omega')\hat{a}_s(\omega)\rangle =$$

$$V^*(\omega''')V^*(\omega'')V(\omega')V(\omega)[\delta(\omega_0 - \omega'')\delta(\omega_0 - \omega''')$$

$$+\delta(\omega_0 - \omega''')\delta(\omega_0 - \omega'')], \tag{4.28}$$

$$\langle \hat{a}_s^\dagger(\omega''')\hat{a}_i^\dagger(\omega'')\hat{a}_i(\omega')\hat{a}_s(\omega)\rangle =$$

$$V^*(\omega''')U^*(\omega_0 - \omega'')U(\omega_0 - \omega')V(\omega)\delta(\omega_0 - \omega''' - \omega'')\delta(\omega_0 - \omega' - \omega)$$

$$+V^*(\omega''')V^*(\omega_0 - \omega'')V(\omega_0 - \omega')V(\omega)\delta(\omega_0 - \omega''')\delta(\omega_0 - \omega''), \tag{4.29}$$

$$\langle \hat{a}_i^\dagger(\omega''')\hat{a}_s^\dagger(\omega'')\hat{a}_s(\omega')\hat{a}_i(\omega)\rangle =$$

$$V^*(\omega_0 - \omega''')U^*(\omega'')U(\omega')V(\omega_0 - \omega)\delta(\omega_0 - \omega''' - \omega'')\delta(\omega_0 - \omega' - \omega)$$

$$+V^*(\omega_0 - \omega''')V^*(\omega'')V(\omega')V(\omega_0 - \omega)\delta(\omega_0 - \omega''')\delta(\omega_0 - \omega''), \tag{4.30}$$

$$\langle \hat{a}_i^\dagger(\omega''')\hat{a}_i^\dagger(\omega'')\hat{a}_i(\omega')\hat{a}_i(\omega)\rangle =$$

$$V^*(\omega_0 - \omega''')V^*(\omega_0 - \omega'')V(\omega_0 - \omega')V(\omega_0 - \omega)[\delta(\omega_0 - \omega'')\delta(\omega_0 - \omega''')$$

$$+\delta(\omega_0 - \omega''')\delta(\omega_0 - \omega'')], \tag{4.31}$$

$$\langle \hat{a}_s^\dagger(\omega''')\hat{a}_i^\dagger(\omega'')\hat{a}_s(\omega')\hat{a}_i(\omega)\rangle =$$

$$V^*(\omega''')U^*(\omega_0 - \omega'')U(\omega')V(\omega_0 - \omega)\delta(\omega_0 - \omega''' - \omega'')\delta(\omega_0 - \omega' - \omega)$$

$$+V^*(\omega''')V^*(\omega_0 - \omega'')V(\omega')V(\omega_0 - \omega)\delta(\omega_0 - \omega'')\delta(\omega_0 - \omega'''), \quad (4.32)$$

and

$$\langle \hat{a}_i^\dagger(\omega''')\hat{a}_s^\dagger(\omega'')\hat{a}_i(\omega')\hat{a}_s(\omega)\rangle =$$

$$V^*(\omega_0 - \omega''')U^*(\omega'')U(\omega_0 - \omega')V(\omega)\delta(\omega_0 - \omega''' - \omega'')\delta(\omega_0 - \omega' - \omega)$$

$$+V^*(\omega_0 - \omega''')V^*(\omega'')V(\omega_0 - \omega')V(\omega)\delta(\omega_0 - \omega''')\delta(\omega_0 - \omega''). \quad (4.33)$$

Comparison to Table 3.1 shows that these quantities reduce to the previously calculated expectation values in the limit that only one signal and one idler mode, each with frequency $\omega_0/2$, are occupied. It can be noted that in the multimode case, the different terms have different dependences on the various frequencies ω-ω'''. In particular, the arguments of the U and V terms differ in the $\langle \hat{a}_s^\dagger \hat{a}_i^\dagger \hat{a}_i \hat{a}_s \rangle$ and $\langle \hat{a}_i^\dagger \hat{a}_s^\dagger \hat{a}_s \hat{a}_i \rangle$ expressions as compared to the $\langle \hat{a}_s^\dagger \hat{a}_i^\dagger \hat{a}_s \hat{a}_i \rangle$ and $\langle \hat{a}_i^\dagger \hat{a}_s^\dagger \hat{a}_i \hat{a}_s \rangle$ expressions. Recalling that for the Hong-Ou-Mandel interferometer the former pair of expectation values correspond to the paths wherein one signal and one idler photon are either both reflected or both transmitted, and that the latter pair of expectation values correspond to the interference between these paths, we can see that the shape of the gain distribution (i.e. the dependence of U and V on ω) will determine the degree to which path interference leads to a reduction in coincidence counts. This is consistent with the results relating distinguishability and quantum interference [36,52,59] in the two-photon entangled state case.

Two-photon entangled state

Using the general form of the two-photon quantum state (Eq. 4.12), the various two-photon expectation values at the output of the source material can be calculated. Since $\hat{a}_s\hat{a}_s|\psi_1\rangle$ and $\hat{a}_i\hat{a}_i|\psi_1\rangle$ can be shown to vanish, as would be expected for a state with only one photon in the signal and idler modes, all expectation values containing two annihilation operators acting on the same mode will also vanish (e.g. $\langle\hat{a}_s^\dagger\hat{a}_s^\dagger\hat{a}_s\hat{a}_s\rangle = 0$). The remaining two-photon expectation values are given by

$$\langle\hat{a}_s^\dagger(\omega''')\hat{a}_i^\dagger(\omega'')\hat{a}_i(\omega')\hat{a}_s(\omega)\rangle =$$

$$\phi^*(\omega''')\phi(\omega)\delta(\omega_0 - \omega''' - \omega'')\delta(\omega_0 - \omega - \omega'),$$

$$\langle\hat{a}_i^\dagger(\omega''')\hat{a}_s^\dagger(\omega'')\hat{a}_s(\omega')\hat{a}_i(\omega)\rangle =$$

$$\phi^*(\omega_0 - \omega''')\phi(\omega_0 - \omega)\delta(\omega_0 - \omega''' - \omega'')\delta(\omega_0 - \omega - \omega'),$$

$$\langle\hat{a}_s^\dagger(\omega''')\hat{a}_i^\dagger(\omega'')\hat{a}_s(\omega')\hat{a}_i(\omega)\rangle =$$

$$\phi^*(\omega''')\phi(\omega_0 - \omega)\delta(\omega_0 - \omega''' - \omega'')\delta(\omega_0 - \omega - \omega'), \tag{4.34}$$

and

$$\langle\hat{a}_i^\dagger(\omega''')\hat{a}_s^\dagger(\omega'')\hat{a}_i(\omega')\hat{a}_s(\omega)\rangle =$$

$$\phi^*(\omega_0 - \omega''')\phi(\omega)\delta(\omega_0 - \omega''' - \omega'')\delta(\omega_0 - \omega - \omega'). \qquad (4.35)$$

As with the parametric amplifier values, in the single-mode limit these values reduce the previously calculated quantities shown in Table 3.1. As was discussed in the parametric amplifier case, the different frequency dependencies of the path interference terms $\langle \hat{a}_s^\dagger \hat{a}_i^\dagger \hat{a}_s \hat{a}_i \rangle$ and $\langle \hat{a}_i^\dagger \hat{a}_s^\dagger \hat{a}_i \hat{a}_s \rangle$ as compared to the other terms suggest that the degeneracy of the gain parameter as expressed in the U and V coefficients will influence the interferometer output.

4.3.2 Coincidence count rates

The coincidence count rates for the generalized fourth-order interferometer can then be calculated using Equation 4.24, which relates the coincidence count rate and the instantaneous joint detection probability, and Equations 4.20- 4.23, which relate the instantaneous joint detection probability to the interferometer-specific coefficients A, B, C, and D and to the source-determined expectation values calculated in Section 4.3.1.

With these expectation values, the joint detection probability density $\langle \hat{E}_1^{(-)}(\mathbf{r}_1, t_1)\hat{E}_2^{(-)}(\mathbf{r}_2, t_2)\hat{E}_2^{(+)}(\mathbf{r}_2, t_2)\hat{E}_1^{(+)}(\mathbf{r}_1, t_1) \rangle$ can be calculated for the parametric amplifier and two-photon input states. If the interferometer coefficients are independent of frequency, this quantity can be written as the sum of several terms

$$\langle \hat{E}_1^{(-)}(\mathbf{r}_1, t_1)\hat{E}_2^{(-)}(\mathbf{r}_2, t_2)\hat{E}_2^{(+)}(\mathbf{r}_2, t_2)\hat{E}_1^{(+)}(\mathbf{r}_1, t_1) \rangle =$$

$$|C|^2|A|^2 \langle \hat{E}_1^{(-)} \hat{E}_2^{(-)} \hat{E}_2^{(+)} \hat{E}_1^{(+)} \rangle_{ssss}$$

$$+ \quad |D|^2|A|^2 \langle \hat{E}_1^{(-)} \hat{E}_2^{(-)} \hat{E}_2^{(+)} \hat{E}_1^{(+)} \rangle_{siis}$$

$$+ \quad |C|^2|B|^2 \langle \hat{E}_1^{(-)} \hat{E}_2^{(-)} \hat{E}_2^{(+)} \hat{E}_1^{(+)} \rangle_{issi}$$

$$+ \quad |D|^2|B|^2 \langle \hat{E}_1^{(-)} \hat{E}_2^{(-)} \hat{E}_2^{(+)} \hat{E}_1^{(+)} \rangle_{iiii}$$

$$+ \quad 2ReC^*A^*DA \langle \hat{E}_1^{(-)} \hat{E}_2^{(-)} \hat{E}_2^{(+)} \hat{E}_1^{(+)} \rangle_{ssis}$$

$$+ \quad 2ReC^*A^*CB \langle \hat{E}_1^{(-)} \hat{E}_2^{(-)} \hat{E}_2^{(+)} \hat{E}_1^{(+)} \rangle_{sssi}$$

$$+ \quad 2ReC^*A^*DB \langle \hat{E}_1^{(-)} \hat{E}_2^{(-)} \hat{E}_2^{(+)} \hat{E}_1^{(+)} \rangle_{ssii}$$

$$+ \quad 2ReD^*A^*CB \langle \hat{E}_1^{(-)} \hat{E}_2^{(-)} \hat{E}_2^{(+)} \hat{E}_1^{(+)} \rangle_{sisi}$$

$$+ \quad 2ReD^*A^*DB \langle \hat{E}_1^{(-)} \hat{E}_2^{(-)} \hat{E}_2^{(+)} \hat{E}_1^{(+)} \rangle_{siii}$$

$$+ \quad 2ReC^*B^*DB \langle \hat{E}_1^{(-)} \hat{E}_2^{(-)} \hat{E}_2^{(+)} \hat{E}_1^{(+)} \rangle_{isii} \qquad (4.36)$$

where each term $\langle \hat{E}_1^{(-)} \hat{E}_2^{(-)} \hat{E}_2^{(+)} \hat{E}_1^{(+)} \rangle_{jklm}$ is given by

$$\langle \hat{E}_1^{(-)} \hat{E}_2^{(-)} \hat{E}_2^{(+)} \hat{E}_1^{(+)} \rangle_{jklm} =$$

$$\int \int \int \int d\omega''' d\omega'' d\omega' d\omega \, N^*(\omega''')N^*(\omega'')N(\omega')N(\omega)$$

$$\times f_1^*(\omega''') f_2^*(\omega'') f_2(\omega') f_1(\omega) e^{-i(\mathbf{k}'''\cdot\mathbf{r}_1 - \omega''' t_1)} e^{-i(\mathbf{k}''\cdot\mathbf{r}_2 - \omega'' t_2)}$$

$$\times e^{i(\mathbf{k}'\cdot\mathbf{r}_2 - \omega' t_2)} e^{i(\mathbf{k}\cdot\mathbf{r}_1 - \omega t_1)} \langle \hat{a}_j^\dagger(\omega''') \hat{a}_k^\dagger(\omega'') \hat{a}_l(\omega') \hat{a}_m(\omega) \rangle. \qquad (4.37)$$

We can note that Equation 4.36 is analogous to Equation 3.17, which relates the joint detection probability to the interferometer-dependent coefficients and the source-dependent expectation values in the single-mode case. When the interfer-

ometer coefficients are independent of frequency, the effect of the choice of source and of the specific interferometer configuration can be separated term by term into different factors. Since we are interested in understanding the effect of changing source parameters on the interferometer output, this assumption is useful and will be retained.

Parametric amplifier

Insertion of the parametric amplifier expectation values from Section 4.3.1 gives instantaneous joint detection probabilities of the form

$$\langle \hat{E}_1^{(-)} \hat{E}_2^{(-)} \hat{E}_2^{(+)} \hat{E}_1^{(+)} \rangle_{ssss} =$$

$$\int \int d\omega d\omega' \, |N(\omega)|^2 |N(\omega')|^2 f_1^*(\omega') f_2^*(\omega) f_2(\omega') f_1(\omega) e^{-i(\mathbf{k'} \cdot \mathbf{r}_1 - \omega' t_1)}$$

$$\times e^{-i(\mathbf{k} \cdot \mathbf{r}_2 - \omega t_2)} e^{i(\mathbf{k'} \cdot \mathbf{r}_2 - \omega' t_2)} e^{i(\mathbf{k} \cdot \mathbf{r}_1 - \omega t_1)} |V(\omega)|^2 |V(\omega')|^2$$

$$+ \int \int d\omega d\omega' |N(\omega)|^2 |N(\omega')|^2 |f_1(\omega)|^2 |f_2(\omega')|^2 |V(\omega)|^2. \tag{4.38}$$

We can note that in the single-mode limit, the joint detection probability $\langle \hat{E}_1^{(-)} \hat{E}_2^{(-)} \hat{E}_2^{(+)} \hat{E}_1^{(+)} \rangle_{ssss}$ is proportional to $|V|^4$ evaluated at the mode frequency. This is the same dependence on V that was obtained in Chapter 3 for $\langle \hat{a}_s^\dagger \hat{a}_s^\dagger \hat{a}_s \hat{a}_s \rangle$. We can also note that the two terms differ in their time dependence. The second term in Equation 4.38 is independent of the specific values of t_1 and t_2, suggesting that it reflects accidental coincidences unrelated to specific photon pair correla-

tions. The first term in Equation 4.38 contains time-dependent exponentials. This term thus may be expected to relate to coincidences arising from the nature of the parametric amplification process.

Carrying out the time integration in Equation 4.24 gives the total coincidence count rate in terms of the interferometer coefficients and the coincidence rates arising from the integration of the individual joint detection probability terms. In similar fashion to Equation 4.36, this relationship can be expressed as

$$
\begin{aligned}
R_{12} &= |C|^2|A|^2 R_{ssss} + |D|^2|A|^2 R_{siis} + |C|^2|B|^2 R_{issi} + |D|^2|B|^2 R_{iiii} \\
&+ 2Re\left[C^*A^*DAR_{ssis} + C^*A^*CBR_{sssi} + C^*A^*DBR_{ssii}\right. \\
&+ \left.D^*A^*CBR_{sisi} + D^*A^*DBR_{siii} + C^*B^*DBR_{isii}\right]
\end{aligned}
\tag{4.39}
$$

where

$$
R_{jklm} = \int_{-T_{cr}/2}^{T_{cr}/2} d\tau \langle \hat{E}_1^{(-)} \hat{E}_2^{(-)} \hat{E}_2^{(+)} \hat{E}_1^{(+)} \rangle_{jklm}
\tag{4.40}
$$

and $\tau = t_2 - t_1$. Integration over the exponential time-dependent factors gives terms such as $T_{cr}\text{sinc}(\frac{(\omega-\omega')T_{cr}}{2\pi})$. Since the coincidence count resolution time T_{cr} is typically much longer than the inverse of the width of the spectral distribution, the sinc function will vary much more rapidly than the remaining factors within the frequency integrals, allowing us to treat it as a delta function in ω.

The nonzero coincidence count rate contributions for the parametric amplifier

are given by

$$
\begin{aligned}
R_{ssss} &= T_{cr}\left[\int d\omega |N(\omega)|^2 |f_1(\omega)|^2 |V(\omega)|^2\right]\left[\int d\omega |N(\omega)|^2 |f_2(\omega)|^2 |V(\omega)|^2\right] \\
&+ \int d\omega |N(\omega)|^4 |f_1(\omega)|^2 |f_2(\omega)|^2 |V(\omega)|^4,
\end{aligned}
\tag{4.41}
$$

$$
\begin{aligned}
R_{siis} &= T_{cr}\left[\int d\omega |N(\omega)|^2 |f_1(\omega)|^2 |V(\omega)|^2\right]\left[\int d\omega |N(\omega)|^2 |f_2(\omega)|^2 |V(\omega_0 - \omega)|^2\right] \\
&+ \int d\omega |N(\omega)|^2 |N(\omega_0 - \omega)|^2 |f_1(\omega)|^2 |f_2(\omega_0 - \omega)|^2 |U(\omega)|^2 |V(\omega)|^2
\end{aligned}
\tag{4.42}
$$

$$
\begin{aligned}
R_{issi} &= T_{cr}\left[\int d\omega |N(\omega)|^2 |f_1(\omega)|^2 |V(\omega_0 - \omega)|^2\right]\left[\int d\omega |N(\omega)|^2 |f_2(\omega)|^2 |V(\omega)|^2\right] \\
&+ \int d\omega |N(\omega)|^4 |f_1(\omega)|^2 |f_2(\omega_0 - \omega)|^2 |U(\omega_0 - \omega)|^2 |V(\omega_0 - \omega)|^2
\end{aligned}
\tag{4.43}
$$

$$
\begin{aligned}
R_{iiii} &= T_{cr}\left[\int d\omega |N(\omega)|^2 |f_1(\omega)|^2 |V(\omega_0 - \omega)|^2\right]\left[\int d\omega |N(\omega)|^2 |f_2(\omega)|^2 |V(\omega_0 - \omega)|^2\right] \\
&+ \int d\omega |N(\omega)|^4 |f_1(\omega)|^2 |f_2(\omega)|^2 |V(\omega_0 - \omega)|^4
\end{aligned}
\tag{4.44}
$$

and

$$
\begin{aligned}
R_{sisi} &= \int d\omega |N(\omega)|^2 |N(\omega_0 - \omega)|^2 |f_1(\omega)|^2 |f_2(\omega_0 - \omega)|^2 V^*(\omega) U^*(\omega) U(\omega_0 - \omega) V(\omega_0 - \omega) \\
&+ \int d\omega |N(\omega)|^4 |f_1(\omega)|^2 |f_2(\omega)|^2 |V(\omega)|^2 |V(\omega_0 - \omega)|^2.
\end{aligned}
\tag{4.45}
$$

Terms proportional to T_{cr} arise from the time-independent part of the instantaneous joint detection probability (e.g. Equation 4.38 for the *ssss* contribution) and reflect accidental coincidence counts. As such, this contribution to the rate is dependent on the coincidence count resolution time. As this time increases, the rate of accidentals increases. Terms in which T_{cr} is absent reflect contributions to the coincidence count rate that are intrinsic to the parametric amplification process. Because we have assumed that the coincidence count resolution time is much longer than the coherence time of the process, the count rate in this case is independent of the specific value of the resolution time, depending solely on the distribution functions describing the amplification process.

Two-photon entangled state

Insertion of the expectation values from Section 4.3.1 gives instantaneous joint detection probabilities of the form

$$\langle \hat{E}_1^{(-)} \hat{E}_2^{(-)} \hat{E}_2^{(+)} \hat{E}_1^{(+)} \rangle_{siis} =$$

$$\int \int d\omega d\omega'' \, N^*(\omega_0 - \omega'') N^*(\omega'') N(\omega_0 - \omega) N(\omega) f_1^*(\omega_0 - \omega'') f_2^*(\omega'') f_2(\omega_0 - \omega) f_1(\omega)$$

$$\times e^{-i(\mathbf{k}(\omega_0 - \omega'') \cdot \mathbf{r}_1 - (\omega_0 - \omega'') t_1)} e^{-i(\mathbf{k}'' \cdot \mathbf{r}_2 - \omega'' t_2)} e^{i(\mathbf{k}(\omega_0 - \omega) \cdot \mathbf{r}_2 - (\omega_0 - \omega) t_2)} e^{i(\mathbf{k} \cdot \mathbf{r}_1 - \omega t_1)}$$

$$\times \phi^*(\omega_0 - \omega'') \phi(\omega) \tag{4.46}$$

The integration over the resolution time can be carried out as in Section 4.3.2 to give the coincidence count rates

$$R_{siis} = \int d\omega |N(\omega)|^2 |N(\omega_0 - \omega)|^2 |f_1(\omega)|^2 |f_2(\omega_0 - \omega)|^2 |\phi(\omega)|^2 \qquad (4.47)$$

$$R_{issi} = \int d\omega |N(\omega)|^2 |N(\omega_0 - \omega)|^2 |f_1(\omega)|^2 |f_2(\omega_0 - \omega)|^2 |\phi(\omega_0 - \omega)|^2 \quad (4.48)$$

and

$$R_{sisi} = \int d\omega |N(\omega)|^2 |N(\omega_0 - \omega)|^2 |f_1(\omega)|^2 |f_2(\omega_0 - \omega)|^2$$
$$\times \phi^*(\omega)\phi(\omega_0 - \omega). \qquad (4.49)$$

4.4 Hong-Ou-Mandel interferometer results

We will first apply these results to the Hong-Ou-Mandel interferometer. In Chapter 3 we treated the case where there is no pathlength difference across the arms of the interferometer. However, we can recall from the two-photon entangled state results reviewed in Chapter 2 that when the multimode nature of the signal and idler parametric downconverter outputs are taken into account, the resulting coincidence count rate is dependent on the pathlength difference between arms [51]. When the arms are matched in length, the coincidence count rate falls to its minimum. When the pathlength difference increases, the rate increases to

an asymptotic level, with the rapidity of the increase determined by the size of pathlength-induced time delay relative to the inverse of the output distribution bandwidth. We will retrieve this result from the expressions derived in Section 4.3 for the two-photon entangled state case, then extend this analysis to a parametric amplifier source.

The relationship between the input and output modes of a Hong-Ou-Mandel interferometer can be described by the coefficients

$$A(\omega) = D^*(\omega) = \frac{1}{\sqrt{2}} e^{\frac{i\omega\tau}{2}} \tag{4.50}$$

$$B(\omega) = -C^*(\omega) = \frac{-i}{\sqrt{2}} e^{\frac{-i\omega\tau}{2}}. \tag{4.51}$$

where τ is the time delay caused by the pathlength difference between the interferometer arms [39]. Because these coefficients are now dependent on the mode frequency ω, the individual $\langle \hat{E}_1^{(-)} \hat{E}_2^{(-)} \hat{E}_2^{(+)} \hat{E}_1^{(+)} \rangle_{jklm}$ terms in the expression for the joint detection probability density (Equation 4.36) may now contain the interferometer coefficients within the frequency integrals; individual expectation values that were previously dependent solely on the source characteristics can now be dependent on the interferometer parameters as well. Because, for the states under consideration, most of the terms affected by this change vanish, the only term actually affected by this change is the $\langle \hat{E}_1^{(-)} \hat{E}_2^{(-)} \hat{E}_2^{(+)} \hat{E}_1^{(+)} \rangle_{sisi}$ term.

4.4.1 Two-photon entangled state

The coincidence count rate R_{12} for the two-photon entangled state can be obtained by evaluating Equations 4.47-4.49 for a specific spectral distribution. Equation 4.49, which is the term associated with interference between path amplitudes, is now modified by pathlength-associated exponential factors to the expression

$$R_{sisi} = \int d\omega |N(\omega)|^2 |N(\omega_0 - \omega)|^2 |f_1(\omega)|^2 |f_2(\omega_0 - \omega)|^2 e^{\frac{i(\omega_0 - 2\omega)\tau}{2}}$$

$$\times \phi^*(\omega)\phi(\omega_0 - \omega). \tag{4.52}$$

Using a Gaussian signal distribution for $\phi(\omega)$ [28], the coincidence count rate is found to be

$$R_{12} = \frac{1}{4} \left\{ 1 - e^{-\left(\frac{\omega_s^0 - \omega_i^0}{2\Delta\omega}\right)^2} e^{-\left(\frac{\Delta\omega\tau}{2}\right)^2} \right\} \tag{4.53}$$

where ω_s^0 is the center of the signal distribution, $\omega_i^0 = \omega_0 - \omega_s^0$ is the center of the idler distribution, and $2\Delta\omega$ is the width of the distributions. Note that we have not included the effect of filters f_1 and f_2, and we have assumed that the normalization varies slowly with ω, removing it from the integrals. We can see that, as expected, the coincidence count rate for the Hong-Ou-Mandel interferometer is dependent on the pathlength difference between arms, decreasing with increasing pathlength, and on the degree of asymmetry between the signal and idler spectral distributions. If the distributions are degenerate ($\omega_s^0 = \omega_i^0 = \omega_0/2$), then the count rate reaches

a minimum of zero. If the distributions are nondegenerate, then the count rate minimum becomes shallower, with the count rate at some nonzero value even for equal pathlengths. This lack of complete coincidence count cancellation can be attributed to the loss of indistinguishability between the signal and idler outputs of the downconversion [52,59,53].

4.4.2 Parametric amplifier

We can now extend these results to the case where the input to the interferometer is an unseeded parametric amplifier described by Equations 4.7 and 4.8. As in Section 4.4.1, we will ignore the filter functions and normalization constants, focusing on the role of the distribution functions $V(\omega)$ and $U(\omega)$. It is convenient to rewrite the equations for the various contributions to the coincidence rate (Equations 4.41- 4.45) in terms of the single detector joint detection probability densities

$$J_s = \langle \hat{E}_s^{(-)}(\mathbf{r},t)\hat{E}_s^{(+)}(\mathbf{r},t)\rangle = \int d\omega |V(\omega)|^2 \tag{4.54}$$

and

$$J_i = \langle \hat{E}_s^{(-)}(\mathbf{r},t)\hat{E}_s^{(+)}(\mathbf{r},t)\rangle = \int d\omega |V(\omega_0 - \omega)|^2 \tag{4.55}$$

giving

$$
\begin{aligned}
R_{12} \;=\; \frac{1}{4} \Bigg\{ & \int d\omega |V(\omega)|^4 + T_{cr} J_s^2 \\
& + \int d\omega |U(\omega)|^2 |V(\omega)|^2 + T_{cr} J_s J_i \\
& + \int d\omega |U(\omega_0 - \omega)|^2 |V(\omega_0 - \omega)|^2 + T_{cr} J_i J_s \\
& + \int d\omega |V(\omega_0 - \omega)|^4 + T_{cr} J_i^2 \\
& - 2\mathrm{Re} \Bigg[\int d\omega V^*(\omega) U^*(\omega) U(\omega_0 - \omega) V(\omega_0 - \omega) e^{i(\omega_0 - 2\omega)\tau} \\
& + \int d\omega |V(\omega)|^2 |V(\omega_0 - \omega)|^2 \Bigg] \Bigg\}
\end{aligned}
\tag{4.56}
$$

We can note that the last term, which is attributable to the interference between possible paths, is the only term dependent on the pathlength difference between arms. This parallels the two-photon entangled state results in this configuration. We can also note the presence of terms proportional to the product of single detector joint detection probability densities. These can be viewed as the rate contribution arising from accidental coincidences. As such, these contributions will increase as the window allowed for coincidences increases.

Relating these results back to the results of Chapter 3, we can consider the case of degenerate signal and idler distributions with zero pathlength difference between arms. In this case, the functions $|U(\omega)|$ and $|V(\omega)|$ will be invariant under a change of arguments from ω to $\omega_0 - \omega$, and the coincidence count rate further reduces to $R_{12} = T_{cr} J_s^2$. (Figure 4.1) Noting that J_s is proportional to the number
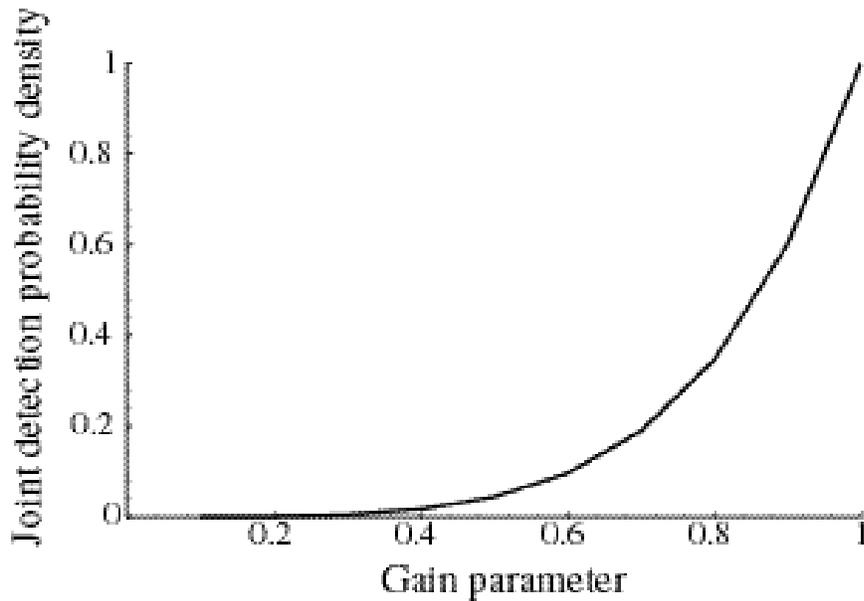
Figure 4.1: Hong-Ou-Mandel interferometer joint detection probability as a function of the source gain parameter G. The displayed values have been normalized to the joint detection probability at G = 1. The joint detection probability is equal to the square of the single detector probability J_s.

of single detector counts in the signal (or idler) arm, we can see that this expression parallels that obtained in the single-mode case (Equation 3.12), where the joint detection probability was found to be equal to the mean number of photons in one of the amplifier output arms. Comparison to the two-photon entangled state results shows that in this interferometer, the presence of additional photon pairs arising from increased parametric amplifier gain leads to qualitatively different results in the two cases.

4.5 Quantum lithography results

We can next apply this model to quantum lithography, extending the results of Section 3.6 to the multimode case. The relationship between the input and output modes in the quantum lithography configuration is describable by the coefficients

$$A = C = \frac{1}{\sqrt{2}}(1 - ie^{i\chi}) \tag{4.57}$$

$$B = D = \frac{1}{\sqrt{2}}(-i + e^{i\chi}) \tag{4.58}$$

where χ is proportional to the transverse coordinate across the observation plane. We can recall that terms in the output pattern that vary as χ have a minimum spacing of $\lambda/2$, while terms that vary as 2χ (e.g. $\cos^2 \chi$) will have a minimum spacing of $\lambda/4$. We will assume that no spectral filters are used, thus all filter functions are replaced by 1 as in the previous sections. Note that we are treating the phase difference as frequency independent. The features of primary interest are the presence of components rapidly varying with χ (i.e. varying as 2χ), the absence of components slowly varying with χ (i.e. varying as χ), and the overall pattern visibility.

4.5.1 Two-photon entangled state

When the quantum lithography coefficients are used in conjunction with the expressions for the individual two-photon entangled state coincidence rate contribu-

tions (Equations 4.47-4.49), we obtain

$$R_{12} = [\cos^2 \chi] \int d\omega \left\{ |\psi(\omega)|^2 + |\psi(\omega_0 - \omega)|^2 + 2\mathrm{Re}\psi^*(\omega)\psi(\omega_0 - \omega) \right\}. \quad (4.59)$$

For degenerate parametric downconversion $\psi(\omega) = \psi(\omega_0 - \omega)$ and the coincidence count rate reduces to $4\cos^2 \chi$. A comparison of the two-photon quantum lithography probability with the two-photon Hong-Ou-Mandel probability (Eq. 4.53) shows that there is a different relationship between coincidence count terms in the two cases. In the Hong-Ou-Mandel case, if the signal and idler are indistinguishable, the negative sign in the expression for the coincidence count probability causes the net probability to go to zero; as the spectral distinguishability increases, the interference pattern becomes shallower, ultimately vanishing. In the quantum lithography arrangement, this phase relationship among components is not present. There is a $\cos^2 \chi$ dependence regardless of spectral distinguishability. We can see that the use of a two-photon entangled state source produces a pattern with the three desired characteristics of rapid dependence on χ, absence of a $\cos \chi$ component, and unit visibility.

4.5.2 Parametric amplifier

With a parametric amplifier input, the output pattern produced in the quantum lithography configuration is less robust to changes in source parameters. In specific, we will see that the presence of single-input terms such as R_{ssss} that are not

present in the two-photon case leads to a reduction in visibility. Because these terms are increasingly present as gain is increased, the output pattern visibility is sensitive to the gain level. In addition, the presence of accidental coincidences, which are also absent in the two-photon case, leads to degradation of the visibility.

Comparison of the general expressions for the terms contributing to the coincidence count rate in the parametric amplifier (Eqs. 4.41- 4.45) and two-photon entangled state cases (Eqs. 4.47- 4.49) shows that the R_{ssss} and R_{iiii} terms that vanish in the latter case are significant when a parametric amplifier is used as a source. As discussed in Section 3.4, these terms can be attributed to the case where two photons from a single input arm are detected together. The R_{ssss} can be identified with the contribution originating entirely from the signal arm and R_{iiii} with the contribution originating entirely from the idler arm. These single-input terms can be seen to have different functional dependences on the amplifier coefficients U and V than the dual-input R_{siis}, R_{issi}, and R_{sisi} terms. The single-input terms are entirely dependent on $V(\omega)$ while the dual-input terms are dependent on integrands that vary with both $|V|^4$ and $|U|^2|V|^2$. Noting that $|V|$ is smaller than $|U|$ at low values of the gain parameter G, we might expect that the dual-input terms will be dominant at the low-gain limit; this can be seen to be true in Figure 4.2, plotted for the degenerate case. As the gain increases, the $|U|^2|V|^2$ and $|V|^4$ terms are seen to approach each other in size, implying that the dual- and single-input terms make similar contributions at the high-gain limit.
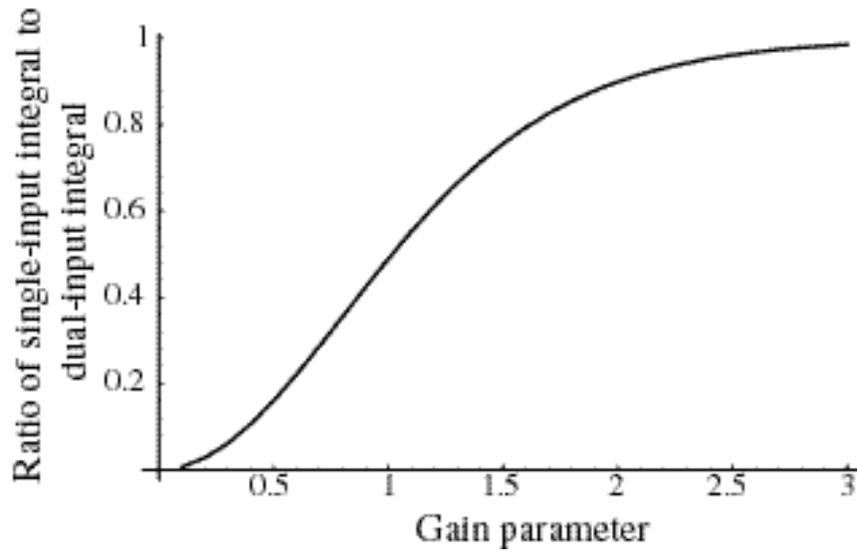
Figure 4.2: Ratio between single-input (R_{ssss}) and dual input (R_{siis}) contributions to the coincidence count rate. This ratio does not include terms arising from accidental coincidences. The R_{ssss} term is attributable to counts where both photons arise from the signal arm. It is not significant at very low gain levels. The integrand of this term is proportional to $|V(\omega)|^4$. The R_{siis} term is attributable to counts where one photon is contributed by each input arm. The integrand of this term is proportional to $|U(\omega)|^2|V(\omega)|^2$. $|V(\omega)|^4$.

We can see the influence of each of these terms in the expression for the quantum lithography coincidence count rate

$$
\begin{aligned}
R_{12} &= (1 + \sin\chi)^2 \left\{ \int d\omega |V(\omega)|^4 + T_{cr} J_s^2 \right\} \\
&\quad + (1 - \sin^2\chi) \left\{ \int d\omega |U(\omega)|^2 |V(\omega)|^2 + T_{cr} J_s J_i \right\} \\
&\quad + (1 - \sin^2\chi) \left\{ \int d\omega |U(\omega_0 - \omega)|^2 |V(\omega_0 - \omega)|^2 + T_{cr} J_i J_s \right\} \\
&\quad + (1 - \sin\chi)^2 \left\{ \int d\omega |V(\omega_0 - \omega)|^4 + T_{cr} J_i^2 \right\} \\
&\quad + 2(1 - \sin^2\chi) \mathrm{Re} \left[\int d\omega V^*(\omega) U^*(\omega) U(\omega_0 - \omega) V(\omega_0 - \omega) \right. \\
&\quad \left. + \int d\omega |V(\omega)|^2 |V(\omega_0 - \omega)|^2 \right].
\end{aligned}
\tag{4.60}
$$

The single-input contributions, which lead to the $(1 + \sin\chi)^2$ and $(1 - \sin\chi)^2$ terms in this expression, are dependent solely on $|V|$ and will contribute to a pattern that goes as $1 + \sin^2\chi$. The dual-input terms vary as $1 - \sin^2\chi$ and are dependent on both $|U|$ and $|V|$. Because the dual- and single-input terms each contain a $\sin^2\chi$ component, the desired rapid dependence on χ will be present. However, because these two contributions are out of phase with one another, as the gain increases the balance between these two components will shift, leading to changes in the output pattern (Figure 4.3).

For the degenerate case shown in this figure, the equalities

$$
J_{V^4} = \int d\omega |V(\omega)|^4
\tag{4.61}
$$
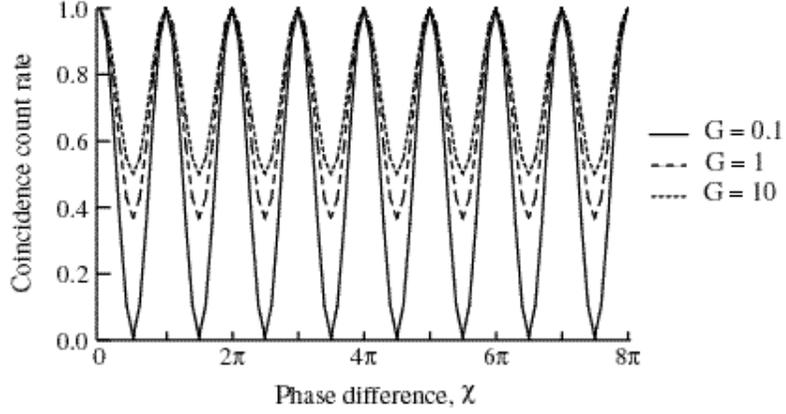
Figure 4.3: Quantum lithography coincidence count rate as a function of phase difference at various values of the gain parameter G. The count rates have been normalized to peak values of 1 to allow for comparison between the various curves. The contribution from accidental coincidences has been subtracted from these curves. A significant decrease in visibility with increasing gain can be noted.

$$= \int d\omega |V(\omega_0 - \omega)|^4 \tag{4.62}$$

$$= \int d\omega |V(\omega)|^2 |V(\omega_0 - \omega)|^2, \tag{4.63}$$

$$J_{U^2 V^2} = \int d\omega |U(\omega)|^2 |V(\omega)|^2 \tag{4.64}$$

$$= \int d\omega |U(\omega_0 - \omega)|^2 |V(\omega_0 - \omega)|^2 \tag{4.65}$$

$$= \int d\omega V^*(\omega) U^*(\omega) U(\omega_0 - \omega) V(\omega_0 - \omega), \tag{4.66}$$

and

$$J_s = \int d\omega |V(\omega)|^2 \tag{4.67}$$

$$= \int d\omega |V(\omega_0 - \omega)|^2 \tag{4.68}$$

$$= J_i \qquad (4.69)$$

can be used to simplify the expressions for the output pattern

$$R_{12} = 4\{J_{V^4} + T_{cr}J_s^2 + J_{U^2V^2}\cos^2\chi\} \qquad (4.70)$$

and the visibility

$$\text{Vis} = \frac{J_{U^2V^2}}{2J_{V^4} + J_{U^2V^2} + 2T_{cr}J_s^2}. \qquad (4.71)$$

The variation of this visibility with the gain parameter G is displayed in Figure 4.4 for the case where the accidental counts from the terms proportional to T_{cr} have been removed. We can see that even in the case where the accidental counts are assumed to be removable, the visibility decreases with increasing gain. In the asymptotic limit, the visibility reaches $1/3$. This value is higher than the $1/5$ value obtained in the single-mode case because the accidental counts that are present with both models have been removed.

In the case where a coincidence counter is used to measure this fourth-order pattern, the estimation and removal of the counts proportional to the coincidence window is feasible. However, in the case where the joint detection is performed by a two-photon absorbing substrate, the ability to compensate for the acciden- tal coincidence rate cannot be assumed. Inspection of the visibility expression
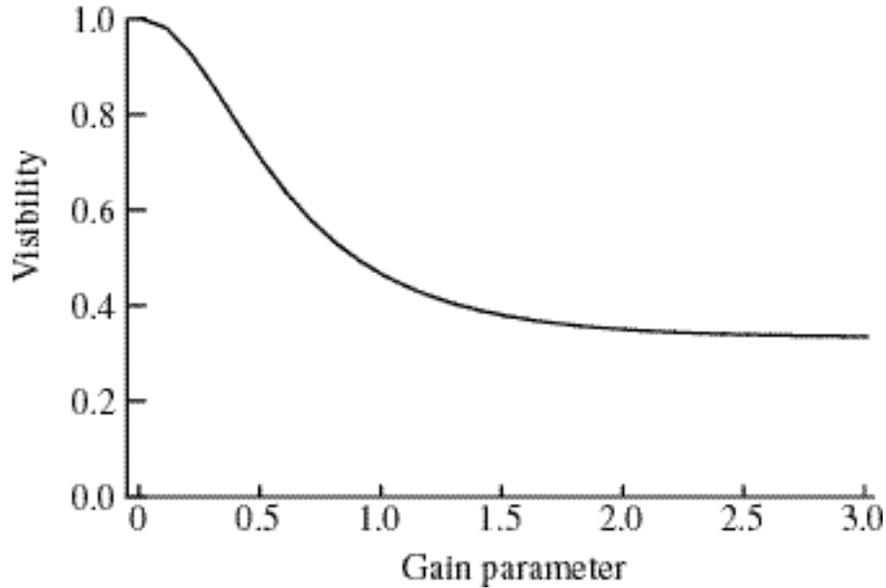
Figure 4.4: Quantum lithography pattern visibility as a function of the gain parameter G. The contribution from accidental coincidences is not included. The asymptotic value of the visibility is 1/3.

(Eq. 4.71) shows that as the coincidence count window is increased the visibility will be lowered. This can be seen in Figure 4.5, which displays the patterns obtained when the accidental coincidences are removed (equivalent to setting T_{cr} to zero) and when the accidental rate is assumed nonzero.

4.6   Effect of mode selection on visibility

One issue yet to be addressed in this chapter is the effect of filtering on the output patterns generated by these interferometric arrangements. We can return to the general expressions for the various coincidence count contributions for the parametric amplifier (Eqns. 4.41- 4.45), this time focusing on the functional
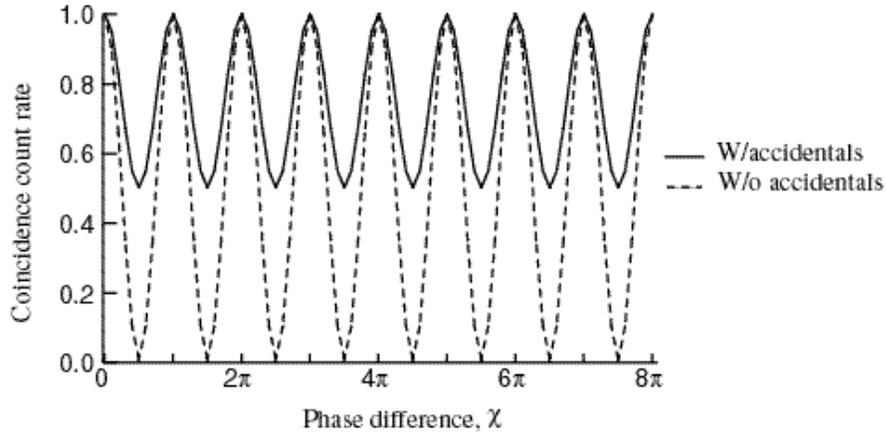
Figure 4.5: Quantum lithography output patterns as a function of the phase difference with and without the inclusion of accidental coincidences. The contribution of these coincidences was included by using a value for the coincidence count resolution time that produced an accidental rate equal to the dual-input rate. As might be expected, accidental coincidences degrade visibility.

dependence of these terms on the filter functions f_1 and f_2. We will term the situation where the filters in each arm have the same central frequency the symmetric filter case and situations where the filters have different central values as the asymmetric case.

Given a degenerate spectral distribution and symmetric filters, the filters simply act in conjunction with the distribution to determine the observed distribution width. However, asymmetries in the spectral distribution and filter settings can affect the various contributions differently, shifting the balance between the components of the coincidence count rate and affecting the observed interferometer output.

The influence of spectral asymmetry has been well analyzed in the case of two-photon entangled states [36,52,59,54]. If the signal and idler distributions (in our

notation, represented by $\phi(\omega)$ and $\phi(\omega_0 - \omega)$ respectively), are centered around different frequencies, the contribution of the term attributable to interference between paths (R_{sisi}) decreases, thus reducing the amount of coincidence count cancellation observed.

This result would seem to suggest that spectral asymmetry could lead to deleterious effects in the quantum lithography configuration as well. However, inspection of the dependence of the various terms in the coincidence count rate on the phase difference χ

$$
\begin{aligned}
R_{12} &= (1 + \sin\chi)^2 R_{ssss} + (1 - \sin^2\chi)\left\{R_{siis} + R_{issi}\right\} + (1 - \sin\chi)^2 R_{iiii} \\
&\quad + 2(1 - \sin^2\chi)\mathrm{Re}R_{sisi}
\end{aligned} \tag{4.72}
$$

shows that if terms contributing to the $(1 - \sin^2\chi)$ variation are strongly favored at the expense of terms contributing to a $(1 + \sin^2\chi)$ variation, or vice versa, the visibility will improve. On the other hand, if the two types of terms are made more equal, they will cancel each other out, leading to little variation with χ.

Comparison of the single detector rates when filters are included shows that there are four types of integrals present, that vary in filter and distribution. These can be written as

$$
J_{1s} = \int d\omega |f_1(\omega)|^2 |V(\omega)|^2 \tag{4.73}
$$

$$J_{1i} = \int d\omega |f_1(\omega)|^2 |V(\omega_0 - \omega)|^2 \tag{4.74}$$

$$J_{2s} = \int d\omega |f_2(\omega)|^2 |V(\omega)|^2 \tag{4.75}$$

$$J_{2i} = \int d\omega |f_2(\omega)|^2 |V(\omega_0 - \omega)|^2 \tag{4.76}$$

and correspond to the joint detection probability densities obtained when the signal or idler beams are directed into detectors 1 or 2. If the distribution $V(\omega)$ is centered around a frequency ω_s^0 that is not equal to $\omega_0/2$, the idler distribution $V(\omega_0 - \omega)$ will be centered around a frequency ω_i^0 that is not equal to ω_s^0. If f_1 is centered around ω_s^0 and f_2 is centered around ω_i^0, J_{1s} and J_{2i} will be favored. Terms such as $\int d\omega |f_1(\omega)|^2 |f_2(\omega)|^2 |V(\omega)|^4$ in R_{ssss} and $\int d\omega |f_1(\omega)|^2 |f_2(\omega_0 - \omega)|^2 |U(\omega)|^2 |V(\omega)|^2$ in R_{siis} (Eqns. 4.41- 4.45) will also be affected, with the R_{ssss} integral diminished while R_{siis} is favored. As discussed above, this type of differential effect will lead to a diminishment of the desired effect in the Hong-Ou-Mandel interferometer configuration, but could lead to increased visibility in the quantum lithography configuration. These results suggest that filter selection in conjunction with an nondegenerate spectrum can shift the balance among various coincidence count rate contributions, altering the output pattern either favorably or unfavorably.

4.7 Conclusion

In this chapter we generalized the parametric amplifier model used in Chapter 3 to the case where multiple signal and idler modes may be occupied. This multimode model was then used to reanalyze the Hong-Ou-Mandel interferometer and quantum lithography configurations. Throughout this chapter, the output produced with two-photon entangled state input was used as a basis for comparison.

The feature of interest in the Hong-Ou-Mandel interferometer configuration was the coincidence count reduction that occurs when the time delay between the two interferometer arms is less than the inverse of the spectral distribution bandwidth. We found that the expression for the coincidence count rate produced by an unseeded parametric amplifier contained terms that could contribute to coincidence count reduction as well as background terms that are not present in the two-photon case. The background terms are proportional to products of single detector probabilities, suggesting that they can be attributed to accidental coincidences. These terms lead to a loss of contrast in the generated pattern, as the minimum coincidence rate increases with increasing gain. In the degenerate case, with equal pathlengths, the parametric amplifier result echoes the single-mode result presented in Chapter 3; the coincidence rate is proportional to the product of the single detector probabilities.

In the quantum lithography configuration, two-photon entangled state input produces a pattern with a minimum spacing of $\lambda/4$ and a visibility of one. Multi-

mode parametric amplifier input was found to retain the desirable $\lambda/4$ variation. However, the visibility was strongly influenced by the presence of both background terms and terms arising from the coincident detection of two photons from the same input arm. Both of these types of contributions are absent in the two-photon case. The visibility was strongly dependent on gain level, vanishing in the high-gain limit.

Although the results in both cases indicate a diminishment or disappearance of the desired output pattern property in the high-gain limit, the multimode treatment also makes explicit the possibility of adjusting the balance between various terms to alter the total interferometer output. In the Hong-Ou-Mandel interferometer case, spectral asymmetry leads to a decrease in pattern visibility. In the quantum lithography case, however, the differing relationships among coincidence rate components suggests the possibility of altering the relative sizes of terms in a way that leads to increased rather than decreased pattern visibility.

Chapter 5

Vacuum-Initiated Filamentation as a Source of Entangled States

5.1 Introduction

It has often been observed that as a laser beam is passed through a nonlinear medium it breaks up into a large number of filaments. This filamentation process is initiated by the presence of weak perturbations on the laser wavefront, [69,70] which can grow by means of four-wave mixing processes [71] and become large enough to disturb the overall propagation of the beam. The questions addressed in this chapter are whether vacuum fluctuations, which are intrinsic to the beam, can act as perturbations to initiate filamentation and whether the generated beams can serve as sources of single- and multiple-pair entangled states.

We begin with a discussion of filamentation as a four-wave mixing process. The initiation of this process by vacuum fluctuations is then discussed [72]. We show that vacuum fluctuations of the electromagnetic field constitute a fundamental

perturbation to the incident laser field, and that filamentation initiated by these quantum fluctuations places a realistic upper limit on the laser intensity that can be transmitted through a given nonlinear optical material without the occurrence of beam breakup.

The quantum properties of the states produced by filamentation are then analyzed and the suitability of filamentation as a source for fourth-order interferometry is discussed.

5.2 Filamentation as a four-wave mixing process

Self-focusing can be considered from the perspective of the nonlinear index of refraction. Viewing the nonlinearity as a change in the refractive index leads naturally to a treatment of self-focusing as a lens-like effect and is entirely appropriate for discussions of whole-beam self-focusing. However, another segment of research in this area concerns multimode effects, where the input beam is observed to break up into multiple beams. In this case, an analysis of self-focusing in terms of the growth of perturbations on the input beam has more utility and leads to a view of filamentation as a four-wave mixing process.

Early experiments in self-focusing found that beams could evolve into both single and multiple filaments [73]. For example, in 1966 Townes and co-workers published experimental observations of a Q-switched beam collapsing into a single filament with a diameter as small as 50 microns [74] and also demonstrated
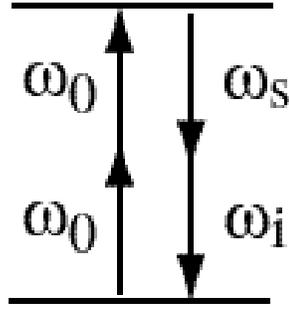
Figure 5.1: Four-wave mixing amplifies weak waves (ω_s,ω_i) at the expense of the pump wave (ω_0).

the collapse of a single beam into many small (few micron) filaments. [75] Chiao, Kelley and Garmire [71] gave a physical explanation of the growth of the off-axis modes in terms of stimulated light scattering. They showed that the nonlinear index of refraction allows the coupling of a strong incident wave with weak waves having different transverse wavevectors. The four-photon interaction of a photon with wavevector $\mathbf{k}_1 = \mathbf{k}_0 + \mathbf{q}$, a photon at $\mathbf{k}_2 = \mathbf{k}_0 - \mathbf{q}$ and two pump photons with $\mathbf{k} = \mathbf{k}_0$ can allow the two weak waves to see gain (Figure 5.1). This gain is dependent on the fulfillment of a phase-matching relation involving the participating waves. (Fig. 5.2) Because of this condition, certain transverse wavevectors will see more gain than others and will come to dominate the spatial evolution of the total field.

The magnitude of the wavevector that will see the maximum gain was calculated using phase matching considerations. From Figure 5.2 we can see that the z-component of $\mathbf{k}_1$ should equal $\mathbf{k}_0$ for optimum phase matching. This gives the relationship $\sqrt{k_1^2 - q^2} = k_0$. We can then substitute in k_1 and k_0 taking into ac-

$$\mathbf{k}_1 = \mathbf{k}_0 + \mathbf{q} \qquad\qquad \mathbf{k}_2 = \mathbf{k}_0 - \mathbf{q}$$

$$\mathbf{q}$$

$$\mathbf{k}_0 \qquad\qquad \mathbf{k}_0$$
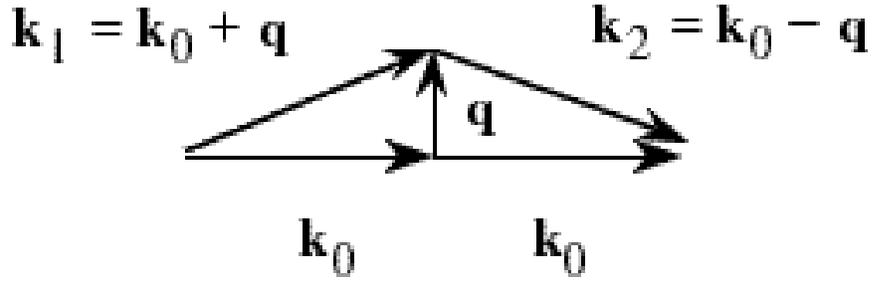
Figure 5.2: Self-focusing as a form of forward four-wave mixing.

count the weak-wave retardation of k_1. This gives the magnitude of the dominant transverse wavevector to be

$$q = \sqrt{k_1^2 - k_0^2} \tag{5.1}$$

$$= \frac{\omega}{c}\sqrt{(n_0 + 2n_2 I)^2 - (n_0 + n_2 I)^2} \tag{5.2}$$

$$= \frac{\omega}{c}\sqrt{2n_0 n_2 I + 3n_2^2 I^2} \tag{5.3}$$

This can be approximated to first order in n_2 to be $q = k_0\sqrt{2n_2 I/n_0}$. This picture is consistent with the model of Bespalov and Talanov [76], which predicted the existence of a dominant instability size $\Lambda = (\pi/k)\sqrt{n_0/2n_2 I}$. It emphasizes the ability of the self-focusing process to allow small perturbations to have a large effect on the overall beam evolution.

Experimental confirmation of this effect, by Carman, et al. [77] and others [69] followed. Among the characteristic signatures of this process are the growth of perturbations at a rate dependent on the spatial frequency of the perturbations and conical emission in the far-field.

5.3 Filamentation initiation by quantum fluctuations

Our theoretical formalism follows closely that of Bespalov and Talanov, [76] which treats the filamentation process classically by considering the gain seen by a wavefront perturbation on a strong, monochromatic pump beam propagating through a Kerr material. Our treatment differs from theirs in that we consider the optical field to be a quantum mechanical quantity. The quantum fluctuations of such a field (i.e., vacuum fluctuations) are necessarily spectrally broad band. Our model thus predicts that quantum-initiated filamentation differs from its classical counterpart in that it is accompanied by a spectral broadening of the transmitted laser field. Our model also differs from its classical counterpart in that it leads to explicit predictions regarding the strength of the fluctuations that initiate the filamentation process.

Consider the propagation of a laser beam through a Kerr material. We can express the positive frequency part of the total field as

$$\hat{E}^{(+)}(\mathbf{r}, t) = \left[\mathcal{E}_0 + \hat{\mathcal{E}}_1(\mathbf{r}, t) \right] e^{i\gamma_0 z} e^{i(k_0 z - \omega t)}. \tag{5.4}$$

Here $\mathcal{E}_0$ denotes the amplitude of the strong pump field, which we have treated classically, and which we assume to have frequency ω_0 and wavevector $k_0 + \gamma_0$, where $k_0 = n_0 \omega_0 / c$ is its linear contribution and $\gamma_0 = n_2 I_0 \omega_0 / c$ is its nonlinear

contribution, with $n_2 = (12\pi^2/n_0^2 c)\chi^{(3)}$ and $I_0 = (n_0 c/2\pi)|\mathcal{E}_0|^2$. The perturbation, which we are treating as a quantum mechanical operator, is denoted $\hat{\mathcal{E}}_1$ and is conveniently decomposed in terms of its frequency components ω and transverse wavevector components $\mathbf{q}$ as

$$\hat{\mathcal{E}}_1(\mathbf{r}, t) = \int d^2 q \int_0^\infty d\omega N(\omega)\hat{a}(\mathbf{q}, \omega; z)e^{i(\mathbf{q} \cdot \mathbf{r})}e^{i(k_z(\omega) - k_0)z - i(\omega - \omega_0)t}. \tag{5.5}$$

The mode amplitudes are denoted by $\hat{a}(\mathbf{q}, \omega; z)$ and satisfy the usual commutation relation $\left[\hat{a}(\mathbf{q}, \omega; z), \hat{a}^\dagger(\mathbf{q}', \omega'; z)\right] = \delta^2(\mathbf{q} - \mathbf{q}')\delta(\omega - \omega')$. We have also introduced the mode normalization factor $N(\omega) = \sqrt{\hbar\omega^2 n^2(\omega)/4\pi^2 k_z(\omega)c^2}$. Note that we are assuming that the nonlinear response can be modeled adequately by a dispersionless third-order susceptibility. We are thus ignoring effects such as those of population trapping, which under certain conditions can prevent the occurrence of self focusing. [78] We assume that n_0 is frequency independent; the validity of this assumption is discussed below. We further assume that $n_2 I_0 \ll n_0$. Note that we have taken the input pump beam to be a perfect plane wave. We have done so to make clear that the onset of filamentation stems from the presence of vacuum fluctuations and not from other perturbations to the input profile. While the introduction of a finite beam width would bring new transverse components into play, the evolution of these components leads simply to diffraction and to whole beam self-focusing and does not alter these conclusions in any significant way.

We insert the field $\hat{E}^{(+)}(\mathbf{r}, t)$ into the wave equation

$$\nabla^2 \hat{E}^{(+)} - \frac{1}{c^2} \frac{\partial^2}{\partial t^2} \hat{E}^{(+)} = \frac{4\pi}{c^2} \frac{\partial^2}{\partial t^2} \hat{P}^{(+)} \tag{5.6}$$

where $\hat{P}^{(+)}$ is the sum of the linear and nonlinear (i.e., $3\chi^{(3)} \hat{E}^{(-)} \hat{E}^{(+)} \hat{E}^{(+)}$) contributions of the material polarization. We linearize this equation in the perturbation, and we make the paraxial and slowly varying amplitude approximations. The paraxial approximation can break down under conditions of catastrophic self focusing, but the present calculation deals only with the initiation of the filamentation process which can be treated adequately within the framework of the paraxial approximation. [79,80] We thereby obtain the coupled equations which describe the spatial evolution of the mode amplitudes

$$\frac{d}{dz} \hat{a}(\mathbf{q}, \omega; z) = C(q, \omega) \hat{a}(\mathbf{q}, \omega; z) + D(q, \omega) \left[e^{-i\Delta k z} \hat{a}^\dagger(-\mathbf{q}, 2\omega_0 - \omega; z) \right] \tag{5.7}$$

$$\frac{d}{dz} \left[e^{-i\Delta k z} \hat{a}^\dagger(-\mathbf{q}, 2\omega_0 - \omega; z) \right] = F(q, \omega) \hat{a}(\mathbf{q}, \omega; z) + E(q, \omega) \left[e^{-i\Delta k z} \hat{a}^\dagger(-\mathbf{q}, 2\omega_0 - \omega; z) \right] \tag{5.8}$$

The coefficients that appear in these equations are given by

$$C(q, \omega) = -\frac{i}{2(k_z(\omega) + \gamma_0)} \left(q^2 + (k_z(\omega) + \gamma_0)^2 - k^2(\omega) - 4k_0\gamma_0 \left(\frac{\omega}{\omega_0} \right)^2 \right) \tag{5.9}$$

$$D(q, \omega) = \frac{i\gamma_0 k_0}{k_z(\omega) + \gamma_0} \left(\frac{\omega}{\omega_0} \right)^2 \tag{5.10}$$
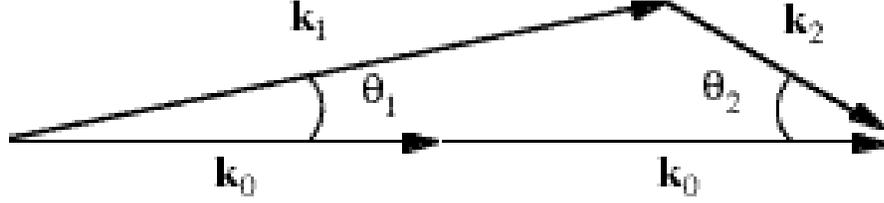
Figure 5.3: Filamentation phase-matching diagram. Wavevector matching diagram describing the four-wave mixing process that leads to filamentation.

$$E(q, \omega) = -i\Delta k(\omega) - C(q, 2\omega_0 - \omega) \tag{5.11}$$

$$F(q, \omega) = -D(q, 2\omega_0 - \omega) \tag{5.12}$$

where

$$\Delta k(\omega) = k_z(\omega) + k_z(2\omega_0 - \omega) - 2k_0. \tag{5.13}$$

We solve Eqs. 5.7 and 5.8 to obtain

$$
\begin{aligned}
\hat{a}(\mathbf{q}, \omega; z) &= \hat{a}(\mathbf{q}, \omega; 0)e^{g_0 z}\left\{\cosh g_1 z + \frac{C - E}{2g_1}\sinh g_1 z\right\} \\
&+ e^{-i\Delta k z}\hat{a}^\dagger(-\mathbf{q}, 2\omega_0 - \omega; 0)e^{g_0 z}\left\{D\frac{\sinh g_1 z}{g_1}\right\} \tag{5.14}
\end{aligned}
$$

where $g_0 = (C + E)/2$ and $g_1 = \sqrt{(C - E)^2 + 4DF}/2$. Note that we have not assumed that the angle between the wavevectors of the pump and the perturbation is necessarily small. We can thus treat interactions, such as that illustrated in Fig. 5.3, which for $|\mathbf{k}_2| \ll |\mathbf{k}_1|$ can be nearly phase matched even for large angles θ_2. We

are required to include interactions of this sort because the quantum fluctuations that initiate the four-wave mixing process are spectrally broad band. Inspection of the form of the coefficients $C(q, \omega)$ and $E(q, \omega)$ shows that the gain eigenvalue $g_0(q, \omega)$ is always imaginary, but that the other eigenvalue $g_1(q, \omega)$ can be either real or imaginary depending on the values of q and ω. When $g_1(q, \omega)$ is real, the mode amplitude undergoes nearly exponential growth.

We next consider the effects of the growth of the mode amplitudes on the overall propagation of the optical beam. We calculate the total intensity of the perturbation as

$$
\begin{aligned}
I_{filament} &= \frac{nc}{2\pi} \langle \hat{\mathcal{E}}_1^\dagger(\mathbf{r}, t) \hat{\mathcal{E}}_1(\mathbf{r}, t) \rangle & (5.15) \\
&= \frac{nc}{2\pi} \int_0^{2\omega} d\omega \int_R dq 2\pi q |N|^2 |D|^2 \frac{\sinh^2 g_1 z}{g_1^2} & (5.16)
\end{aligned}
$$

where we have assumed that at the input to the nonlinear medium the perturbation is in the vacuum state and where R denotes integration only over those transverse wavevectors for which $g_1(q, \omega)$ is real. We have evaluated this integral and find that for $z \ll \gamma_0^{-1}$ the result can be approximated by

$$
I_{filament}(z) = 0.051 \frac{n_0 c}{2\pi} \left[\frac{\hbar \omega_0 k_0^2}{4\pi} \gamma_0 \right] e^{2\gamma_0 z} \tag{5.17}
$$
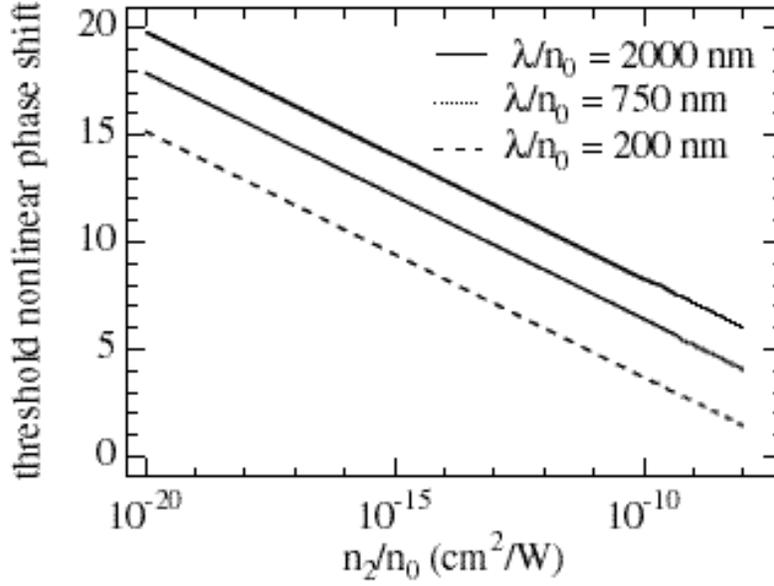
Figure 5.4: Normalized laser intensity at filamentation threshold (i.e. the nonlinear phase shift B_{th}) versus the nonlinearity parameter for various laser wavelengths.

which indicates that vacuum fluctuations supply an effective input intensity of

$$I_0^{vac} = 0.051 \frac{n_0 c}{2\pi} \frac{\hbar\omega_0 k_0^2}{4\pi} \gamma_0 \tag{5.18}$$

Using Equation 5.17, we readily determine the filamentation threshold distance z_f, which we arbitrarily take to be the distance at which the filament intensity reaches one-tenth of the input pump intensity I_0, and which is given by

$$z_f = \frac{1}{2\gamma_0} \ln \frac{8\pi^2}{0.51\hbar\omega_0 k_0^3 n_2 c} \tag{5.19}$$

This result is illustrated in Fig. 5.4, which shows how the dimensionless parameter

$B_{th} = \gamma_0 z_f = n_2 I_0 z_f \omega_0 / c$, which can be interpreted as the nonlinear phase shift experienced by the pump wave at the threshold for filamentation, depends on the nonlinearity parameter n_2/n_0 for a variety of laser wavelengths. Note that typical threshold phase shifts are in the range 5 to 15, comparable to those of stimulated scattering processes.

As a specific example of the application of these results, let us consider the case of a laser beam propagating through air, for which $n_2 = 5 \times 10^{-19} \mathrm{cm}^2/\mathrm{W}$. [81] For the case of an input beam at a wavelength of 775 nm with intensity $10^{11} \mathrm{W/cm}^2$, we find that the effective vacuum input intensity is 0.128 mW/cm^2 and that the filament intensity reaches one-tenth of the input intensity at a distance of 40 m. This distance is comparable to those that have been used in high-intensity laser-beam propagation experiments. [82] We note, for comparison, that a beam with a diameter of 3 cm has a whole beam self-focusing [83,84] distance of about 67 m and a Rayleigh range of about 2 km. Filamentation induced by vacuum fluctuations is thus seen to impose a realistic limitation on the intensities and distances over which a high-power beam can propagate.

5.4 Filamentation as an interferometric source

Of interest in the context of multiphoton entangled state sources is whether the vacuum-initiated filamentation process can serve as a source of correlated photon pairs in the same manner as spontaneous parametric downconversion. For

this reason, we will close this chapter with a brief assessment of the similarities and differences between the two processes. For simplicity we will consider the frequency-degenerate case in the remainder of this chapter.

In the degenerate case, where all fields are at ω_0, the relationship between modes (for those that see gain) is given by

$$\hat{a}(\mathbf{q}, z) = U(q, z)\hat{a}_0(\mathbf{q}) + V(q, z)\hat{a}_0^\dagger(-\mathbf{q}) \tag{5.20}$$

where

$$U(q, z) = \cosh \Lambda z - \frac{\xi}{\Lambda} \sinh \Lambda z \tag{5.21}$$

$$V(q, z) = \frac{i\gamma}{\Lambda} \sinh \Lambda z. \tag{5.22}$$

γ is the nonlinear wavevector component, and ξ and Λ are transverse-wavevector-dependent quantities. By inspection, it can be seen that Λ serves as the gain parameter.

This type of mode relationship is clearly reminiscent of the parametric down-converter mode relationship given in Equations 4.7 and 4.8. Instead of coupling pairs of modes with the frequency relationship $\omega_s + \omega_i = \omega_0$, filamentation couples pairs of modes with the wavevector relationship $\mathbf{q}_1 + \mathbf{q}_2 = 0$. As in the case of parametric downconversion with a broadband pump, for which ω_0 can take on a range of values, the transverse wavevector relationship is relaxed if the pump field

has a range of **q** components (e.g. a focused beam). The coupling of annihilation operators to creation operators in both cases reflects the possibility of spontaneous initiation of the process via vacuum fluctuations.

The processes differ in the specifics of the energy conservation relationships obeyed. Because filamentation is a four-wave mixing process, all four photons can be degenerate in frequency. This relationship is unlike the parametric down-conversion case, in which, if spectral indistinguishability is to be maintained, the signal and idler have approximately twice the wavelength of the pump. In quantum lithographic applications, where maintaining a short wavelength is desirable from the perspective of spatial resolution, a process in which the created photons are degenerate with the pump is desirable.

While the wavelength degeneracy of filamentation can be seen as advantageous in the context of resolution limits, it raises another concern–how to distinguish the seeded process from the spontaneous process. As will be discussed in Chapter 6, seeding with a coherent state alters the nature of the process and, in the context of quantum lithography, can lead to the presence of an undesirable spatial frequency component. It is thus desirable to be able to distinguish the seeded and spontaneous processes. In parametric downconversion, because of the wavelength difference between the pump and the signal, accidental seeding of the process by the pump is not a concern. In beam filamentation, spatial components introduced by wavefront irregularities often serve to seed the four-wave mixing process.

Addressing this issue is necessary for beam filamentation to have utility in this context. If the goals are reversed, however, so that the observation of vacuum-induced filamentation is the aim rather than the generation of a sub-Rayleigh pattern, one might imagine that the presence or absence of the additional spatial frequencies added by coherent-state input might be of use as an indicator of the presence of seeding in the process.

5.5   Conclusion

In this chapter we have considered an alternative spontaneous wave-mixing process as a generator of correlated photon pairs. We showed that vacuum-induced beam filamentation places a limit on the light intensity that can be propagated through a nonlinear material and compared this process to parametric downconversion in the context of fourth-order interferometric configurations.

Chapter 6

Comparison to Other Multiphoton Sources

6.1 Introduction

The states produced by parametric downconversion have interesting and useful quantum properties at both the low and high gain levels. We have presented calculations showing that certain fourth-order interferometric properties identified with two-photon state inputs are retained even when the source gain is increased. In some cases, the desired property is reduced to an asymptotic level; in other cases, the desired property is retained, but only under a restrictive set of source and interferometer conditions.

For example, in the case of quantum lithography, a two-photon entangled state input produces a pattern with a spatial period of $\lambda/4$, no components at $\lambda/2$, and a visibility of 1. When the parametric downconverter interaction strength is increased, the periodicity of the pattern is retained, but the visibility drops to $1/5$.

The rate of visibility loss can be slowed dramatically in some cases through the use of filtering, as the filtering process favors one type of coincidence count pathway over the other pathways. Although the selection of a particular pathway produces beneficial results in the quantum lithography configuration, it also reduces or eliminates the terms arising from interference between pathways. Since this path interference is a hallmark of other interferometers such as the Hong-Ou-Mandel interferometer, it is clear that this filtering process cannot be generalized to other fourth-order configurations. Furthermore, visibility enhancement in the absence of pathway interference suggests that states with the unique characteristics of the those produced by downconversion may not be required to achieve the results of quantum lithography.

A question that follows naturally from results of this type is whether the outputs produced by a high-gain parametric downconversion source can be duplicated by a coherent state source. Although two-photon entangled state sources have been shown to be superior to coherent state sources for the generation of many of these properties of interest, it is less clear that the results produced by high-gain parametric downconversion retain this superiority.

A related question is the extent to which the presence of a seed affects the character of the pattern produced by parametric downconversion at low and high gain levels. We have considered so far only processes initiated by vacuum fluctuations–spontaneous parametric downconversion and vacuum-initiated fila-

mentation. However, in a particular experimental setting, a seeded configuration may be easier to implement. It is thus of interest to consider whether the presence of a seed degrades the interferometric properties of interest.

In this chapter, we return to the single mode model of Chapter 3 to investigate coherent and seeded parametric amplifier source states as multiphoton pair fourth-order interferometric sources. The systems considered are the Hong-Ou-Mandel interferometer and quantum lithography configurations. In each system, the output property of interest differs. The property characteristic of a two-photon entangled state source in the Hong-Ou-Mandel setup is coincidence count cancellation. We thus use the coincidence count rate relative to the product of the individual detector count rates as the basis for comparison of high-gain optical parametric generator performance to that obtained by the use of coherent state inputs. In the quantum lithography configuration, the variation of the output pattern on wavelength and the size of this variation relative to its background are the properties of interest. We thus use the presence of a $\lambda/4$ spatial component, the absence of a $\lambda/2$ component, and the pattern visibility as the bases for comparison.

We first consider the impact of seeding in this model and examine the implication of these results for the use of filamentation as a fourth-order interferometric source. We then consider coherent state inputs, both phase coherent and phase in-

coherent, and compare the results for these two interferometers to those obtained for spontaneous parametric downconversion in Chapter 3.

6.2 Joint detection probability

We begin by recalling from Section 3.4 that a generalized four-port fourth-order interferometer can be described by

$$
\begin{pmatrix} \hat{a}_{o_1} \\ \hat{a}_{o_2} \end{pmatrix} = \begin{pmatrix} A & B \\ C & D \end{pmatrix} \begin{pmatrix} \hat{a}_s \\ \hat{a}_i \end{pmatrix} \tag{6.1}
$$

where $\hat{a}_s$ and $\hat{a}_i$ are the input signal and idler modes, $\hat{a}_{o_1}$ and $\hat{a}_{o_2}$ are output modes, and A, B, C, and D are coefficients specific to the particular interferometer used.

The joint detection probability for this system is given by

$$
\begin{aligned}
\langle \hat{a}_{o_1}^\dagger \hat{a}_{o_2}^\dagger \hat{a}_{o_2} \hat{a}_{o_1} \rangle \;=\;\; & |C|^2 |A|^2 \langle \hat{a}_s^\dagger \hat{a}_s^\dagger \hat{a}_s \hat{a}_s \rangle \\
& + |D|^2 |A|^2 \langle \hat{a}_s^\dagger \hat{a}_i^\dagger \hat{a}_i \hat{a}_s \rangle \\
& + |C|^2 |B|^2 \langle \hat{a}_i^\dagger \hat{a}_s^\dagger \hat{a}_s \hat{a}_i \rangle \\
& + |D|^2 |B|^2 \langle \hat{a}_i^\dagger \hat{a}_i^\dagger \hat{a}_i \hat{a}_i \rangle \\
& + 2 \ \mathrm{Re}\, C^* A^* D A \langle \hat{a}_s^\dagger \hat{a}_s^\dagger \hat{a}_i \hat{a}_s \rangle \\
& + 2 \ \mathrm{Re}\, C^* A^* C B \langle \hat{a}_s^\dagger \hat{a}_s^\dagger \hat{a}_s \hat{a}_i \rangle \\
& + 2 \ \mathrm{Re}\, C^* A^* D B \langle \hat{a}_s^\dagger \hat{a}_s^\dagger \hat{a}_i \hat{a}_i \rangle \\
& + 2 \ \mathrm{Re}\, D^* A^* C B \langle \hat{a}_s^\dagger \hat{a}_i^\dagger \hat{a}_s \hat{a}_i \rangle \\
& + 2 \ \mathrm{Re}\, D^* A^* D B \langle \hat{a}_s^\dagger \hat{a}_i^\dagger \hat{a}_i \hat{a}_i \rangle \\
& + 2 \ \mathrm{Re}\, C^* B^* D B \langle \hat{a}_i^\dagger \hat{a}_s^\dagger \hat{a}_i \hat{a}_i \rangle .
\end{aligned}
\tag{6.2}
$$

We can again note that, proceeding term by term, the effect of the interferometer and the effect of the choice of input state are separately described by coefficient products such as $|C|^2|A|^2$ and by fourth-order expectation values such as $\langle \hat{a}_s^\dagger \hat{a}_i^\dagger \hat{a}_i \hat{a}_s \rangle$. The overall impact of changing input states can thus be analyzed through the comparison of the various signal and idler fourth-order expectation values that appear in this equation. In Chapter 3 this comparison was conducted for low- and high-gain output of an optical parametric generator; here we are contrasting the high-gain OPG output with a seeded parametric amplification process and with various coherent state inputs.

6.3 Seeded parametric processes

In this section, we will calculate the output produced by a seeded parametric process using the same model used in Section 3.4. The interaction between the signal mode $\hat{a}_s$ and idler mode $\hat{a}_i$ is described by

$$\hat{a}_s = U\hat{a}_{s0} + V\hat{a}_{i0}^\dagger \tag{6.3}$$

$$\hat{a}_i = U\hat{a}_{i0} + V\hat{a}_{s0}^\dagger \tag{6.4}$$

where

$$U = \cosh G \tag{6.5}$$

$$V = -i\exp(i\theta)\sinh G, \tag{6.6}$$

G represents the gain of the process and is dependent on the pump amplitude and the size of the material nonlinearity. For parametric downconversion, this gain factor may be written as $G = g|v_0|t$ where t is the interaction time, $|v_0|$ is the pump amplitude, and g is proportional to $\chi^{(2)}$.

The spontaneous process and the seeded process are compared by using input states at the entrance to the source material of $|\text{vac}\rangle_s|\text{vac}\rangle_i$ and $|\alpha_0\rangle_s|\text{vac}\rangle_i$, respectively. The various fourth-order signal and idler expectation values of Equa-

		$\lvert vac\ vac\rangle$	$\lvert \alpha_0\ vac\rangle$
	$\langle a_s^\dagger a_s^\dagger a_s a_s\rangle$	$2\lvert V\rvert^4$	$[\lvert U\rvert^2\lvert\alpha_0\rvert^2+4\lvert V\rvert^2]\lvert U\rvert^2\lvert\alpha_0\rvert^2 + 2\lvert V\rvert^4$
	$\langle a_s^\dagger a_i^\dagger a_i a_s\rangle$	$\lvert U\rvert^2\lvert V\rvert^2 + \lvert V\rvert^4$	$[\lvert U\rvert^2\lvert\alpha_0\rvert^2+3\lvert U\rvert^2+\lvert V\rvert^2]\lvert V\rvert^2\lvert\alpha_0\rvert^2 +\lvert U\rvert^2\lvert V\rvert^2 + \lvert V\rvert^4$
	$\langle a_i^\dagger a_s^\dagger a_s a_i\rangle$	$\lvert U\rvert^2\lvert V\rvert^2 + \lvert V\rvert^4$	$[\lvert U\rvert^2\lvert\alpha_0\rvert^2+3\lvert U\rvert^2+\lvert V\rvert^2]\lvert V\rvert^2\lvert\alpha_0\rvert^2 +\lvert U\rvert^2\lvert V\rvert^2 + \lvert V\rvert^4$
	$\langle a_i^\dagger a_i^\dagger a_i a_i\rangle$	$2\lvert V\rvert^4$	$[\lvert\alpha_0\rvert^2+4]\lvert V\rvert^4\lvert\alpha_0\rvert^2 + 2\lvert V\rvert^4$
	$\langle a_s^\dagger a_s^\dagger a_i a_s\rangle$	0	$[\lvert U\rvert^2\lvert\alpha_0\rvert^2+\lvert U\rvert^2+2\lvert V\rvert^2]U^*V\alpha_0^{*2}$
	$\langle a_s^\dagger a_s^\dagger a_s a_i\rangle$	0	$[\lvert U\rvert^2\lvert\alpha_0\rvert^2+\lvert U\rvert^2+2\lvert V\rvert^2]U^*V\alpha_0^{*2}$
	$\langle a_s^\dagger a_s^\dagger a_i a_i\rangle$	0	$U^{*2}V^2\alpha_0^{*4}$
	$\langle a_s^\dagger a_i^\dagger a_s a_i\rangle$	$\lvert U\rvert^2\lvert V\rvert^2 + \lvert V\rvert^4$	$[\lvert U\rvert^2\lvert\alpha_0\rvert^2+3\lvert U\rvert^2+\lvert V\rvert^2]\lvert V\rvert^2\lvert\alpha_0\rvert^2 +\lvert U\rvert^2\lvert V\rvert^2 + \lvert V\rvert^4$
	$\langle a_s^\dagger a_i^\dagger a_i a_i\rangle$	0	$[\lvert\alpha_0\rvert^2+3]U^*\lvert V\rvert^2 V\alpha_0^{*2}$
	$\langle a_i^\dagger a_s^\dagger a_i a_i\rangle$	0	$[\lvert\alpha_0\rvert^2+3]U^*\lvert V\rvert^2 V\alpha_0^{*2}$

single-input terms = both detected photons arise from a single input arm
dual-input terms = detected photons arise from both input arms

Table 6.1: Coincidence count rate contributions (Eq. 6.2) for states produced by spontaneous and seeded parametric downconversion. The diagrammatic representation for each expectation value is shown at left. Here $\lvert\alpha_0 vac\rangle$ designates an input state seeded by a coherent state input. This state is compared to that produced by spontaneous parametric downconversion, designated by $\lvert vac\ vac\rangle$.

tion 6.2 can then be calculated for each choice of source seed state. The results are shown in Table 6.1.

From Table 6.1, it can be seen that the fourth-order expectation values produced by the spontaneous and seeded processes are qualitatively quite different. Several terms which vanish in the spontaneous case, such as $\langle\hat{a}_s^\dagger\hat{a}_s^\dagger\hat{a}_i\hat{a}_s\rangle$ are nonzero in the seeded case. Furthermore, terms such as $\langle\hat{a}_s^\dagger\hat{a}_s^\dagger\hat{a}_s\hat{a}_s\rangle$ and $\langle\hat{a}_i^\dagger\hat{a}_i^\dagger\hat{a}_i\hat{a}_i\rangle$ that were

equal in the spontaneous case have different values in the seeded case. These differences may be expected to contribute to differences in interferometer output.

Applying these expectation values to the Hong-Ou-Mandel interferometer, it can be shown that the joint detection probability is given by

$$
\begin{aligned}
\langle \hat{a}_{o_1}^\dagger \hat{a}_{o_2}^\dagger \hat{a}_{o_2} \hat{a}_{o_1} \rangle &= \frac{1}{4} \left[(|U|^4 + |V|^4)|\alpha_0|^4 + 4|V|^2(|U|^2 + |V|^2)|\alpha_0|^2 + 4|V|^2 \right] \\
&\quad - \frac{1}{2}|U|^2|V|^2|\alpha_0|^4 \cos 4\phi_0,
\end{aligned}
\tag{6.7}
$$

where a value of zero for the pump phase θ has been assumed. In the limit that $|\alpha_0| = 0$, we regain the spontaneous result of $|V|^4$ (Eq. 3.12).

The joint detection probability for the seeded process in the quantum lithography configuration is given by

$$
\begin{aligned}
\langle \hat{a}_{o_1}^\dagger \hat{a}_{o_2}^\dagger \hat{a}_{o_2} \hat{a}_{o_1} \rangle &= (1 + \sin^2\chi)[\langle \hat{a}_s^\dagger \hat{a}_s^\dagger \hat{a}_s \hat{a}_s \rangle + \langle \hat{a}_i^\dagger \hat{a}_i^\dagger \hat{a}_i \hat{a}_i \rangle] \\
&\quad + (1 - \sin^2\chi)2[\langle \hat{a}_s^\dagger \hat{a}_i^\dagger \hat{a}_i \hat{a}_s \rangle + Re\langle \hat{a}_s^\dagger \hat{a}_s^\dagger \hat{a}_i \hat{a}_i \rangle + Re\langle \hat{a}_s^\dagger \hat{a}_i^\dagger \hat{a}_s \hat{a}_i \rangle] \\
&\quad + 2 \sin\chi[\langle \hat{a}_s^\dagger \hat{a}_s^\dagger \hat{a}_s \hat{a}_s \rangle - \langle \hat{a}_i^\dagger \hat{a}_i^\dagger \hat{a}_i \hat{a}_i \rangle] \\
&\quad + 4 \cos\chi Re[\langle \hat{a}_s^\dagger \hat{a}_s^\dagger \hat{a}_i \hat{a}_s \rangle + \langle \hat{a}_s^\dagger \hat{a}_i^\dagger \hat{a}_i \hat{a}_i \rangle] \\
&\quad + 4 \sin\chi \cos\chi Re[\langle \hat{a}_s^\dagger \hat{a}_s^\dagger \hat{a}_i \hat{a}_s \rangle - \langle \hat{a}_s^\dagger \hat{a}_i^\dagger \hat{a}_i \hat{a}_i \rangle]
\end{aligned}
\tag{6.8}
$$

where the relationships $\langle \hat{a}_s^\dagger \hat{a}_i^\dagger \hat{a}_i \hat{a}_s \rangle = \langle \hat{a}_i^\dagger \hat{a}_s^\dagger \hat{a}_s \hat{a}_i \rangle = \langle \hat{a}_s^\dagger \hat{a}_i^\dagger \hat{a}_i \hat{a}_s \rangle = \langle \hat{a}_s^\dagger \hat{a}_i^\dagger \hat{a}_s \hat{a}_i \rangle$, $\langle \hat{a}_s^\dagger \hat{a}_s^\dagger \hat{a}_i \hat{a}_s \rangle = \langle \hat{a}_s^\dagger \hat{a}_s^\dagger \hat{a}_s \hat{a}_i \rangle$, and $\langle \hat{a}_s^\dagger \hat{a}_i^\dagger \hat{a}_i \hat{a}_i \rangle = \langle \hat{a}_i^\dagger \hat{a}_s^\dagger \hat{a}_i \hat{a}_i \rangle$ have been used. This ex-

pression is very different from the expression for the spontaneous process

$$\langle \hat{a}_{o_1}^\dagger \hat{a}_{o_2}^\dagger \hat{a}_{o_2} \hat{a}_{o_1} \rangle = (1 + \sin^2\chi)[4|V|^4] + (1 - \sin^2\chi)[8|V|^4 + 4|V|^2]. \qquad (6.9)$$

. We can note that terms that are absent in the spontaneous case, such as the term proportional to $\sin\chi$, appear due to the imbalance between amplitudes such as $\langle \hat{a}_s^\dagger \hat{a}_s^\dagger \hat{a}_s \hat{a}_s \rangle$ and $\langle \hat{a}_i^\dagger \hat{a}_i^\dagger \hat{a}_i \hat{a}_i \rangle$. As these new terms are in general undesirable due to their "slower" dependence on χ, the introduction of a seed can clearly have detrimental effects. It is also important to note, however, that the size of these effects is determined by the amplitude of the seed beam. Although the differences between the two cases is qualitatively significant, if a weak seed beam is used, the deviation from the spontaneous case may not be large and will clearly vanish as the seed beam amplitude is decreased to zero.

6.4 Coherent state sources

We can next consider the patterns produced when coherent states are used as inputs directly into the interferometer. Note that in this case, there are no signal and idler beams in the conventional sense, rather "signal" and "idler" are simply used to designate the two interferometer input modes as shown in Figure 3.4.

We will first consider two types of coherent state inputs–phase-coherent and phase-incoherent–and will consider the effect of having matching $(|\alpha_0\rangle_s|\alpha_0\rangle_i)$ or

		$\lvert\alpha_0\,\alpha_0\rangle_{PCoh}$	$\lvert\alpha_0\,\alpha_0\rangle_{PInc}$	$\lvert\alpha_0\,\alpha_1\rangle_{PCoh}$	$\lvert\alpha_0\,\alpha_1\rangle_{PInc}$
(diagram)	$\langle a_s^\dagger a_s^\dagger a_s a_s\rangle$	$\lvert\alpha_0\rvert^4$	$\lvert\alpha_0\rvert^4$	$\lvert\alpha_0\rvert^4$	$\lvert\alpha_0\rvert^4$
(diagram)	$\langle a_s^\dagger a_i^\dagger a_i a_s\rangle$	$\lvert\alpha_0\rvert^4$	$\lvert\alpha_0\rvert^4$	$\lvert\alpha_0\rvert^2\lvert\alpha_1\rvert^2$	$\lvert\alpha_0\rvert^2\lvert\alpha_1\rvert^2$
(diagram)	$\langle a_i^\dagger a_s^\dagger a_s a_i\rangle$	$\lvert\alpha_0\rvert^4$	$\lvert\alpha_0\rvert^4$	$\lvert\alpha_0\rvert^2\lvert\alpha_1\rvert^2$	$\lvert\alpha_0\rvert^2\lvert\alpha_1\rvert^2$
(diagram)	$\langle a_i^\dagger a_i^\dagger a_i a_i\rangle$	$\lvert\alpha_0\rvert^4$	$\lvert\alpha_0\rvert^4$	$\lvert\alpha_1\rvert^4$	$\lvert\alpha_1\rvert^4$
(diagram) $\oplus$ (diagram)	$\langle a_s^\dagger a_s^\dagger a_i a_s\rangle$	$\lvert\alpha_0\rvert^4$	0	$\lvert\alpha_0\rvert^3\lvert\alpha_1\rvert e^{i\phi}$	0
(diagram) $\oplus$ (diagram)	$\langle a_s^\dagger a_s^\dagger a_s a_i\rangle$	$\lvert\alpha_0\rvert^4$	0	$\lvert\alpha_0\rvert^3\lvert\alpha_1\rvert e^{i\phi}$	0
(diagram) $\oplus$ (diagram)	$\langle a_s^\dagger a_s^\dagger a_i a_i\rangle$	$\lvert\alpha_0\rvert^4$	0	$\lvert\alpha_0\rvert^2\lvert\alpha_1\rvert^2 e^{i2\phi}$	0
(diagram) $\oplus$ (diagram)	$\langle a_s^\dagger a_i^\dagger a_s a_i\rangle$	$\lvert\alpha_0\rvert^4$	$\lvert\alpha_0\rvert^4$	$\lvert\alpha_0\rvert^2\lvert\alpha_1\rvert^2$	$\lvert\alpha_0\rvert^2\lvert\alpha_1\rvert^2$
(diagram) $\oplus$ (diagram)	$\langle a_s^\dagger a_i^\dagger a_i a_i\rangle$	$\lvert\alpha_0\rvert^4$	0	$\lvert\alpha_0\rvert\lvert\alpha_1\rvert^3 e^{i\phi}$	0
(diagram) $\oplus$ (diagram)	$\langle a_i^\dagger a_s^\dagger a_i a_i\rangle$	$\lvert\alpha_0\rvert^4$	0	$\lvert\alpha_0\rvert\lvert\alpha_1\rvert^3 e^{i\phi}$	0

(diagram)(diagram) single-input terms = both detected photons arise from a single input arm
(diagram)(diagram) dual-input terms = detected photons arise from both input arms

Table 6.2: Coincidence count rate contributions (Eq. 6.2) for various coherent state inputs. The diagrammatic representation for each expectation value is shown at left. Here $\lvert\alpha_0\alpha_0\rangle$ and $\lvert\alpha_0\alpha_1\rangle$ designate input states with matching and unmatched amplitudes. The subscripts PCoh and PInc represent inputs that are phase coherent and phase incoherent, respectively.

unmatched ($\lvert\alpha_0\rangle_s\lvert\alpha_1\rangle_i$) input amplitudes. As in the previous section, the various states are compared by examining their fourth-order expectation values at the input to the interferometer. Extending Table 3.1 to coherent state sources gives Table 6.2, which displays the expectation value contributions to the joint detection probability (Eq. 6.2) for states of this type. Comparison to Table 3.1 shows that phase-incoherent coherent state inputs have expectation value contributions

similar to those determined for states of the form $|mm\rangle$ and $\sum_m |mm\rangle$. All of the states displayed have absent interference terms (last six terms listed), with the exception of the term $\langle \hat{a}_s^\dagger \hat{a}_i^\dagger \hat{a}_s \hat{a}_i \rangle$ and its complex conjugate. All of these states also have $\langle \hat{a}_s^\dagger \hat{a}_s^\dagger \hat{a}_s \hat{a}_s \rangle$, $\langle \hat{a}_s^\dagger \hat{a}_i^\dagger \hat{a}_i \hat{a}_s \rangle$, $\langle \hat{a}_i^\dagger \hat{a}_s^\dagger \hat{a}_s \hat{a}_i \rangle$, $\langle \hat{a}_i^\dagger \hat{a}_i^\dagger \hat{a}_i \hat{a}_i \rangle$ terms that are present, and of equal or nearly equal magnitude.

Comparison with the coefficient list in Table 3.2 shows that the terms that distinguish the phase-coherent and phase-incoherent states (path interference terms such as $\langle \hat{a}_s^\dagger \hat{a}_s^\dagger \hat{a}_i \hat{a}_s \rangle$) appear to be multiplied by coefficients that vanish in the case of the Hong-Ou-Mandel interferometer, leading one to suspect that these two types of coherent state inputs would produce the same Hong-Ou-Mandel joint detection probability. However, closer inspection of the expression for this probability (Eq. 6.2) shows that the HOMI coefficients shown in Chapter 3 vanish only because the expectation values for the states considered in that chapter are real. Now that the expectation values can be complex (for the case of phase-coherent $|\alpha_0\rangle_s |\alpha_1\rangle_i$ input), the product of the coefficient and expectation value for a given term must be calculated before the real part of the term is taken. Thus purely imaginary HOMI coefficients like that for $\langle \hat{a}_s^\dagger \hat{a}_s^\dagger \hat{a}_i \hat{a}_s \rangle$ will combine with complex expectation values such as $|\alpha_0|^3 |\alpha_1| e^{i\phi}$ to produce nonzero contributions for terms not present with OPG states. These considerations do not affect interferometer coefficients such as those for quantum lithography that are entirely real. The in-

terferometer coefficients (Table 3.2) redone to show the full coefficient value are shown in Table 6.3.

The interferometer-dependent coefficients combined with the state-dependent expectation values can now be used with Equation 6.2 to calculate the joint detection probability for a particular configuration. Doing so for the Hong-Ou-Mandel interferometer, with coefficients given by Eq. 3.18, gives

$$\langle \hat{a}_{o_1}^\dagger \hat{a}_{o_2}^\dagger \hat{a}_{o_2} \hat{a}_{o_1} \rangle = \begin{cases} \frac{1}{4}[|\alpha_0|^4 + |\alpha_1|^4 + 2|\alpha_0|^2|\alpha_1|^2 \cos 2\phi_{si}] & \text{for } |\alpha_0\alpha_1\rangle_{\text{PCoh}} \\ \frac{1}{4}[|\alpha_0|^4 + |\alpha_1|^4] & \text{for } |\alpha_0\alpha_1\rangle_{\text{PInc}} \end{cases} \tag{6.10}$$

for inputs with different magnitudes. For inputs with that are matched in amplitude, these expressions reduce to

$$\langle \hat{a}_{o_1}^\dagger \hat{a}_{o_2}^\dagger \hat{a}_{o_2} \hat{a}_{o_1} \rangle = \begin{cases} \frac{1}{2}|\alpha_0|^4[1 + \cos 2\phi_{si}] & \text{for } |\alpha_0\alpha_0\rangle_{\text{PCoh}} \\ \frac{1}{2}|\alpha_0|^4 & \text{for } |\alpha_0\alpha_0\rangle_{\text{PInc}} \end{cases} \tag{6.11}$$

Note that the phase difference between the two input fields for the phase coherent sources is designated $\phi_{si} = \phi_s - \phi_i$, and is applicable whether the inputs are of equal or unequal magnitudes. (While we have used the notation $|\alpha_0\alpha_0\rangle$ for the matched amplitude case, the calculations were conducted with an input state of the form $|\alpha_0\rangle_s|\alpha_0'\rangle_i$ where $\alpha_0 = |\alpha_0|e^{-i\phi_s}$ and $\alpha_0' = |\alpha_0|e^{-i\phi_i}$.)

For a $|\alpha_0\rangle_s|\alpha_0\rangle_i$ phase coherent input where there is no phase difference between the two input fields ($\phi_{si} = 0$), the joint detection probability $\langle \hat{a}_{o_1}^\dagger \hat{a}_{o_2}^\dagger \hat{a}_{o_2} \hat{a}_{o_1} \rangle$

		OPA	HOMI	QL
	$|C|^2|A|^2$	0	1/4	$(1+\sin \chi)^2$
	$|D|^2|A|^2$	1	1/4	$1-\sin^2 \chi$
	$|C|^2|B|^2$	0	1/4	$1-\sin^2 \chi$
	$|D|^2|B|^2$	0	1/4	$(1-\sin \chi)^2$
	C^*A^*DA	0	i/4	$\cos \chi (1+\sin \chi)$
	C^*A^*CB	0	-i/4	$\cos \chi (1+\sin \chi)$
	C^*A^*DB	0	1/4	$\cos^2 \chi$
	D^*A^*CB	0	-1/4	$\cos^2 \chi$
	D^*A^*DB	0	-i/4	$\cos \chi (1-\sin \chi)$
	C^*B^*DB	0	i/4	$\cos \chi (1-\sin \chi)$

single-input terms = both detected photons arise from a single input arm
dual-input terms = detected photons arise from both input arms

Table 6.3: Coincidence count rate coefficients for various interferometers. For three different situations (listed at the top) the coefficient of the quantum expectation value of each contribution (listed at the left along with its diagrammatic representation) to Eq. 6.2 is given. OPA refers to the joint detection probability at the output of an optical parametric amplifier, HOMI refers to the joint detection probability at the output of a 50/50 beamsplitter, and QL refers to the two-photon absorption rate at the recording plane in a quantum lithography configuration.

has the same value as the product of the two single detector probabilities $\langle \hat{a}_{o_1}^\dagger \hat{a}_{o_1} \rangle$ and $\langle \hat{a}_{o_2}^\dagger \hat{a}_{o_2} \rangle$. As was noted in Chapter 3, this is the same relationship that exists between the joint and single detection probabilities for the high-gain optical parametric generator, for which $\langle \hat{a}_{o_1}^\dagger \hat{a}_{o_2}^\dagger \hat{a}_{o_2} \hat{a}_{o_1} \rangle = \langle \hat{a}_{o_1}^\dagger \hat{a}_{o_1} \rangle \langle \hat{a}_{o_2}^\dagger \hat{a}_{o_2} \rangle = |V|^4$. Thus in both cases there is no reduction in coincidence count rate below the level expected from the single detector rates alone.

For $|\alpha_0\rangle_s |\alpha_0\rangle_i$ phase coherent inputs that are $\pi/2$ out of phase ($\phi_{si} = \pm\pi/2$), the joint detection probability vanishes as it does for a two-photon entangled state. However, examination of the single detector probabilities shows that this occurs for the trivial reason that either $\langle \hat{a}_{o_1}^\dagger \hat{a}_{o_1} \rangle$ or $\langle \hat{a}_{o_2}^\dagger \hat{a}_{o_2} \rangle$ vanishes. This case is very different from the $|1\rangle_s |1\rangle_i$ state, for which the joint detection probability vanishes although the single detector probabilities are nonzero.

The $|\alpha_0\rangle_s |\alpha_0\rangle_i$ phase-incoherent result, which has the value $\frac{1}{2}|\alpha_0|^4$ resembles those obtained with $|m\rangle_s |m\rangle_i$ states, which approach $\frac{1}{2}m^2$ for large m. Comparison between the phase-incoherent state expectation values in Table 6.2 and the $|m\rangle_s |m\rangle_i$ expectation values in Table 3.1 shows that the same terms are present with both state types and that, in the limit of large m, all nonzero terms in both cases have a value equal to the square of the single detector probability.

The results for quantum lithography follow a similar pattern, but have different ramifications due to the different nature of the two interferometric arrangements. With a low-gain parametric downconverter input ($|1\rangle_s |1\rangle_i$), the output pattern

has the desirable quality of unit visibility in a pattern that varies as $\lambda/4$ with no "slow" $\lambda/2$ component. As the gain is increased, the visibility decreases to $1/5$, but the dependence on λ remains the same. We can compare these results to the patterns obtained with coherent state input. For $|\alpha_0\rangle_s|\alpha_1\rangle_{i\text{PCoh}}$, the quantum lithography output pattern is given by

$$
\begin{aligned}
\langle\hat{a}_{o_1}^\dagger\hat{a}_{o_2}^\dagger\hat{a}_{o_2}\hat{a}_{o_1}\rangle & \\
= \; & (1+\sin^2\chi)[|\alpha_0|^4+|\alpha_1|^4]+(1-\sin^2\chi)2|\alpha_0|^2|\alpha_1|^2[2+\cos 2\phi_{si}] \\
+ \; & 2\sin\chi(|\alpha_0|^2-|\alpha_1|^2)+4\cos\chi\cos\phi_{si}|\alpha_0||\alpha_1|[(|\alpha_0|^2+|\alpha_1|^2) \\
+ \; & 4\sin\chi\cos\chi\cos\phi_{si}|\alpha_0||\alpha_1|(|\alpha_0|^2-|\alpha_1|^2)
\end{aligned}
\tag{6.12}
$$

and for $|\alpha_0\rangle_s|\alpha_1\rangle_{i\text{PInc}}$ by

$$
\begin{aligned}
\langle\hat{a}_{o_1}^\dagger\hat{a}_{o_2}^\dagger\hat{a}_{o_2}\hat{a}_{o_1}\rangle = \; & (1+\sin^2\chi)[|\alpha_0|^4+|\alpha_1|^4]+(1-\sin^2\chi)4|\alpha_0|^2|\alpha_1|^2 \\
& +2\sin\chi(|\alpha_0|^2-|\alpha_1|^2)
\end{aligned}
\tag{6.13}
$$

where $\chi=2kx$ is the phase difference between the beams incident on the observation plane at a transverse displacement x. In the limit that $|\alpha_0|=|\alpha_1|$, these expressions reduce to

$$
\begin{aligned}
\langle\hat{a}_{o_1}^\dagger\hat{a}_{o_2}^\dagger\hat{a}_{o_2}\hat{a}_{o_1}\rangle & \\
= \; & (1+\sin^2\chi)2|\alpha_0|^4+(1-\sin^2\chi)2|\alpha_0|^4[2+\cos 2\phi_{si}]
\end{aligned}
$$

$$+ \quad 8\cos\chi\cos\phi_{si}|\alpha_0|^4 \tag{6.14}$$

and

$$\langle \hat{a}_{o_1}^\dagger \hat{a}_{o_2}^\dagger \hat{a}_{o_2} \hat{a}_{o_1} \rangle = 2|\alpha_0|^4(2 + \cos^2\chi) \tag{6.15}$$

for $|\alpha_0\rangle_s|\alpha_0\rangle_{i\text{PCoh}}$ and $|\alpha_0\rangle_s|\alpha_0\rangle_{i\text{PInc}}$, respectively.

From the case of phase-coherent $|\alpha_0\rangle_s|\alpha_0\rangle_i$ input fields with no net phase difference between them ($\phi_{si} = 0$), the joint detection probability reduces to $4|\alpha_0|^4(2 - \sin^2\chi + 2\cos\chi)$. We can note that this output pattern contain the undesired $\cos\chi$ component that varies as $\lambda/2$ and thus does not achieve a sub-Rayleigh-limit pattern. If the $\cos\chi$ term was simply ignored, the pattern resulting from the remaining terms would have a visibility of $1/3$. However, it is not possible to adjust the phase difference between arms to eliminate the $\cos\chi$ term without also affecting the $\sin^2\chi$ term, since the phase difference ϕ_{si} is contained in both. Choosing a value of ϕ_{si} that eliminates the $\cos\chi$ term, such as $\pi/2$, also leads the $\sin^2\chi$ term to vanish. We can note that this is unlike the output pattern produced by the optical parametric generator at either low or high gain. The OPG pattern contains no slowly varying $\cos\chi$ or $\sin\chi$ terms in either case.

The output pattern produced by phase-incoherent equal amplitude fields is proportional to $3 - \sin^2\chi$ and thus does contain the desired 2χ variation without a more slowly varying χ-dependent term. The remaining criterion for assessment

of this source is visibility. It can easily be shown that the visibility for this state

is 1/5, which is the same as that for a high-gain optical parametric generator.

6.5   Conclusion

In this chapter, the output of a high-gain optical parametric generator was com-

pared to a seeded parametric amplifier and various coherent states as sources for

various fourth-order interferometric systems. Section 6.3 showed that the intro-

duction of a seed qualitatively altered the quantum lithography output pattern,

adding undesirable components. The degree of deviation from the vacuum-seeded

pattern was dependent on the seed amplitude; a weak seed might be acceptable

depending on the size of the deviation that can be tolerated.

This result has implications for the utility of vacuum-induced beam filamenta-

tion as a source for fourth-order interferometric applications. While beam filamen-

tation and parametric downconversion can be treated with the same mathemati-

cal model, one significant difference is the presence of seeding for filamentation in

the form of wavefront aberrations. In parametric downconversion, the difference

between the wavelengths of the pump and the output beams allows the sponta-

neous process to be easily distinguished from the seeded process. In the case of

filamentation, the degeneracy in wavelength between the pump and the created

beams, while an advantage for resolution doubling, also implies that fluctuations

present on the pump wavefront can serve as seeds to the interaction; that seeded

process is not easily separated from the spontaneous process. The results of Section 6.3 suggest that a small amount of seeding may still lead to acceptable results; this, in turn, suggests that the issue of wavefront fluctuations need not prevent vacuum-induced filamentation from being considered as a source for this type of interferometric configuration.

Section 6.4 compared the fourth-order interferometric output of the high-gain OPG to that produced by various coherent states. The results are summarized in Table 6.4, which shows both the joint detection probability and the expected coincidence probability defined as the product of the single detector probabilities. This table also includes results calculated for the fourth-order Mach-Zehnder configuration.

From this table we can see that, with an appropriate choice of phase relationship between the two input beams, coherent state output can mimic the output obtained with a two-photon entangled state at the level of the joint detection probability alone. For instance, an output that varies with transverse coordinate and wavelength (as contained in χ) in the same manner as that obtained with a $|11\rangle$ can be achieved in the quantum lithography configuration with the use of two randomly phased equal-amplitude coherent states. However, this apparent similarity disappears when the values of the single detector rates are considered. For both the Hong-Ou-Mandel and the Mach-Zehnder interferometers, the effect of interest is difference between the calculated coincidence count rate and that

	$|1\ 1\rangle$	$|\alpha_0\ \alpha_0\rangle$	OPG
Hong-Ou-Mandel			
$\langle a_1^\dagger a_2^\dagger a_2 a_1\rangle$	0	0 $(\phi_{si} = \pi/2)$	$|V|^4$
$\langle a_1^\dagger a_1\rangle\langle a_2^\dagger a_2\rangle$	1	0	$|V|^4$
Mach-Zehnder			
$\langle a_1^\dagger a_2^\dagger a_2 a_1\rangle$	$\cos^2\chi$	$|\alpha_0|^4\cos^2\chi (\phi_{si}=0)$	$|V|^2[|V|^2+(1+|V|^2)\cos^2\chi]$
$\langle a_1^\dagger a_1\rangle\langle a_2^\dagger a_2\rangle$	1	$|\alpha_0|^4\cos^2\chi$	$|V|^4$
Quantum Lithography			
$\langle a_1^\dagger a_2^\dagger a_2 a_1\rangle$	$4\cos^2\chi$	$2|\alpha_0|^4(2+\cos^2\chi)$ (P|nc)	$4|V|^2[2|V|^2+(1+|V|^2)\cos^2\chi]$
$\langle a_1^\dagger a_1\rangle\langle a_2^\dagger a_2\rangle$	4	$4|\alpha_0|^4$	$4|V|^4$

Table 6.4: Comparison of joint detection probabilities versus expected coincidence levels. The expected coincidence level is here defined as the product of the individual detector probabilities $\langle \hat{a}_{o_1}^\dagger \hat{a}_{o_1}\rangle\langle \hat{a}_{o_2}^\dagger \hat{a}_{o_2}\rangle$ and is compared to the actual joint detection probability $\langle \hat{a}_{o_1}^\dagger \hat{a}_{o_2}^\dagger \hat{a}_{o_2}\hat{a}_{o_1}\rangle$. The sources displayed are the two-photon entangled state ($|11\rangle$), the paired coherent state input ($|\alpha_0\alpha_0\rangle$), and the output of an optical parametric generator (OPG). The phases of the coherent state inputs were chosen to best illustrate similarities in joint detection probabilities and differ for each interferometer ($\phi_{si} = \pi/2$, HOMI; $\phi_{si} = 0$, Mach-Zehnder; random phase, QL).

expected based on the product of the single detector rates. In the case of coherent state input, the calculated rate is simply the product of the single detector rates, indicating no excess or reduction from the rate expected due to accidental coincidences. In contrast, the two-photon entangled state produces a rate that differs from the accidental rate, either in overall reduction as with the HOMI or in dependence on phase difference between arms as in the Mach-Zehnder.

The high-gain optical parametric generator results vary by interferometer. In the Hong-Ou-Mandel interferometer configuration, the calculated rate is the same as the accidental rate. In the Mach-Zehnder, the calculated rate differs from the accidental rate. Quantum lithography is unique among the three cases in that all three sources show a deviation of the calculated coincidence rate from the accidental coincidence rate. It is also unique in that the quantity of interest is truly the joint detection rate alone, rather than the deviation of that rate from other quantities. This implies that both high-gain OPG and coherent state sources are of interest in this configuration. This conclusion is reinforced by the existence of classical proposals for the achievement of sub-Rayleigh-limit lithographic sources [64]. In practice, details of substrate properties as well as the creation of N-photon entangled sources will determine which configuration is of the most experimental relevance.

Chapter 7

Conclusions

In this thesis, our focus has been the assessment of the utility of high-gain sources such as unseeded parametric amplifiers in configurations conventionally associated with two-photon entangled state sources. We have done so by using a single-mode analysis to compare the outputs of three fourth-order interferometers obtained with parametric amplifier and two-photon entangled state sources. These analyses were extended to the multimode case in order to examine the effect of system transfer characteristics on the results. Vacuum-induced beam filamentation was then considered as an alternative to spontaneous parametric downconversion as a source for fourth-order interferometric configurations. The high-gain unseeded parametric amplifier results were then compared with the results obtained using coherent state and seeded amplifier sources.

The first set of analyses involved a model of parametric downconversion in which a single signal mode was coupled to a single idler mode. The output of this source was then used as an input to three different fourth-order interferometric

arrangements. The first interferometer considered was the Hong-Ou-Mandel interferometer. We can recall that a two-photon entangled state used as a source for this interferometer produces no coincidence counts when the arms are matched in pathlength, even though the single detector rates are nonvanishing. We found that the output obtained with a spontaneous parametric downconverter deviated from this result at both low- and high-gain levels, and, in fact, that the coincidence rate for the downconverter output was equal to the product of the single detector rates. There was no coincidence count cancellation even with equal arm pathlengths.

The second single-mode analysis considered the effect of different sources on the output of a fourth-order Mach-Zehnder interferometer. With this interferometer, a two-photon entangled state source produces a fourth-order output proportional to $\cos^2 \chi$, where χ is the phase difference between the two arms. This result is notable given the independence of the single detector rates from χ. When an unseeded parametric amplifier was used, the pattern was found to have the $\cos^2 \chi$ dependence of the entangled state accompanied by an additional gain-dependent background term. In the low-gain limit the visibility was found to increase to the value of unity obtained with a two-photon entangled state source; in the high-gain limit, the visibility was found to decrease to the asymptotic value of $1/3$.

In the third configuration, that of quantum lithography, the most salient properties of the two-photon entangled state pattern are its visibility of one and its

lack of a slowly varying cosine dependence on kx. We show that the unseeded parametric amplifier produces a pattern that has the same desirable relationship to kx, but is accompanied by a gain-dependent background term. As in the Mach-Zehnder case, the visibility returns to the two-photon entangled state level in the low-gain limit, and is reduced to a nonzero asymptotic level in the high-gain limit.

A generalized treatment of four-port fourth-order interferometers was also considered in order to explore the differences among the various results. The contributions to the joint detection probability were decomposed into state-dependent and interferometer-dependent factors. This analysis clarified the role of terms arising from the presence of coincidence counts attributable to photons originating from the same input arm. These single-input-arm terms are not present in the two-photon entangled state case, where all coincidences are attributable to pathways involving both input arms. The contribution of these terms was found to be the origin of the gain-dependent loss of visibility found in the Mach-Zehnder and quantum lithography cases and the loss of coincidence count cancellation in the Hong-Ou-Mandel case. This finding suggests that understanding how to manipulate the balance between various types of contributions to the coincidence count rate will be of importance if multiphoton sources are to be useful in two-photon entangled state configurations.

The single-mode analyses were then extended to the case where multiple signal and idler modes are coupled. A multimode treatment of the parametric ampli-

fier was applied to the Hong-Ou-Mandel interferometer and quantum lithography arrangements. As had been previously found for the two-photon case, the symmetry properties of the spectral distribution function was found to be a factor influencing interferometer output. The impact of the transfer characteristics of an interferometer using these sources on the output pattern was also explored.

In much of this work, the interferometric patterns created with high-gain parametric amplifiers were compared to the outputs generated by two-photon entangled states. While this comparison is central to our goal of understanding which entangled state properties are retained with multiphoton illumination, it neglects another basis for comparison, namely the output produced by coherent state input. We addressed this issue by returning to the single mode model of parametric amplification to investigate coherent and seeded parametric amplifier states as multiphoton pair fourth-order interferometric sources. We found that a coherent state source can mimic the output obtained with a two-photon entangled state at the level of the joint detection probability alone, but that this apparent similarity disappears when the values of the single detector rates are considered. We also showed that the introduction of a seed qualitatively altered the quantum lithography output pattern, adding undesirable components, with the degree of deviation from the vacuum-seeded pattern dependent on the seed amplitude.

One disadvantage of quantum lithography schemes using parametric down-conversion is the lack of resolution doubling when the wavelength of the pump is

considered. There is an increase in resolution by a factor of two from that expected using sources at the signal wavelength. However, this resolution increase is offset by the wavelength doubling produced by a degenerate downconversion process. Sources utilizing four-wave mixing, where the pump and generated fields can be of the same wavelength are thus of interest. We discussed the suitability of vacuum-induced filamentation as a fourth-order interferometric source, comparing its features to those of parametric downconversion.

In these analyses, we have shown that multiphoton sources have promise in contexts conventionally associated with two-photon entangled states. There are, however, trade-offs between increased gain levels and desired output properties such as pattern visibility. This balance is determined by the relative contribution of terms involving both input arms versus terms attributable to a single input arm. The specifics of the source spectrum and the interferometer transfer characteristics affect this balance, making the manipulation of these parameters to mitigate undesirable gain-associated changes a promising area for future study.

Bibliography

[1] Y. Ben-Aryeh, Y. H. Shih, and M. H. Rubin, "Optical wigner functions for two-photon entangled wavepackets," J. Opt. Soc. Am. B **16**, 1730 (1999).

[2] T. E. Kiess, Y. H. Shih, A. V. Sergienko, and C. O. Alley, "Einstein-podolsky-rosen-bohm experiment using pairs of light quanta produced by type-ii parametric downconversion," Phys. Rev. Lett. **71**, 3893 (1993).

[3] Z. Y. Ou, S. F. Pereira, H. J. Kimble, and K. C. Peng, "Realization of the einstein-podolsky-rosen paradox for continuous variables," Phys. Rev. Lett. **68**, 3663 (1992).

[4] T. Kim, O. Pfister, M. J. Holland, J. Noh, and J. L. Hall, "Influence of decorrelation on heisenberg-limited interferometry with quantum correlated photons," Phys. Rev. A **57**, 4004 (1998).

[5] T. Kim *et al.*, "Effect of the detector efficiency on the phase sensitivity in a mach-zehnder interferometer," Phys. Rev. A **60**, 708 (1999).

[6] A. N. Boto, P. Kok, D. S. Abrams, S. L. Braunstein, C. P. Williams, and J. P. Dowling, "Quantum interferometric optical lithography: exploiting entanglement to beat the diffraction limit," Phys. Rev. Lett. **85**, 2733 (2000).

[7] G. Bjork, L. L. Sanchez-Soto, and J. Soderholm, "Entangled-state lithography: tailoring any pattern with a single state," Phys. Rev. Lett. **86**, 4516 (2001).

[8] M. D'Angelo, M. V. Chekhova, and Y. Shih, "Two-photon diffraction and quantum lithography," Phys. Rev. Lett. **87**, 013602 (2001).

[9] A. K. Ekert, J. G. Rarity, P. R. Tapster, and G. M. Palma, "Practical quantum cryptography based on two-photon interferometry," Phys. Rev. Lett. **69**, 1293 (1992).

[10] A. V. Sergienko, M. Atature, Z. Walton, G. Jaeger, B. E. A. Saleh, and

M. C. Teich, "Quantum cryptography using femtosecond-pulsed parametric down-conversion," Phys. Rev. A **60**, R2622 (1999).

[11] D. N. Klyshko, "Scattering of light in a medium with nonlinear polarizability," Sov. Phys. JETP **28**, 522 (1969).

[12] D. C. Burnham and D. L. Weinberg, "Observation of simultaneity in parametric production of optical photon pairs," Phys. Rev. Lett. **25**, 84 (1970).

[13] D. A. Kleinman, "Theory of optical parametric noise," Phys. Rev. **174**, 1027 (1968).

[14] B. R. Mollow, "Photon correlations in a parametric frequency splitting of light," Phys. Rev. A **8**, 2684 (1973).

[15] Z. Y. Ou, J. K. Rhee, and L. J. Wang, "Photon bunching and multiphoton interference in parametric down-conversion," Phys. Rev. A **60**, 593 (1999).

[16] H. H. Arnaut and G. A. Barbosa, "Two-photon pattern in a second-order interference," Phys. Rev. A **58**, 4163 (1998).

[17] G. Bjork and Y. Yamamoto, "Generation of nonclassical photon states using correlated photon pairs and linear feedforward," Phys. Rev. A **37**, 4229 (1988).

[18] A. Luis and J. Peřina, "Su(2) coherent states in parametric down-conversion," Phys. Rev. A **53**, 1886 (1996).

[19] C. K. Hong and L. Mandel, "Theory of parametric frequency downconversion of light," Phys. Rev. A **31**, 2409 (1985).

[20] A. Gatti, E. Brambilla, L. A. Lugiato, and M. I. Kobolov, "Quantum entangled images," Phys. Rev. Lett. **83**, 1763 (1999).

[21] L. A. Lugiato, A. Gatti, H. Ritsch, I. Marzoli, and G. L. Oppo, "Quantum images in nonlinear optics," J. Mod. Opt. **44**, 1899 (1997).

[22] S. P. Choi, M. Vasilyev, and P. Kumar, "Noiseless optical amplification of images," Phys. Rev. Lett. **83**, 1938 (1999).

[23] C. Fabre, J. B. Fouet, and A. Maitre, "Quantum limits in the measurement of very small displacements in optical images," Opt. Lett. **25**, 76 (2000).

[24] J. Jeffers and G. L. Oppo, "Tuning, enhancing, and writing quantum images with input squeezed light," Phys. Rev. A **60**, 2393 (1999).

[25] M. I. Kolobov and C. Fabre, "Quantum limits on optical resolution," Phys. Rev. Lett. **85**, 3789 (2000).

[26] A. Gatti, L. A. Lugiato, G. L. Oppo, R. Martin, P. D. Trapani, and A. Berzanskis, "From quantum to classical images," Opt. Expr. **1**, 21 (1997).

[27] M. Marte *et al.*, "Spatial patterns in optical parametric oscillators with spherical mirrors: classical and quantum effects," Opt. Expr. **3**, 71 (1998).

[28] A. Joobeur, B. E. A. Saleh, T. S. Larchuk, and M. C. Teich, "Coherence properties of entangled light beams generated by parametric downconversion: theory and experiment," Phys. Rev. A **53**, 4360 (1996).

[29] Y. H. Shih, A. V. Sergienko, M. H. Rubin, T. E. Kiess, and C. O. Alley, "Two-photon entanglement in type-ii parametric down-conversion," Phys. Rev. A **50**, 23 (1994).

[30] M. H. Rubin, D. N. Klyshko, Y. H. Shih, and A. V. Sergienko, "Theory of two-photon entanglement in type-ii optical parametric down-conversion," Phys. Rev. A **50**, 5122 (1994).

[31] S. R. Friberg, C. H. Hong, and L. Mandel, "Measurement of time delays in the parametric production of photon pairs," Phys. Rev. Lett. **54**, 2011 (1985).

[32] P. G. Kwiat, K. Mattle, H. Weinfurter, A. Zeilinger, A. V. Sergienko, and Y. Shih, "New high-intensity source of polarization-entangled photon pairs," Phys. Rev. Lett. **75**, 4337 (1995).

[33] J. D. Franson, "Bell inequality for position and time," Phys. Rev. Lett. **62**, 2205 (1990).

[34] P. G. Kwiat, W. A. Vareka, C. K. Hong, H. Nathel, and R. Y. Chiao, "Correlated two-photon interference in a dual-beam michelson interferometer," Phys. Rev. A **41**, 2910 (1990).

[35] R. A. Campos, B. E. A. Saleh, and M. C. Teich, "Fourth-order interference of joint single-photon wavepackets in lossless optical systems," Phys. Rev. A **42**, 4127 (1990).

[36] A. V. Sergienko, Y. H. Shih, and M. H. Rubin, "Experimental evaluation of a

two-photon wavepacket in type-ii parametric downconversion," J. Opt. Soc. Am. B **12**, 859 (1995).

[37] J. G. Rarity and P. R. Tapster, "Fourth-order interference in parametric downconversion," J. Opt. Soc. Am. B **6**, 1221 (1989).

[38] H. Fearn and R. Loudon, "Theory of two-photon interference," J. Opt. Soc. Am. B **6**, 917 (1989).

[39] B. E. A. Saleh, A. Joobeur, and M. C. Teich, "Spatial effects in two- and four-beam interference of partially entangled beams," Phys. Rev. A **57**, 3991 (1998).

[40] E. J. S. Fonseca, P. H. S. Ribeiro, S. Padua, and C. H. Monken, "Quantum interference by nonlocal double slit," Phys. Rev. A **60**, 1530 (1999).

[41] A. Casado, A. Fernandez-Rueda, T. Marshall, R. Risco-Delgado, and E. Santos, "Fourth-order interference in the wigner representation for parametric down-conversion experiments," Phys. Rev. A **55**, 3879 (1997).

[42] A. V. Burlakov *et al.*, "Interference effects in spontaneous two-photon parametric scattering from two macroscopic regions," Phys. Rev. A **56**, 3214 (1997).

[43] E. J. S. Fonseca, J. C. M. da Silva, C. H. Monken, and S. Padua, "Controlling two-particle conditional interference," Phys. Rev. A **61**, 023801 (2000).

[44] Z. Y. Ou and L. Mandel, "Violation of bell's inequality and classical probability in a two-photon correlation experiment," Phys. Rev. Lett. **61**, 50 (1988).

[45] P. G. Kwiat, A. M. Steinberg, and R. Y. Chiao, "High-visibility interference in a bell inequality experiment for energy and time," Phys. Rev. A **47**, R2472 (1993).

[46] Z. Y. Ou, L. J. Wang, and L. Mandel, "Vacuum effects on interference in two-photon downconversion," Phys. Rev. A **40**, 1428 (1989).

[47] Z. Y. Ou, L. J. Wang, X. Y. Zou, and L. Mandel, "Coherence in two-photon down-conversion induced by a laser," Phys. Rev. A **41**, 1597 (1990).

[48] M. H. Rubin, "Transverse correlation in optical spontaneous parametric down-conversion," Phys. Rev. A **54**, 5349 (1996).

[49] D. Branning, *Optical tests of complementarity and nonlocality*, Ph.D. thesis, University of Rochester, 1998.

[50] J. Brendel, E. Mohler, and W. Martienssen, "Time-resolved dual-beam two-photon interferences with high visibility," Phys. Rev. Lett. **66**, 1142 (1991).

[51] C. K. Hong, Z. Y. Ou, and L. Mandel, "Measurement of subpicosecond time intervals between two photons by interference," Phys. Rev. Lett. **59**, 2044 (1987).

[52] W. P. Grice and I. A. Walmsley, "Spectral information and distinguishability in type-ii down-conversion with a broadband pump," Phys. Rev. A **56**, 1627 (1997).

[53] G. D. Giuseppe, L. Haiberger, F. D. Martini, and A. V. Sergienko, "Quantum interference and indistinguishability with femtosecond pulses," Phys. Rev. A **56**, R21 (1997).

[54] M. Atature, A. V. Sergienko, B. M. Jost, B. E. A. Saleh, and M. C. Teich, "Partial distinguishability in femtosecond optical spontaneous parametric downconversion," Phys. Rev. Lett. **83**, 1323 (1999).

[55] Z. Y. Ou, X. Y. Zou, L. J. Wang, and L. Mandel, "Experiment on nonclassical fourth-order interference," Phys. Rev. A **42**, 2957 (1990).

[56] L. Mandel and E. Wolf, *Optical coherence and quantum optics* (Cambridge University Press, Cambridge, 1995).

[57] A. M. Steinberg, P. G. Kwiat, and R. Y. Chiao, "Dispersion cancellation in a measurement of the single-photon propagation velocity in glass," Phys. Rev. Lett. **68**, 2421 (1992).

[58] Z. Y. Ou, C. H. Hong, and L. Mandel, "Relation between input and output states for a beamsplitter," Opt. Commun. **63**, 118 (1987).

[59] W. P. Grice, R. Erdmann, I. A. Walmsley, and D. Branning, "Spectral distinguishability in ultrafast parametric down-conversion," Phys. Rev. A **57**, R2289 (1998).

[60] T. S. Larchuk *et al.*, "Interfering entangled photons of different colors," Phys. Rev. Lett. **70**, 1603 (1993).

[61] J. G. Rarity *et al.*, "Two-photon interference in a mach-zehnder interferometer," Phys. Rev. Lett. **65**, 1348 (1990).

[62] E. J. S. Fonseca, C. H. Monken, and S. Padua, "Measurement of the de broglie wavelength of a multiphoton wave packet," Phys. Rev. Lett. **82**, 2868 (1999).

[63] J. Jacobson, G. Bjork, I. Chuang, and Y. Yamamoto, "Photonic de broglie waves," Phys. Rev. Lett. **74**, 4835 (1995).

[64] E. Yablonovitch and R. B. Vrijen, "Optical projection lithography at half the rayleigh resolution limit by two-photon exposure," Opt. Eng. **38**, 334 (1999).

[65] J. Javanainen and P. L. Gould, "Linear intensity dependence of a two-photon transition rate," Phys. Rev. A **41**, 5088 (1990).

[66] J. P. Jr., B. E. A. Saleh, and M. C. Teich, "Multiphoton absorption cross section and virtual-state spectroscopy for the entangled n-photon state," Phys. Rev. A **57**, 3972 (1998).

[67] G. S. Agarwal, R. W. Boyd, E. M. Nagasako, and S. J. Bentley, "Comment on 'quantum interferometric optical lithography: exploiting entanglement to beat the diffraction limit'," Phys. Rev. Lett. **86**, 1389 (2001).

[68] B. E. A. Saleh, A. F. Abouraddy, A. V. Sergienko, and M. C. Teich, "Duality between partial coherence and partial entanglement," Phys. Rev. A **62**, 043816 (2000).

[69] E. S. Bliss, D. R. Speck, and J. F. H. et al., "Propagation of a high-intensity laser pulse with small-scale intensity modulation," Appl. Phys. Lett. **25**, 448 (1974).

[70] C. Sibilia, Y. Schiavone, and M. B. et al., "Nonclassical spatial properties of light propagation in dissipative nonlinear waveguides," J. Opt. Soc. Am. B **11**, 2175 (1994).

[71] R. Y. Chiao, P. L. Kelley, and E. Garmire, "Stimulated four-photon interaction and its influence on stimulated rayleigh-wing scattering," Phys. Rev. Lett. **17**, 1158 (1966).

[72] E. M. Nagasako, R. W. Boyd, and G. S. Agarwal, "Vacuum-field-induced filamentation in laser-beam propagation," Phys. Rev. A **55**, 1412 (1997).

[73] M. Hercher, "Laser-induced damage in transparent media," J. Opt. Soc. Am. **54**, 563 (1964).

[74] E. Garmire, R. Y. Chiao, and C. H. Townes, "Dynamics and characterization of the self-trapping of intense light beams," Phys. Rev. Lett. **16**, 347 (1966).

[75] R. Y. Chiao, M. A. Johnson, and S. K. et al., "A new class of trapped light filaments," IEEE J. Quant. Elect. 467 (1966).

[76] V. I. Bespalov and V. I. Talanov, "Filamentary structure of light beams in nonlinear liquids," Sov. Phys. JETP **3**, 307 (1966).

[77] R. L. Carman, R. Y. Chiao, and P. L. Kelley, "Observation of degenerate stimulated four-photon interaction and four-wave parametric amplification," Phys. Rev. Lett. **17**, 1281 (1966).

[78] M. Jain, A. J. Merriam, A. Kasapi, G. Yin, and S. E. Harris, "Elimination of optical self-focusing by population trapping," Phys. Rev. Lett. **75**, 4385 (1995).

[79] M. D. Feit and J. J. A. Fleck, "Beam nonparaxiality, filament formation, and beam breakup in the self-focusing of optical beams," J. Opt. Soc. Am. B **5**, 633 (1988).

[80] G. Fibich, "Small beam nonparaxiality arrests self-focusing of optical beams," Phys. Rev. Lett. **76**, 4356 (1996).

[81] D. M. Pennington, M. A. Henesian, and R. A. Hellwarth, "Nonlinear index of air at 1.053 microns," Phys. Rev. A **39**, 3003 (1989).

[82] A. Braun, G. Korn, and X. L. et al., "Self-channeling of high-peak power femtosecond laser pulses in air," Opt. Lett. **20**, 73 (1995).

[83] R. Y. Chiao, I. H. Deutsch, and J. C. Garrison, "Two-photon bound state in self-focusing media," Phys. Rev. Lett. **67**, 1399 (1991).

[84] E. M. Wright, "Quantum fluctuation is nonlinear self-focusing," Chaos Solitons Fractals **4**, 1805 (1994).